DYNAMIC ANALYSIS OF AUTOMOTIVE CARBON FIBER STRUT BAR

MOHD SUFFIAN BIN AB RAZAK

FACULTY OF ENGINEERING
UNIVERSITY OF MALAYA
KUALA LUMPUR

2018

DYNAMIC ANALYSIS OF AUTOMOTIVE CARBON FIBER STRUT BAR

MOHD SUFFIAN BIN AB RAZAK

RESEARCH REPORT SUBMITTED IN PARTIAL FULFILMENT OF THE REQUIREMENT FOR THE DEGREE OF MASTER OF ENGINEERING (MECHANICAL)

FACULTY OF ENGINEERING
UNIVERSITY OF MALAYA
KUALA LUMPUR

2018

UNIVERSITY OF MALAYA

ORIGINAL LITERARY WORK DECLARATION

Name of Candidate: Mohd Suffian bin Ab Razak

Matric No: KQK 160006

Name of Degree: Degree of Master of Mechanical Engineering

Title of Research Report: Dynamic Analysis of Automotive Carbon Fiber Strut Bar

Field of Study: Structural Dynamics and Optimization

I do solemnly and sincerely declare that:

(1) I am the sole author/writer of this Work;
(2) This Work is original;
(3) Any use of any work in which copyright exists was done by way of fair dealing and for permitted purposes and any excerpt or extract from, or reference to or reproduction of any copyright work has been disclosed expressly and sufficiently and the title of the Work and its authorship have been acknowledged in this Work;
(4) I do not have any actual knowledge, nor do I ought reasonably to know that the making of this work constitutes an infringement of any copyright work;
(5) I hereby assign all and every right in the copyright to this Work to the University of Malaya ("UM"), who henceforth shall be owner of the copyright in this Work and that any reproduction or use in any form or by any means whatsoever is prohibited without the written consent of UM having been first had and obtained;
(6) I am fully aware that if in the course of making this Work I have infringed any copyright whether intentionally or otherwise, I may be subject to legal action or any other action as may be determined by UM.

Candidate's Signature　　　　　　　　Date:

Subscribed and solemnly declared before,

Witness's Signature　　　　　　　　Date:

Name:

Designation:

ABSTRACT

Front strut bar is an automotive part commonly used for McPherson suspension system to minimize load on the strut tower by tying both left and right strut with a single bar. By distributing the force acting on a single strut to both strut tower, the strut bar reduces the chassis flex which improves ride and handling especially during cornering. Therefore, strut bar should be stiffer but lighter at the same time to reduce vehicle weight towards fuel efficiency and lower carbon emission. This research attempts to design a lightweight carbon fiber reinforced polymer strut bar in order to replace conventional steel strut bar with equivalent stiffness. For validation, a steel strut bar model is analyzed by conducting experimental modal analysis to determine their natural frequencies and the corresponding mode shapes. These results were compared to analytical and simulation results. Later, the dynamic behavior of CFRP and the corresponding mode shapes were analyzed and correlated with static loading test results. Findings in the dynamic analysis will be used as input in designing a carbon fiber strut bar to further optimizes using composite optimization method in Hyperworks Optistruct until desired characteristics are obtained. The dynamic analysis found out that alternate positive-negative degree ply angle arrangement could resist resonance due to torsion. Combination of different ply orientation and stack sequence results in the design of an optimized carbon fiber strut bar achieved a reduction in weight, higher natural frequency while improving or preserving the static and dynamic performances.

Keywords: composite strut bar, ply orientation, composite optimization, dynamic analysis, experimental modal analysis (EMA), finite element analysis (FEA)

ABSTRAK

Bar topang hadapan adalah satu komponen automotif yang biasa digunakan untuk sistem gantungan McPherson bagi meminimumkan beban pada menara sangga dengan cara mengikat kedua-dua kiri dan kanan sangga dengan sebatang bar. Dengan mengagihkan daya yang bertindak ke atas sangga yang tunggal ke kedua-dua menara sangga, bar topang mengurangkan kelenturan casis yang seterusnya menambah baik perjalanan dan pengendalian terutama semasa di selekoh. Oleh yang demikian, bar topang hendaklah lebih keras tetapi lebih ringan pada masa yang sama untuk mengurangkan berat kenderaan ke arah kecekapan bahan api dan pelepasan karbon yang lebih rendah. Kajian ini cuba untuk mereka bentuk sebuah bar topang polimer diperkukuh gentian karbon yang ringan untuk menggantikan sangga keluli bar konvensional dengan kekerasan yang setara. Untuk pengesahan, model bar topang keluli dianalisis dengan menjalankan eksperimen analisia modal untuk menentukan frekuensi semula jadi dan bentuk mod yang sepadan. Keputusan ini dibandingkan dengan kiraan analitikal dan keputusan simulasi. Kemudian, sifat dinamik CFRP dan bentuk mod telah dianalisis dan menghubung kaitkan dengan hasil ujian statik. Penemuan dalam analisa dinamik akan digunakan sebagai input dalam mereka bentuk sebuah bar topang gentian karbon yang dioptimumkan lagi menggunakan kaedah pengoptimuman komposit di dalam perisian Hyperworks Optistruct sehingga ciri-ciri yang diperlukan dicapai. Analisa dinamik mendapati bahawa susunan sudut positif-negatif lapis berselang seli boleh melawan resonans akibat kilasan. Kombinasi berbeza orientasi lapis dan turutan susunan menghasilkan rekabentuk optima karbon fiber topang bar berjaya mencapai pengurangan berat, frekuensi semula jadi yang lebih tinggi sambil menambah baik atau mengekalkan prestasi statik dan dinamik.

Kata kunci: bar topang komposit, orientasi lapis, pengoptimuman komposit, analisa dinamik, eksperimen analisa modal (EMA), analisa unsur terhingga (FEA)

ACKNOWLEDGEMENTS

Thanks to the Almighty Allah s.w.t. for giving me an opportunity to complete my study on time. Many thanks to my supervisor, Associate Prof. Dr. Rahizar bin Ramli for all guidance and good advice towards issues arises during this project.

Thanks also to Ms. Sim Hoi Yin, in helping me performing experimental modal analysis, Mr. Mohammad Rafi bin Omar for reverse engineering, Mr. Saiful Naim bin Sulaiman for assisting me in composite optimization. Thanks to Universiti Teknikal Malaysia Melaka (UTeM) for sponsoring my Master degree study.

To my beloved wife, thank you for moral support and keeping me motivated in completing this Master degree. Not to forget my mother whom always pray for my success in my study and in my life. This project is dedicated to her for ongoing love and support and to my father who could not see this Master project completed.

Last but not least, to all my friends and family, thanks for all the support and caring. I am lucky to have them around.

TABLE OF CONTENTS

LIST OF FIGURES

LIST OF TABLES

LIST OF SYMBOLS AND ABBREVIATIONS

CFRP	:	Carbon fiber reinforced polymer
FRP	:	Fiber reinforced polymer
EMA	:	Experimental modal analysis
FEA	:	Finite element analysis
EEV	:	Energy efficient vehicles
ESC	:	Electronic stability control
AEB	:	Assisted emergency braking
BiW	:	Body-in-white
FRF	:	Frequency response function
FFT	:	Fast Fourier transform
SISO	:	Single input – single output
SIMO	:	Single input – multiple inputs
MISO	:	Multiple inputs – single output
MIMO	:	Multiple input – multiple output
m	:	Mass
$X(\omega)$	:	Output response
$F(\omega)$	:	Input excitation
c	:	Viscous damping coefficient
k	:	Stiffness
x	:	Absolute displacement of the mass
F	:	Applied force
ω_n	:	Natural frequency
ζ	:	Damping ratio
$\emptyset$	:	Phase angle

APS	:	Auto power spectrum
XPS	:	Cross power spectrum
TLS	:	Total least square
CAD	:	Computer-aided design
FE	:	Finite element
$f(x)$	:	Objective function
$g_j(x)$	:	Constraint function
g_j^U	:	Upper limit of constraint function
X_i	:	Design variables
X_{ik}	:	Thickness of i^{th} super ply of the k^{th} element
N_E	:	No. of elements in a ply in FE model
N_p	:	No. of super ply in FE model
DAQ	:	Data acquisition system
ADC	:	Analog-digital converter
BNC	:	Bayonet Neill Concelman
GUI	:	Graphical user interface
STL	:	Stereolitography
CCD	:	Coupled charge device
CMOS	:	Complementary steel oxide semiconductor
CAM	:	Computer-aided machining
DOF	:	Degree of freedom
FSTOSZ	:	Free size to size optimization
SZTOSH	:	Size to shape optimization
Tx	:	Torsion mode (twisting about system X-axis)
Lt	:	Lateral mode (bending towards system Y-axis)
Tv	:	Transverse mode (bending towards system Z-axis)

LIST OF APPENDICES

CHAPTER 1: INTRODUCTION

The competitive market in the automotive industry has led to higher demands for lower components price and increasing trends in reducing vehicle weight towards better fuel efficiency and lower emission. This, in turn, has resulted in further development of the McPherson type suspension system, which eliminates the upper arm of double wishbone suspension and replaces it with an absorber-spring combination unit. This unit connects the knuckle on the lower end and the flexible mounting on the strut housing of unibody chassis on the upper end for weight reduction as well as minimizing the cost. However, the drawback of this type of suspension is the load acting on the strut tower or strut house, especially when passing over a bump or pothole on the road.

Furthermore, weight reduction on the unibody chassis often led to the reduction in stiffness, which is not a good combination to the McPherson strut in terms of ride and handling. Development of hybrid composite strut tower had been conducted to increase structural rigidity, however, there are challenges in joining the part with the unibody (Lee, Oh, & Kim, 2013).

Front strut bar or strut tower brace is designed to minimize loads on the strut tower by tying both left and right strut with a single bar. By distributing the force acting on a single strut to both strut tower, the strut bar reduces the chassis flex which improves ride and handling especially during cornering. In order to achieve this, the strut bar should be stiffer. Strut bar is generally made of steel or aluminum which is typically heavy or bulky. As such, a lighter component with similar or better performance is desirable. Currently, there are two types of strut bar in the market; single piece type and hinged type. An example is shown in Figure 1.1. Single piece type provides maximum rigidity compared to other types.

Figure 1.1: Single-piece strut bar (left) and hinged type strut bar (right)

The lightweight design of metallic structures in vehicle body had been optimized to reduce material through finite element simulation technology which altered a component's topology, size, and shape. This method, however, has a limit in weight minimization where further weight reduction will compromise the structural rigidity and durability. Therefore, substituting steels with alternative materials such as composite is a promising solution for further weight reduction.

Laminated fiber reinforced polymer (FRP) materials, such as glass, aramid, carbon fiber and boron with epoxy matrix are commonly used composite for automotive application. A popular option among them is carbon–epoxy fiber reinforced polymer (CFRP), due to its higher strength–to–weight ratio and environmental resistance. CFRP can achieve up to 13 times stronger than aluminum in term of tensile strength with about half of its weight. CFRP can be tailored for a specific purpose, which broadens its capabilities. Properties of CFRP can be customized according to the ply angles, ply thickness and stacking sequence.

The forces transmitted from McPherson suspension system to the body directly influence the ride and handling performance of a vehicle. Car manufacturers typically use steel strut bars to stiffen the chassis structure, but a major disadvantage is the weight of steel strut bars. Therefore, this research project aims to develop a carbon fiber strut bar with stiffness value comparable to steel strut bar, with lighter weight.

Experimental modal analysis (EMA), together with finite element modeling are to be conducted in order to develop a modal model of carbon fiber strut bar. To simplify the problem, the modal model is analyzed on a steel plate to determine their natural frequencies and the corresponding mode shapes. These results were compared to analytical and simulation results. Later, the dynamic behavior of CFRP and corresponding mode shape had to be analyzed and correlated with static loading test result. Findings in the dynamic analysis will be used as input in designing a carbon fiber strut bar to further optimizes using composite optimization method in finite element method (FEA) software Hyperworks Optistruct until desired characteristics are obtained.

1.1 Research Objectives

The objectives of this study can be outlined as the followings:

i. Validate the dynamic properties of cantilever beam through experiment, analytical and numerical method.

ii. Analyze the dynamic behavior of steel and carbon fiber strut bar through FEA simulation

iii. Design optimization of lightweight carbon fiber strut bar using composite optimization method in FEA simulation software.

1.2 Scope of Work

i. To determine the dynamic properties of a simple cantilever beam through experimental modal analysis (EMA) using OROS NVGate and ME' Scope software.

ii. To validate the EMA result of simple cantilever beam through analytical and finite element analysis (FEA) simulation.

iii. To model and simulate the steel strut bar in FEA simulation.

iv. To evaluate carbon fiber laminate configuration suitable for strut bar application through simulation.

v. Design and optimization of CFRP laminate strut bar using FEA software. Fabrication of composite strut bar is not covered in this project.

CHAPTER 2: LITERATURE REVIEW

Research on energy efficient vehicles (EEV) are increasingly gaining momentum as the automotive industry strive to increase fuel efficiency and reduce carbon emission. Among others, fuel efficiency can be increased through powertrain optimization, aerodynamic improvement, rolling resistance reduction and mass reduction. Powertrain design and performance has been much improved by replacing mechanical components with electrical sensors and actuators, whilst aerodynamic can be achieved by reducing the frontal area, which usually results in a lowered roof and cabin. Rolling resistance resulting from wheel contact with road surface can be improved through tire profile and road surface improvement. Electrification of system attached to the engine such as air conditioning system, water pump, start-stop system using belt driven alternator will also improve the energy efficiency (Berggren & Magnusson, 2012)

However, these enhancements have not contributed a significant improvement in terms of overall car weight. For most manufacturers, reducing vehicle weight is a viable solution given the increasing car weight over the years due to regulations on safety as well as market demands in terms of engine performance, ride and handling, interior cabin comfort etc. Active safety elements such as traction control, electronic stability control (ESC), minimum of six airbags, autonomous emergency braking (AEB) and anti-lock braking system all contributed to the additional weight in a car.

A study on vehicle mass reduction found that efficiency is improved up to 7% for every 10% weight removed, whilst for every 1 kg removed, approximately 20 kg of carbon dioxide emission could be reduced (Cheah & Heywood, 2010). Weight reduction also has tangible benefit in terms of fuel saving. By reducing the vehicle weight, lower torque and power are required, thus allowing for downsizing of engine displacement, even smaller transmission system and smaller tanks. In turn, this will lead to an improvement of 8-10% of fuel efficiency for every 10% of vehicle weight loss (Miller et al., 2000).

Mass reduction can be achieved through design improvement and substitution of heavy parts with lightweight material. A compilation of vehicle mass breakdown by system and component is shown in Figure 2.1; Body-in-White (BiW), powertrain and suspension each contributes up to 28% of total weight of a vehicle. Among these three major components, there is a bigger opportunity for suspension weight reduction since the vehicle passive safety and carbon emission standards and regulations did not have much influence on the suspension design.

Approximate vehicle mass breakdown[a]

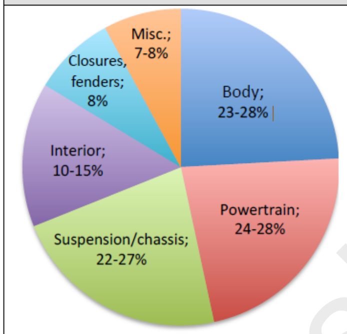

System	Major components in system
Body-in-white	Passenger compartment frame, cross and side beams, roof structure, front-end structure, underbody floor structure, panels
Powertrain	Engine, transmission, exhaust system, fuel tank
Chassis	Chassis, suspension, tires, wheels, steering, brakes
Interior	Seats, instrument panel, insulation, trim, airbags
Closures	Front and rear doors, hood, lift gate
Miscellaneous	Electrical, lighting, thermal, windows, glazing

Figure 2.1: Vehicle weight categorization by system and component (Lutsey, 2010)

The MacPherson strut suspension system has become more popular for passenger car than double wishbone or multi-link due to its simple structure, lower cost, and weight. The MacPherson system is built by having the upper arm removed and the coil spring-absorber directly connected to the strut tower of the unibody. However, this led to some disadvantages in terms of ride and handling, whereas the kinematic characteristics are not as good as double wishbone or multi-link suspension. For example, the change in wheel track length has an adverse effect on body roll center during driving. Camber angle in MacPherson suspension system also did not allow for smooth switching between bounce and jounce (Fallah, Bhat, & Xie, 2008). As more car makers are reducing car in order to increase energy efficiency, more steel parts are reduced, causing stiffness of the unibody chassis to be lowered to the minimum safety requirement. Subsequently, this will affect the quality of ride and handling as the car should absorb more suspension load, especially during excessive cornering and rough road surfaces. When driving over a bump on one tire, the spring compression exerts a force that when high enough, can cause the car chassis to flex and twist. Thus, this will affect the suspension alignment and make the car less stable and unpredictable. Suspension system service life can also be affected and may increase the tire wear rate.

In order to address these problems, the use of safety bars such as front strut bar and rear anti-roll bar is proposed. Front strut bar will increase the stiffness of car chassis slightly by tying up both strut towers with a single bar. In turn, any minimal impact or random excitation on one side of the strut can be canceled by the other strut, thus improving ride and handling. However, as the chassis become stiffer and less flexible, failure would occur at spot weld and sealant joints of the body. Conversely, a very high stiffness will render the strut bar unnecessary (Qviller, 2012). As such, setting a limit on stiffness need to be studied further. On the other hand, rear anti-roll bar also plays a significant role in improving ride and handling by preventing side swaying while cornering, which in turn eliminate body roll and provides stability. This component is not within the scope of this project as the use of carbon fiber is not feasible due to its complex design. The pultrusion process of the composite rear anti-roll bar is currently limited to the straight pipe shape and not suitable for complex design.

According to a research conducted by William F. Milliken (1994), McPherson strut suspension's ride frequency is between 3 to 5 Hz for a race car. It was also mentioned that front axle's frequency is greater than the rear. Given this low frequency, it is an advantage for composite materials to be used in automotive applications. Composite has five times higher damping loss factor than steel, which is around 0.9 to 1.4% (Gur & Wagner, 2017).

A composite is composed of two or more elements combined through chemical and mechanical bonds, which are usually visible. "Matrix phase" is a term used to refer to a combination of the composite materials in the form of woven fibers sheet called the reinforcing phase. These materials are arranged in a specific direction or pattern to improve the strength and characteristic.

Many studies had been done on hybrid composite whereas two or more materials are combined as to take the advantages of each material and reduce the weaknesses, especially on glass-carbon fiber sandwich laminate. By varying the percentage of mass of glass-carbon fibers and their configuration, few researchers concluded that this hybrid composite will have higher flexural modulus than pure glass fiber composite and better impact strength than pure carbon fiber composite (Irina, Azmi, Tan, Lee, & Khalil, 2015; Jagannatha & Harish, 2015; Ni, Lin, & Adams, 1984). Having more carbon fiber will result in better properties in terms of tensile, bending and impact absorption, which can also be improved by changing the stack sequence and orientation for the same weight of carbon and glass fiber (Mohamed, EL-Wazery, EL-Elamy, & Zoalfakar A, 2017; Saravanan. S, 2007). With economic consideration, hybrid carbon glass fiber is a desirable choice to be used in a less critical area or a section that suffer less impact in a full carbon fiber component.

Kalantari (2017) found that matrix void content up to 2% did not affect the ply laminate strength. Degrading effect on performance become critical when 3% or higher void content, $\pm$ 10% laminate thickness variation or $\pm 3°$ variation in ply orientation angle. Structural vibration can be reduced up to 27% with equivalent strength by replacing epoxy matrix with methylmethacrylate (MMA) thermoplastic matrix (Bhudolia, Perrotey, &

Joshi, 2017). In terms of variation of ply orientation, 45°/-45° plies have a lower frequency than 0°/90° plies in flexural mode but have a higher frequency in torsion mode than 0°/90° (Tita, Carvalho, & Lirani, 2003).

Mohammed (2013) conducted an analysis of glass and carbon fiber epoxy composite with various percentage of carbon ply in the glass epoxy ply stack, stacking sequence and ply orientation. He reported that natural frequency will be increased as the percentage of carbon plies increased. As carbon ply is positioned towards the middle of the stacked laminate, the natural frequency will also increase. Ply orientation variation shows that natural frequency for the first three transverse modes of 0°/0° ply orientation is the highest and decreasing as the ply angle increase from 0° to the lowest natural frequency at 45°/-45° ply orientation.

One unique attribute of almost all fiber reinforced composites is their excellent damping capability. This results in improved energy and vibration absorption which significantly reduce noise transmitted to neighboring components. Most composite materials exhibit good or better performance of strength and modulus combination compared to common metallic material available in the market. Because of their lower specific gravity, strength and modulus to weight ratio made the composite materials superior to the metallic material. (Deepak, 2012)

Carbon fiber reinforced polymer has been widely used in automotive industry, especially for vehicle body application. Wang et al., (2018) analyzed the strength, stiffness and peeling strength of CFRP laminates with aluminum honeycomb cores. He reported that stiffness can be improved by increasing the thickness of CFRP. Current technology is capable of manufacturing carbon fiber and glass fiber reinforced polymer through additive manufacturing (Goh et al., 2018). CFRP also can be "welded" to metallic structures or CFRP joints using a polyurethane based adhesive which offers superior strength against stress with greater elasticity than epoxy (Galvez et al., 2017). Apart from that, there is comprehensive research on CFRP for supercapacitor that provides structural strength and energy storage function for electric vehicles (Deka, Hazarika, Kim, Park, & Park, 2017).

Presently, no extensive study had been done on the dynamic behavior of strut bar. Takamatsu et al, (1992) reported 30 kg reduction of components including strut bar to improve 15% torsional stiffness and 20% bending stiffness of Mazda RX-7 sports car body. Kangde, Shitole, & Sahu, (2014) found a good correlation of suspension strain with FE strains at all suspension locations except at strut bar due to higher dynamic stresses.

In order to produce a composite strut bar with strength comparable to those of steel, physical test (hammer test) will be conducted on steel bar to gain the frequency response function (FRF). FRF is a measurement of displacement, acceleration response per unit of excitation force. FRF can be analyzed to gather mechanical properties such as compliance, dynamic stiffness and dynamic mass (Schwarz & Richardson, 1999). Based on these properties, a combination of carbon fiber and fiberglass with a variation of ply angles, thickness, and stacking sequence, composite strut bar can be simulated to achieve the benchmarked properties.

In a nutshell, the dynamic analysis would provide a better understanding of the behavior of strut bar towards deformations and vibrations. Using CFRP for strut bar to replace steel could be an effective measure in reducing weight, stresses, and vibrations. Variation in the thickness and ply orientation should be investigated further and correlated with the static analysis result. On top of that, advancement of FEA in composite optimization will be utilized in designing a lightweight and high-performance carbon fiber strut bar.

CHAPTER 3: THEORETICAL DEVELOPMENT

In order to perform dynamic analysis, there are few guidelines an engineer need to follow. First, the natural frequencies of the structure should be determined. Next, the excitation function should be characterized. Based on the maximum estimated excitation, response to the structure can be calculated. From the calculated response, we can determine whether the response would violate any failure criterion.

Natural frequency can be determined through analytical methods or numerical method at the early design stage. The frequencies may also be measured after the structure or a prototype is built using a method such as experimental modal analysis (EMA) that will be elaborated in this chapter. Each natural frequency has a corresponding damping ratio. These damping ratios are empirical values that should be measured during the experiment.

3.1 Experimental Modal Analysis

Experimental modal analysis (EMA) or modal testing is a method used to characterize resonant vibration which usually occurred in operating machinery and structures. When the operating frequency of a structure's vibration is very close to or coincide with its natural frequency, interaction between inertial and elastic properties of the material within the structure caused the vibration response to be amplified beyond the stress, strain, and deformation that is usually caused by the static loading (Schwarz & Richardson, 1999). The effect is potentially catastrophic; accidents as a result of component failure or even collapse of a building or structure.

The most crucial element in understanding vibration is the modes. Modes, or resonances, are inherent properties of a structure. Resonance change depends on the material properties i.e. mass, stiffness, and damping properties, and boundary conditions of the structure. Relationship of natural frequency, ω, and other material properties can be described by the equation below.

$$\omega = \sqrt{\frac{k}{m}} \tag{3.1}$$

$$\zeta = \frac{c}{C_{cr}} = \frac{c}{2m\omega} \tag{3.2}$$

Each mode excites with different natural frequency, modal damping, and its mode shape. For example, if the thickness of a plate is increased, the mass of the structure is increased, and its natural frequency will decreases.

EMA requires an impact hammer to knock on the specimen or structure to produce excitation (input force). The vibration (output response) of the structure due to the excitation is measured using an accelerometer connected to a high-speed data logger. Based on input force and output response, Fast Fourier Transform (FFT) through software will analyze the data in frequency response function (FRF) graph, which represents the structural response towards the impact hammer excitation. A key feature of FFT analyzer software called curve fitting estimates modal parameters of the system, such as natural frequencies, modal damping, and mode shape. These are valuable information to further understand the resonance of a structure and allows for proactive measures to be taken to avoid it from happening.

There are four methods for conducting EMA (Maia & Silva, 2001). These methods can be chosen depending on the number of data acquisition channels and type of excitation available. The methods are summarized in the following table.

Table 3.1: Four methods in EMA

Method	Number of data acquisition channel	Description
SISO (single input – single output)	2	Longest testing time Fixed input and roving output or vice versa Time invariance problem between measurement
SIMO (single input – multiple outputs)	≥ 3	Shorter testing time than SISO Frequency and damping ratio data acquired simultaneously Inconsistent time interval between measurement
MISO (multiple inputs – single output)	≥ 3	Long testing time Detects repeated root. Maxwell reciprocity check is possible Inconsistent time interval between measurement
MIMO (multiple inputs – multiple outputs)	≥ 4, up to 512	Increase setup time, short testing time Frequency and damping ratio for data acquired simultaneously Detects repeated root. Maxwell reciprocity checks are possible

In this research, SISO method is used. A single input channel for impact hammer, and one channel accelerometer during transverse steel and composite plate EMA had been used. A fixed reference point was knocked to the downward direction, while the accelerometer is roving along the measurement points to measure the response acceleration. EMA of the cantilever beam of steel plate can be performed to compare with FEA simulation (Chaphalkar, Khetre, & Meshram, 2015), as well as the theoretical value using Rayleigh Method to estimate the fundamental bending frequency of this cantilever beam (Church, 1964).

3.1.1 Frequency Response Function

Frequency response function (FRF) is an expression of structural response towards applied excitation as a function of frequency. Experimental measurement of input excitation and output response must be accurate, as they will affect the accuracy of estimated FRF. There are several external factors that can influence the result accuracy, such as noises from measuring devices, leakage, and aliasing in digital signal processing and error in sensor calibration.

To determine the FRF, the system is assumed to linear and time-invariant because the solution of Fast-Fourier Transform (FFT) algorithm is based on limited time history. Therefore, we assume that the waveform created within the recorded time repeats itself over time. The FRF is transformed from time domain to frequency domain through FFT. FRF is the frequency transfer function of a system that described with real and imaginary components of complex function. FRF may also be represented in terms of magnitude and phase.

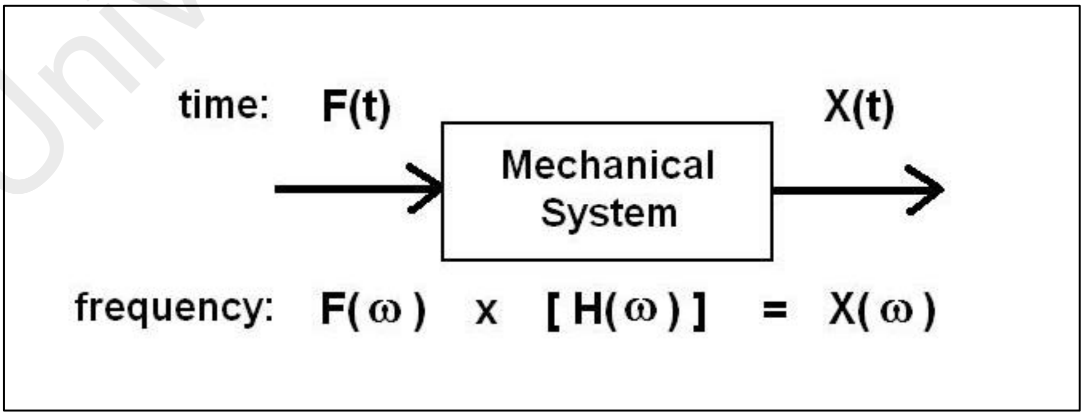

Figure 3.1: Block diagram of an FRF (Schwarz & Richardson, 1999)

FRF is calculated as the ratio of the FFT of an output response $X(\omega)$ to the FFT of the input excitation $F(\omega)$ that causes the output (Figure 3.1). The ratio between output response and input excitation is a complex function of real and imaginary components, or magnitude and phase components. Let $X(\omega) = a + bi$ and $F(\omega) = c + di$, therefore FRF can be defined as

$$H(\omega) = \frac{X(\omega)}{F(\omega)} = \frac{a + bi}{c + di} \quad (3.3)$$

$$\therefore |H(\omega)| = \frac{\sqrt{a^2 + b^2}}{\sqrt{c^2 + d^2}} = \frac{|X(\omega)|}{|F(\omega)|} \quad (3.1)$$

and $$\angle H(\omega) = tan^{-1}\left(\frac{b}{a}\right) - tan^{-1}\left(\frac{d}{c}\right) = \angle X(\omega) - \angle F(\omega) \quad (3.5)$$

Equation (3.3) and (3.4) show that the magnitude of FRF is the ratio of response magnitude to input magnitude, and the phase of FRF signifies the phase difference of response relative to the input. Thus, peaks in FRF magnitude plot represents a great response per unit input excitation which indicates resonance, and frequencies that correspond to these peaks are known as the natural frequency of the system. Here, we understand that FRF is a transfer function that is expressed in a frequency domain.

There are six types of FRF depending on the response being measured as displacement, velocity or acceleration. Table 3.2 summarizes several common names for each of the six types of FRF (Schwarz & Richardson, 1999)

Table 3.2: Six types of FRF definitions

FRF Name	FRF Dimension
Compliance	$\frac{Displacement}{Force}$
Mobility	$\frac{Velocity}{Force}$
Inertance or Receptance	$\frac{Acceleration}{Force}$
Dynamic Stiffness	$\frac{1}{Compliance} = \frac{Force}{Displacement}$
Mechanical Impedance	$\frac{1}{Mobility} = \frac{Force}{Velocity}$
Dynamic Mass	$\frac{1}{Inertance} = \frac{Force}{Acceleration}$

To demonstrate analytically that the relation of FRF with the transfer function of a system, (Irvine, 2000) explained the system through a simple single-degree-of-freedom subjected to external force as shown in Figure 3.2

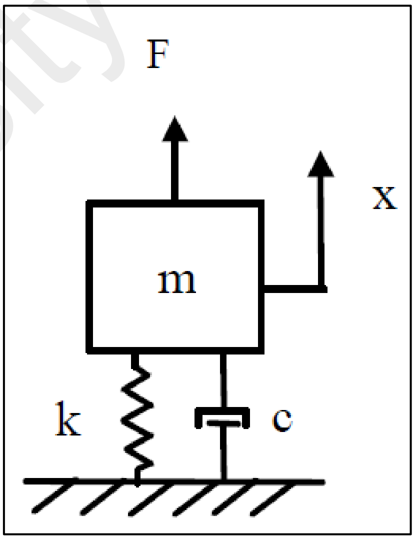

Figure 3.2: Simple single DOF system

The variables are

m: mass,

c: viscous damping coefficient

k: stiffness

x: absolute displacement of the mass

F: applied force

Analysis of free-body diagram is shown in Figure 3.3 below

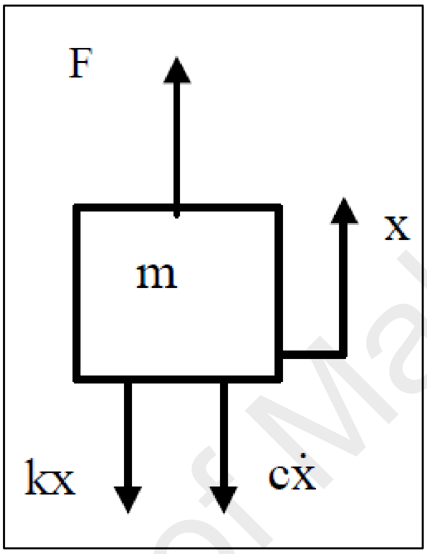

Figure 3.3: Free-body Diagram

Total forces acting on the system are

$$\sum F = m\ddot{x} \tag{3.6}$$

$$m\ddot{x} = -c\dot{x} - kx + F(t) \tag{3.7}$$

$$m\ddot{x} + c\dot{x} + kx = F(t) \tag{3.8}$$

$$\ddot{x} + \frac{c}{m}\dot{x} + \frac{k}{m}x = \frac{F(t)}{m} \tag{3.9}$$

Where $F(t) = \sin \omega t$ is the applied force with frequency ω (rad/s). By convention,

$$\frac{c}{m} = 2\zeta\omega_n \tag{3.10}$$

$$\frac{k}{m} = {\omega_n}^2 \tag{3.11}$$

where ω_n is the natural frequency in (rad/s), and ζ is the damping ratio. Substituting the convention terms into equation (3.9),

$$\ddot{x} + 2\zeta\omega_n\dot{x} + {\omega_n}^2 x = {\omega_n}^2\frac{F}{k} \tag{3.12}$$

The Fourier transform of each side of equation (3.12) above may be taken to derive the steady-state transfer function for the absolute response displacement. After many steps, the resulting transfer function is

$$\frac{X(\omega)}{F(\omega)} = \left[\frac{1}{k}\right]\left[\frac{{\omega_n}^2}{{\omega_n}^2 + \omega^2 + j(2\zeta\omega\omega_n)}\right] \tag{3.13}$$

This transfer function, which represents displacement over force, is sometimes called the receptance function, as shown in Table 3.2. The transfer function can be represented in terms of magnitude and phase angle Ø as

$$\left|\frac{X(\omega)}{F(\omega)}\right| = \left[\frac{1}{k}\right]\left[\frac{{\omega_n}^2}{\sqrt{({\omega_n}^2 - \omega^2)^2 + (2\zeta\omega\omega_n)^2}}\right] \tag{3.14}$$

$$\left|\frac{X(\omega)}{F(\omega)}\right| = \left[\frac{1}{m}\right]\left[\frac{1}{\sqrt{({\omega_n}^2 - \omega^2)^2 + (2\zeta\omega\omega_n)^2}}\right] \tag{3.15}$$

$$\emptyset = \tan^{-1}\left[\frac{2\zeta\omega\omega_n}{{\omega_n}^2 - \omega^2}\right] \tag{3.16}$$

The mobility function is

$$\left|\frac{V(\omega)}{F(\omega)}\right| = \left[\frac{1}{k}\right]\left[\frac{j\omega{\omega_n}^2}{{\omega_n}^2 - \omega^2 + j(2\zeta\omega\omega_n)}\right] \tag{3.17}$$

$$\left|\frac{V(\omega)}{F(\omega)}\right| = \left[\frac{1}{k}\right]\left[\frac{\omega{\omega_n}^2}{\sqrt{({\omega_n}^2 - \omega^2)^2 + (2\zeta\omega\omega_n)^2}}\right] \tag{3.18}$$

$$\left|\frac{V(\omega)}{F(\omega)}\right| = \left[\frac{1}{m}\right]\left[\frac{\omega}{\sqrt{({\omega_n}^2 - \omega^2)^2 + (2\zeta\omega\omega_n)^2}}\right] \tag{3.19}$$

$$\theta = \tan^{-1}\left[\frac{-{\omega_n}^2 + \omega^2}{2\zeta\omega_n}\right] \tag{3.20}$$

The accelerance function is

$$\left|\frac{A(\omega)}{F(\omega)}\right| = \left[\frac{1}{k}\right]\left[\frac{-\omega^2{\omega_n}^2}{{\omega_n}^2 - \omega^2 + j(2\zeta\omega\omega_n)}\right] \tag{3.21}$$

$$\left|\frac{A(\omega)}{F(\omega)}\right| = \left[\frac{1}{k}\right]\left[\frac{-\omega^2{\omega_n}^2}{\sqrt{({\omega_n}^2 - \omega^2)^2 + (2\zeta\omega\omega_n)^2}}\right] \tag{3.22}$$

$$\left|\frac{A(\omega)}{F(\omega)}\right| = \left[\frac{1}{m}\right]\left[\frac{-\omega^2}{\sqrt{({\omega_n}^2 - \omega^2)^2 + (2\zeta\omega\omega_n)^2}}\right] \tag{3.23}$$

$$\alpha = -\pi + \tan^{-1}\left[\frac{2\zeta\omega_n}{{\omega_n}^2 - \omega^2}\right] \tag{3.24}$$

3.1.2 Noise Minimization

From the previous subsection, we know that the components which constructed FRF are mass, stiffness, natural frequency, and damping ratio. The FRF estimation is accurate only if it is free from noise. FFT analyzer built around a tri-spectrum averaging loop across all channel to sample two or more-time domain simultaneously to remove noise and unexpected non-linearity or distortion from FRF estimation. This consists of two Auto Power Spectrum (APS) for each input and output channels and a Cross Power Spectrum (XPS) between two channels. The mechanism of Tri-Spectrum Averaging Loop is shown in Figure 3.4.

.

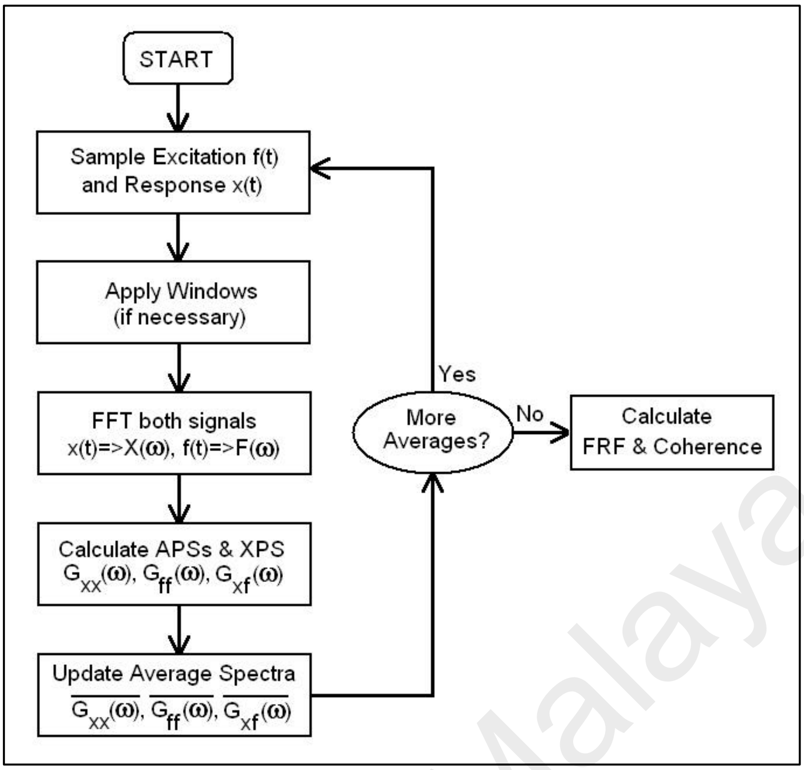

Figure 3.4: Tri-Spectrum Averaging Loop

Based on this method, noise minimization can be performed in three different algorithms, referred as H_1, H_2, and H_V. H_1 is a least squared (LS) FRF estimator which assume noises occur on the output, whereas H_2 assumed noises occur on the input. On the other hand, H_V employs total least square (TLS) technique, and assume that random noise and distortion are a combination of both input and output of the system.

3.1.3 Coherence

The coherence function is used in data quality assessment tool which identifies how much of the output signal is related to the measured signal. Coherence value range from 0 to 1, which indicates the degree of causality in the FRF (Avitabile, 2001). When the coherence is equal to one, the measured response power is caused totally by the measured input power. A coherence value less than one indicates that the measured response power is greater than the input. This happens due to random noise during measurement or inconsistency on the impacting point. The coherence function can be described by equation (3.25):

$$Y^2 = \frac{\text{XPS}^2}{APS_{input} \times APS_{output}} \tag{3.25}$$

However, it is difficult to maintain coherence value of 1 for all measurement. Having a set target of coherence above 0.8, and increasing number of averaging measurement can reduce the noise and non-linearity contributions. Low coherence can also be caused by double impact during hammering, thus affecting the FRF measurement accuracy. More practice on hammering is necessary to impact the structure moderately. When the impact is too hard, the response will be out of its linearity range. If the impact is inadequate, the input power spectrum does not excite all the frequency range and the coherence value and FRF will also deteriorate at the second half of frequency range as shown in Figure 3.5. Softer hammer tip also contributes to deterioration at the second half of frequency range (Avitabile, 2001). Thus, softer hammer tip is suitable for lower frequency range (Figure 3.6). Furthermore, inconsistency in excitation angle and impact point will lead to phase shift in FRF measurement.

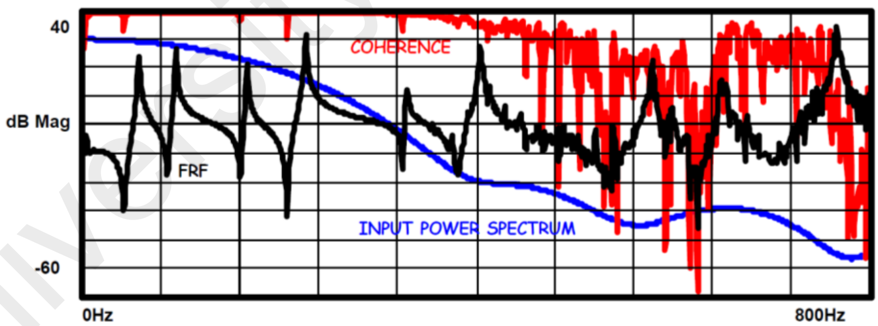

Figure 3.5: Inadequate APS (Avitabile, 2001)

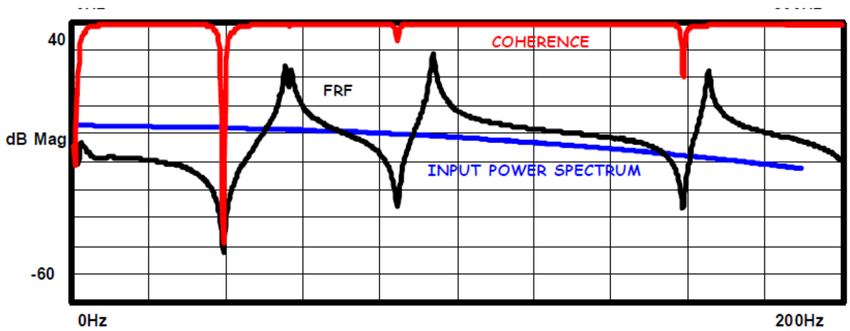

Figure 3.6: Soft hammer tip for low-frequency range (Avitabile, 2001)

3.2 Composite Design and Optimization

3.2.1 Composite Design

The typical composite design uses surfaces in computer-aided design (CAD) which is later converted to shell element in finite element analysis. There are two types of composite design modeling; zone-based and ply-based modeling. Zone-based modeling is a traditional method of composite modeling, wherein zone refers to a region where all the plies similar. There is one property card to represent each unique composite zone. As such it is easier for FEA solver to perform analysis of each zone individually. However, when the finite element (FE) model requires modifications and optimizations this method proves to be rather difficult. On top of that, zone-based modeling does not represent the real-world type of laminate.

In ply based modeling, every individual ply has its own property or control card. Therefore, a specific setting for each ply such as its shape, thickness, ply angle and stacking order can be fully tailored to meet design requirements during optimization. These plies are stacked into one laminate card which represents the composite body as a whole. Figure 3.7 is a typical design cycle for composite currently used in the automotive industry.

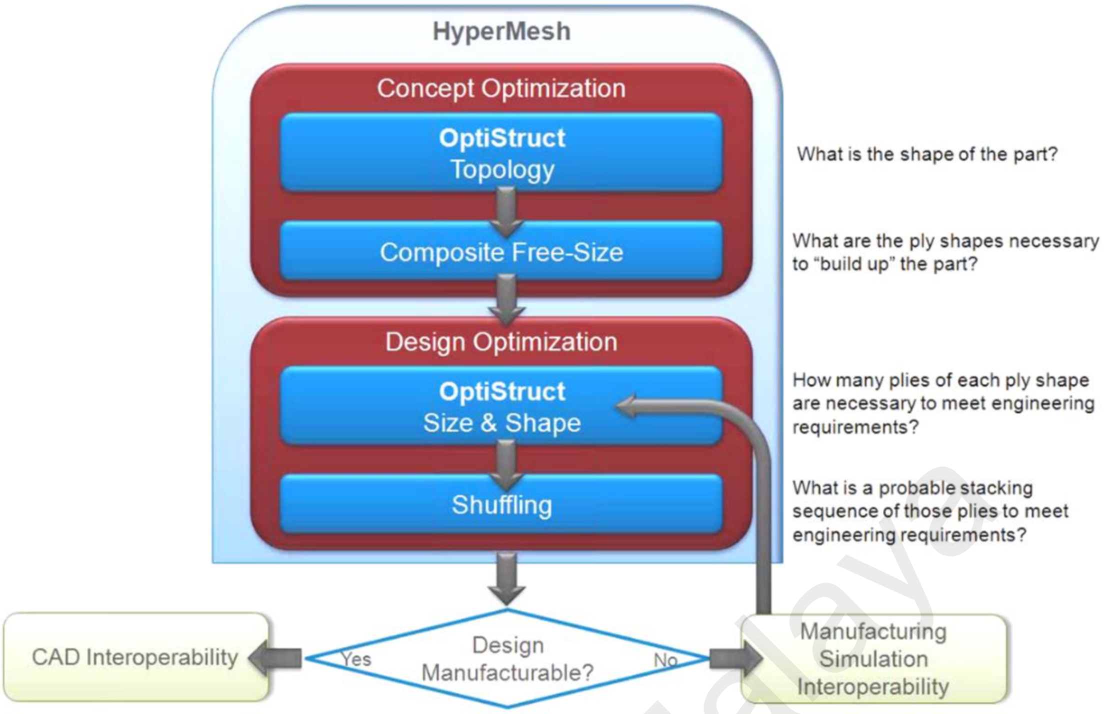

Figure 3.7: Composite design and optimization (www.altair.com)

3.2.2 Unidirectional composite finite element modeling

Main characteristics of unidirectional (UD) composite is that the stiffness and strength are different at different ply angles or directions. The behavior of UD composite is transversely isotropic in a cross-section perpendicular to the fibers. This means the properties in the longitudinal direction (e.g. modulus of elasticity, E_1) is very different from the other direction ‘2' and ‘3' which both are normal to fiber's longitudinal axis (lateral direction) (Figure 3.8). However, direction ‘2' and ‘3' will have same elastic properties (e.g. modulus of elasticity, E_2). This type of material is called ‘orthotropic’ (Matthews, 2003). Direction ‘1’, ‘2’, ‘3’ are also called ‘X’, ‘Y’, ‘Z’ in some literature.

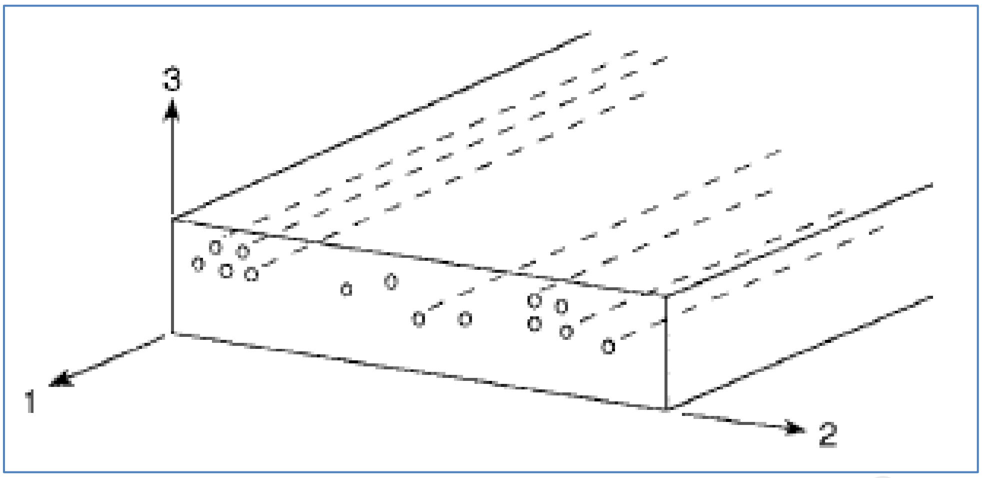

Figure 3.8: Orientation of principal material axes. (Matthews, 2003)

These UD composites will be stacked together, forming a thin sheet construction known as laminate. The stacking sequence and direction of each ply should be predetermined before forming a laminate because these will influence the structural performance of a laminate.

The strength of laminate can be determined by failure criteria that can be separated into three classes; limit criteria, interactive criteria, and hybrid criteria. Limit criteria are the simplest method, and there are two types of limit methods; maximum stress criteria and maximum strain criteria. Maximum stress criteria are given by following equations.

$$\sigma_1 \geq \hat{\sigma}_{1T} \; or \; \sigma_1 \leq \hat{\sigma}_{1C}, or$$

$$\sigma_2 \geq \hat{\sigma}_{2T} \; or \; \sigma_2 \leq \hat{\sigma}_{2C}, or \tag{3.26}$$

$$\tau_{12} \geq \hat{\tau}_{12}$$

$\hat{\sigma}_1$ and $\hat{\sigma}_2$ are pure tensile or compressive strength in longitudinal ('1') and the lateral direction ('2'). $\hat{\tau}$ is the pure shear strength. Laminate is considered failed when either one of sub-criteria in the limit criteria exceeded. Similarly, laminate will be considered when one of these maximum strain criteria exceeded.

$$\varepsilon_1 \geq \hat{\varepsilon}_{1T} \; or \; \varepsilon_1 \leq \hat{\varepsilon}_{1C}, or$$
$$\varepsilon_2 \geq \hat{\varepsilon}_{2T} \; or \; \varepsilon_2 \leq \hat{\varepsilon}_{2C}, or \tag{3.27}$$
$$\gamma_{12} \geq \hat{\gamma}_{12}$$

ε is the normal strain in longitudinal and transverse direction while γ_{12} is the shear strain. Although both maximum stress and maximum strain limit criteria are easy to use, these criteria do not correlate well with experimental data unless the fiber angle is close to 0° or 90°.

This problem can be overcome by interactive criteria, which attempt to allow for interaction of multiaxial stress. The Tsai – Hill interactive criterion has proven successful in many circumstances. This criterion developed for Hill's anisotropic failure which can be traced back to the Von Mises yield criterion for steels. It defines failure as

$$\left(\frac{\sigma_1}{\hat{\sigma}_1}\right)^2 + \left(\frac{\sigma_2}{\hat{\sigma}_2}\right)^2 + \left(\frac{\tau_{12}}{\hat{\tau}_{12}}\right)^2 \geq 1 \tag{3.28}$$

Thus, only one criterion needs to be satisfied compared to five sub-criteria of the limit method. However, this method only gives only a global indication of failure. This is really helpful in designing a lightweight composite structure, where material reduction takes place without compromising its safety and performance.

Hoffman made some improvements by incorporating linear terms into the fracture condition. Under plane stress state, the Hoffman criterion for combined loading of longitudinal stress and shear stress on longitudinal direction can be stated as

$$\frac{\sigma_1^2}{\hat{\sigma}_{1T}\hat{\sigma}_{1C}} + \frac{(\hat{\sigma}_{1c} - \hat{\sigma}_{1T}) \cdot \sigma_1}{(\hat{\sigma}_{1T}\hat{\sigma}_{1C})} + \left(\frac{\tau_{12}}{\hat{\tau}_{12}}\right)^2 \geq 1 \tag{3.29}$$

Similarly, failure criteria for transverse direction can be expressed as follows

$$\frac{\sigma_2^2}{\hat{\sigma}_{2T}\hat{\sigma}_{2C}} + \frac{(\hat{\sigma}_{2c} - \hat{\sigma}_{2T}) \cdot \sigma_2}{(\hat{\sigma}_{2T}\hat{\sigma}_{2C})} + \left(\frac{\tau_{21}}{\hat{\tau}_{21}}\right)^2 \geq 1 \tag{3.30}$$

In case of tensile strength is equal to compressive strength in each longitudinal and lateral direction, equation (3.29) and (3.30) will revert to equation (3.28). Carbon fiber laminate properties used in this project have different tensile and compressive value in both direction, therefore Hoffman failure criteria will be chosen over Tsai – Hill.

Most composite structures are best modeled using shell elements. The total strain can be written in term of mid-plane strain $\varepsilon°$, and the curvature, κ. When z being the coordinate normal to the shell measured from laminate midplane (as shown in Figure 3.9), the following normal and shear strain relationship can be formulated.

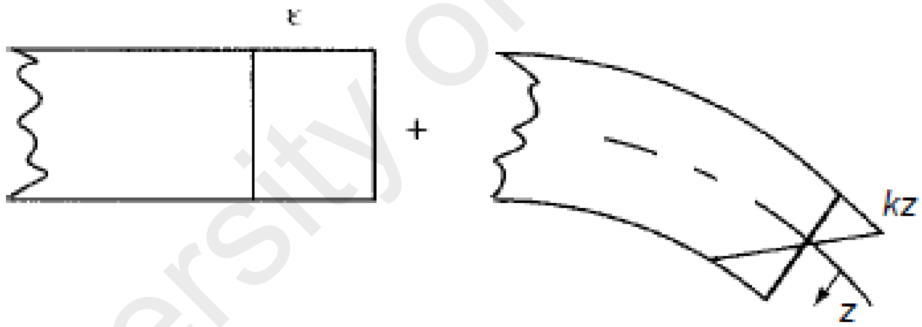

Figure 3.9: $\varepsilon°$ in plane constant over the thickness and $\varepsilon_x = z\ \kappa$, bending strain over thickness.

$$\begin{bmatrix} \varepsilon_x \\ \varepsilon_y \\ \gamma_{xy} \end{bmatrix} = \begin{bmatrix} \varepsilon°_x \\ \varepsilon°_y \\ \gamma°_{xy} \end{bmatrix} + z \begin{bmatrix} \kappa_x \\ \kappa_y \\ \kappa_{xy} \end{bmatrix} \text{ or } \boldsymbol{\varepsilon}_{xy} = \boldsymbol{\varepsilon}° + z\boldsymbol{\kappa} \tag{3.30}$$

Each ply is assuming to have same in-plane strains and curvatures. So, principal stress for any ply, e.g. j[th] layer is given by the following equation,

$$\boldsymbol{\sigma}_{xy,j} = \bar{Q}_j\boldsymbol{\varepsilon}° + z\bar{Q}_j\boldsymbol{\kappa} \tag{3.31}$$

$\bar{Q}_j$ is the transformed stiffness matrix of the layer. The stresses acting in the plane of laminate. These stresses can be converted into equivalent forces acting on a unit width of a shell (e.g. from σ_x, we get $N_{x,j} = \boldsymbol{\sigma}_{x,j} \cdot t$. Here, t is the ply thickness). Adding up resultant of all plies, the total is equal to the external force (per unit width) acting on a shell as shown in Figure 3.10.

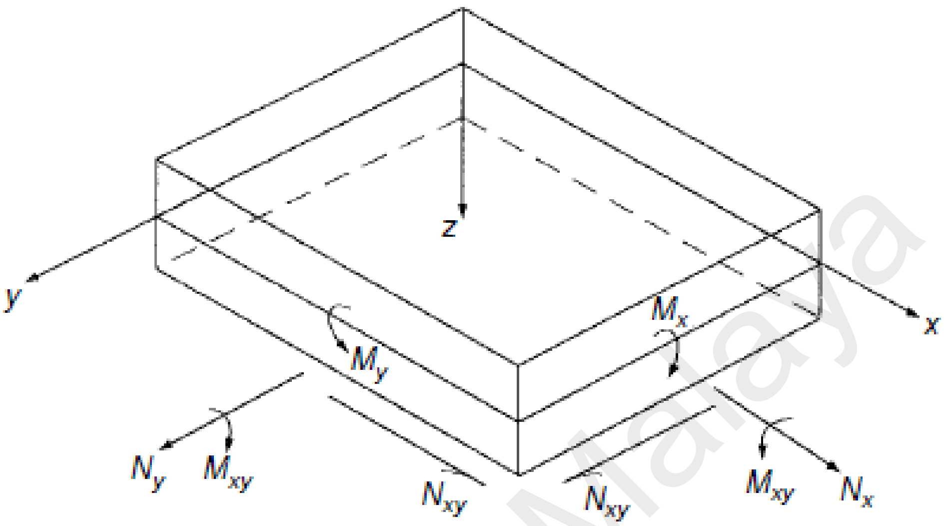

Figure 3.10: Load acting on a laminate.

Similarly, there will be moment (e.g. $M_{x,j}$) about the mid plane due to the equivalent force on a layer. Adding together moments for all plies are equal to external moment (per unit width) acting on a shell element (Figure 3.10). Therefore, relationship of stress resultants to the in-plane strains and curvatures are

$$\boldsymbol{N} = \boldsymbol{A\varepsilon}^{\circ} + \boldsymbol{B\kappa} \tag{3.32}$$

$$\boldsymbol{M} = \boldsymbol{B\varepsilon}^{\circ} + \boldsymbol{D\kappa} \tag{3.33}$$

In expanded form;

$$\begin{bmatrix} N_x \\ N_y \\ N_{xy} \end{bmatrix} = \begin{bmatrix} A_{11} & A_{12} & A_{13} \\ A_{21} & A_{22} & A_{23} \\ A_{31} & A_{32} & A_{33} \end{bmatrix} \begin{bmatrix} \varepsilon^{\circ}{}_x \\ \varepsilon^{\circ}{}_y \\ \varepsilon^{\circ}{}_{xy} \end{bmatrix} + \begin{bmatrix} B_{11} & B_{12} & B_{13} \\ B_{21} & B_{22} & B_{23} \\ B_{31} & B_{32} & B_{33} \end{bmatrix} \begin{bmatrix} \kappa_x \\ \kappa_y \\ \kappa_{xy} \end{bmatrix} \tag{3.34}$$

$$\begin{bmatrix} M_x \\ M_y \\ M_{xy} \end{bmatrix} = \begin{bmatrix} B_{11} & B_{12} & B_{13} \\ B_{21} & B_{22} & B_{23} \\ B_{31} & B_{32} & B_{33} \end{bmatrix} \begin{bmatrix} \varepsilon^{\circ}{}_x \\ \varepsilon^{\circ}{}_y \\ \varepsilon^{\circ}{}_{xy} \end{bmatrix} + \begin{bmatrix} D_{11} & D_{12} & D_{13} \\ D_{21} & D_{22} & D_{23} \\ D_{31} & D_{32} & D_{33} \end{bmatrix} \begin{bmatrix} \kappa_x \\ \kappa_y \\ \kappa_{xy} \end{bmatrix} \tag{3.35}$$

Similar to standard finite element method, A_{21}=A_{12}, etc. These association of elements in the matrices above is as follows;

i. A_{13} and A_{23} relate in-plane direct forces to in-plane shear strain or in-plane shear force to in-plane direct strains.

ii. B_{11}, B_{12}, and B_{22} relate in-plane direct forces to plate curvatures or bending moments to in-plane direct strains.

iii. B_{13} and B_{23} relate in-plane direct forces to plate twisting or torque to in-plane direct strains.

iv. B_{33} relates in-plane shear force to plate twisting or torque to in-plane shear strain.

v. D_{13} and D_{23} relate bending moments to plate twisting, or torque to plate curvatures.

Stiffness matrix [K] and load matrix {F} for a beam element with two degrees of freedom is given by (Moaveni & Saeed, 2008)

$$[K]^{(e)} = \frac{EI}{l^3}\begin{bmatrix} 12 & 6l & -12 & 6l \\ 6l & 4l^2 & -6l & 2l^2 \\ -12 & -6L & 12 & -6l \\ 6l & 2l^2 & -6l & 4l^2 \end{bmatrix}, \{F\}^{(e)} = \begin{Bmatrix} -\frac{wl}{2} \\ -\frac{wl^2}{12} \\ -\frac{wl}{2} \\ \frac{wl^2}{12} \end{Bmatrix} \tag{3.36}$$

Stiffness matrix [K] and load matrix {F} of a quad element of two-dimensional torsional problem is given by (Moaveni & Saeed, 2008)

$$[K]^{(e)} = \frac{w}{6l}\begin{bmatrix} 2 & -2 & -1 & 1 \\ -2 & 2 & 1 & -1 \\ -1 & 1 & 2 & -2 \\ 1 & -1 & -2 & 2 \end{bmatrix} + \frac{l}{6w}\begin{bmatrix} 2 & 1 & -1 & -2 \\ 1 & 2 & -2 & -1 \\ -1 & -2 & 2 & 1 \\ -2 & -1 & 1 & 2 \end{bmatrix}$$

$$\{F\}^{(e)} = \frac{2G\theta A}{4}\begin{Bmatrix} 1 \\ 1 \\ 1 \\ 1 \end{Bmatrix} \tag{3.37}$$

Where w is width, l is the length, E and G are tensile and shear modulus of elasticity respectively.

3.2.3 Composite Optimization Techniques

Computer-aided engineering (CAE) Optimization, in general, is an automated system of searching the minimum or maximum range of responses and formally defined as:

$$\min \boldsymbol{f}(\boldsymbol{x}) = f(x_1, x_2, \dots, x_n) \;\; or \;\; \max \boldsymbol{f}(\boldsymbol{x}) = f(x_1, x_2, \dots, x_n) \tag{3.38}$$

This objective function, $\boldsymbol{f}(\boldsymbol{x})$ are subjected to constraint function, $\boldsymbol{g_j}(\boldsymbol{x})$**,** which both are structural responses obtained from a finite element analysis. g_j^U is the upper limit of the constraint function and *m* being the total no. of constraints.

$$\boldsymbol{g}_{\boldsymbol{j}}(\boldsymbol{x}) - g_j^U \le 0, \qquad j = 1, \dots, m \tag{3.39}$$

There are few terminologies used in optimization; design variables, responses, constraints, and objective. Design variables, $\boldsymbol{X_i}$ are the values that can be changed in the FE model such as shell or solid mesh as well as the dimension (thickness, width, etc.). Design variables for composite can be stated mathematically as

$$X_{ik}^L \le X_{ik} \le X_{ik}^U, \qquad i = 1, \dots, N_p, k = 1, \dots, N_E \tag{3.40}$$

X_{ik} is the thickness of i^{th} super ply of the k^{th} element. N_E represents the no. of elements in a ply and N_p is the no. of super ply in the FE model. Super ply is a definition of arbitrary thickness variation of a ply angle in the stack (Warren Dias, 2011).

Other than that, responses are the values measured in an FE model as results for the boundary condition applied (mass, volume, displacement, stress, etc). Constraints are the limits applied to the responses of a model which need to be satisfied for a feasible design. All these setups are to achieve the objective, which is a single response of the FE model which need to be minimized (or maximized).

In composite, optimization occurred in three phases; conceptual design phase, design fine-tuning phase and ply stacking sequence phase. Optimum shape of a component is constructed through topology optimization technique; which also known as free-size optimization during the conceptual design phase. This shape is determined through material distribution along the load paths within a component with respect to boundary conditions (forces, support, etc.), manufacturing constraints (optional) and global responses (stress, displacement, etc.). Initially, the composite layers are stacked in nominal ply (also known as super ply) with different thickness and angles (orientations). Then, the optimal shapes of each super ply of the component are determined through a process called composite free-size optimization.

The next phase is design fine-tuning phase through size optimization. Size optimization is performed to determine the optimal ply thickness of each ply shape in the stack while considering all design responses and optional manufacturing constraints. In other words, this technique determines optimal thickness through continuous sizing method and later distribute the thickness into a number of plies of each ply shapes through discrete sizing method to satisfy engineering requirements (strength, life cycle, manufacturing requirements, etc.).

Ply stacking sequence phase is the final stage that will perform shuffling optimization of the plies to find best possible stacking sequences which considering all behavior responses and satisfy the component manufacturing requirements is determined using this technique. An overview of the composite design phase and its optimization processes are shown in Figure 3.11. Figure 3.12 described the changes in composite ply during the optimization process.

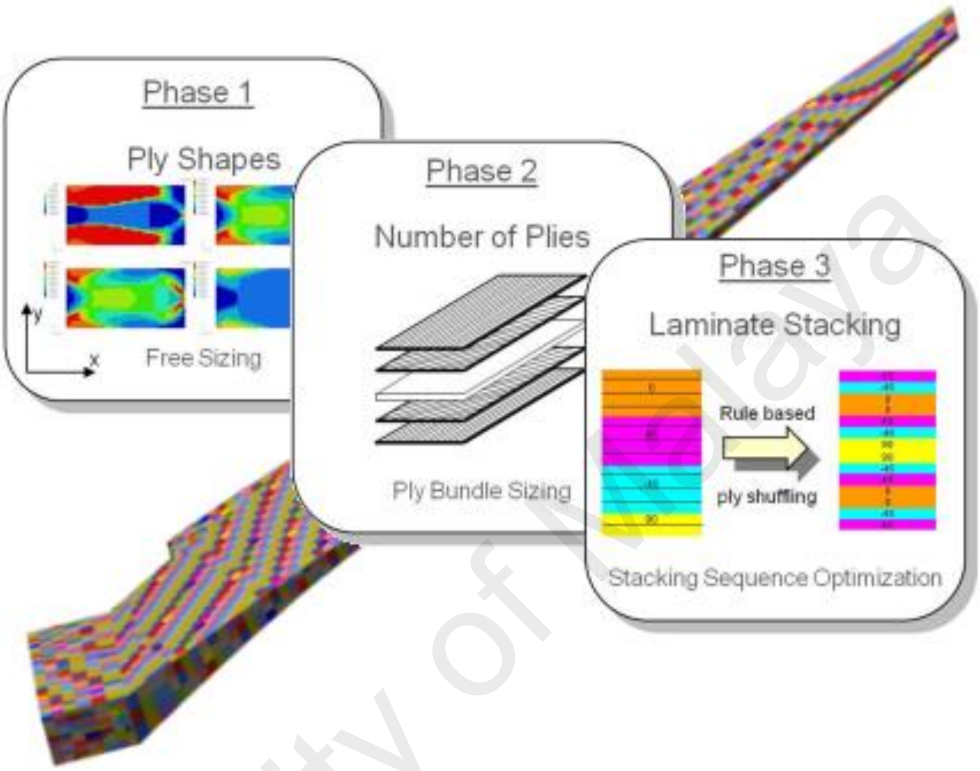

Figure 3.11: Overview of composite optimization phase (www.altair.com)

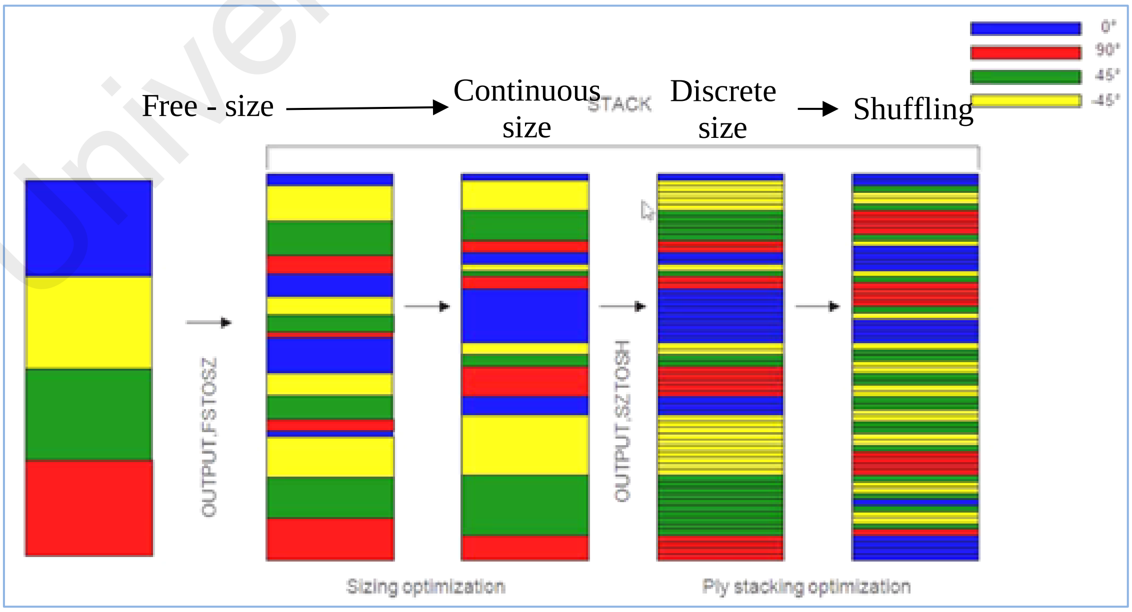

Figure 3.12: Super ply to individual ply in optimized stacking sequence (www.altair.com)

CHAPTER 4: INSTRUMENTATION

4.1 Experimental Modal Analysis Instrumentation

There are three main instruments were used for experimental modal analysis; impact hammer, accelerator, and data acquisition system (DAQ). Basic function, principles of operation and measurement techniques with these instruments will be introduced in this section.

4.1.1 Impact Hammer

Impact hammer is a device used to apply impulsive force in EMA. It has a built-in piezoelectric transducer at the hammerhead, right before the hammer tip. Measurement is based on linear momentum principal whereby impulse is equal to the change in momentum and typically measured in Newton (N). Upon hammering, the force transducer will generate impulse signal (in voltage) that is proportional to the impact force; the signal is subsequently sent to the input channel in data acquisition device.

The frequency content of the applied impulsive force is a function of the stiffness of hammer tip and the hammer mass. Higher frequency content can be obtained by shorter impulse duration i.e. by using hard hammer tip since frequency is the reciprocal of time. The head of the hammer has a threaded hole for installation of three different tips; hard, medium and soft. Hard type is made of stainless steel, medium type from plastic and the soft one is of soft plastic or rubber. The frequency range for the harder tip is generally broader (up to 7000 Hz), while the range is limited up to 500 Hz soft hammer tip.

The hammer mass can also be increased by installing accessories such as a cylindrical head extender on the other side of the hammerhead. Increasing hammer mass will produce higher impulsive force and excitation, which is needed when higher energy at low-frequency range is desired. The impact hammer used in this project is the Dytran 5800B2 which is shown in Figure 4.1. A soft tip was chosen as this experiment are interested in low-frequency range (0 ~ 500 Hz). The hammer will be knocked at roving points with the direction perpendicular to the structure surface.

Figure 4.1: Impact hammer model Dytran 5800B2

This hammer model has high sensitivity (100mV/LbF) and can achieve up to 1.0 % linearity (see appendix A).

4.1.2 Accelerometer

An accelerometer is used to measure the acceleration of motion of a structure or vibration in EMA. The response is typically measured in millivolt per gravity (mV/g) which is later converted to meters per second squared (m/s^2) based on the component datasheet. An ideal accelerometer should be small-sized with a solid body and weight as low as possible to avoid any effect on the FRF measurement.

Accelerometers are either capacitance sensor type or piezoelectric type. Capacitance type senses change of capacitance between microstructures when moved by the accelerative force and translate them into voltage. Most accelerometer, however, follows the piezoelectric effect. Change in the motion of a seismic mass in the sensor will apply a certain amount of pressure on the piezoelectric material which produces an electrical voltage proportional to the force applied. Since the seismic mass is constant, the acceleration is directly proportional to the voltage. Figure 4.2 describe the piezoelectric effect in accelerometer.

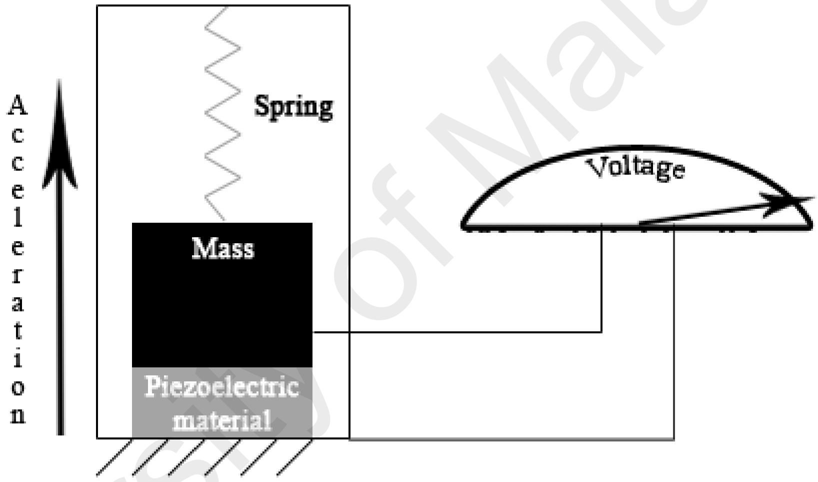

Figure 4.2: Piezoelectric effect in accelerometer

Additional mass (to the structure) from the addition of an accelerometer should be considered in EMA. From equation (3.1), the square root of mass is inversely proportional to the natural frequency; natural frequency will be lower when mass is added to the structure. In order to minimize error, accelerometer's mass should be less than 5% of the structure mass.

The Dytran 3055B2T is a uniaxial integrated electronic piezoelectric (IEPE) accelerometer (Figure 4.3). This type of accelerometer incorporated microelectronics that converts a high – impedance charge signal generated by a piezoelectric sensing element into a usable low-impedance voltage signal that can be readily transmitted, over ordinary two-wire or coaxial cables to any data acquisition system.

Figure 4.3: Uniaxial IEPE accelerometer model Dytran 3055B2T

This accelerometer has a natural frequency which restricted the measurement frequency range to a certain limit. When resonance occurred, its sensitivity rises drastically with a result of the overload of signal output (Figure 4.4).

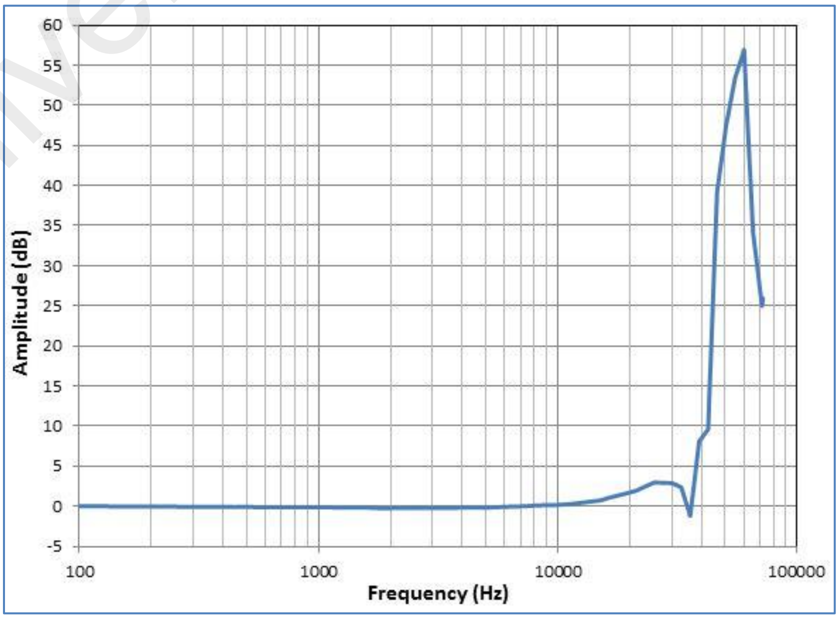

Figure 4.4: Accelerometer output signal at resonance (www.pcb.com)

Particularly compact and lightweight, it only weighed 8.6 grams with 100 mV/g sensitivity. Moreover, it has magnetic mounting making it very easy to mount and move on the structure for all 10 roving points. It is suitable to measure modal analysis within interest range, 1 Hz ~ 500 Hz. Other specifications for the accelerometer are given in appendix B.

4.1.3 Data acquisition system (DAQ)

The signal in form of a voltage generated by both accelerometer and impact hammer is in an analog signal. DAQ converts these signals to the digital signal through the analog-digital converter (ADC) and sends these signal to the FRF analyzing software to be analyzed.

Figure 4.5: OR34 Four channel analyzer

This project used OR34; four-channel real-time analyzer (Figure 4.5) connected to the computer via local area network (LAN) cable. Impact hammer and accelerometer are connected to this DAQ through BNC (Bayonet Neill-Concelman) connectors at two input channels. It has a 24-bit ADC which converts analog to the digital signal in $\pm$ 10 V range with sampling frequency up to 65 kB/s. To ensure the accurate analog signal is being measured, this device has high/low pass filter, stop/passband, as well as integrator and differentiator. However, this DAQ can be only connected to its software; NVGate or Supervisor NETGate.

4.2 FRF analyzer (NVGate software)

NVGate software has a dedicated FFT plugin and tools for the structural model for FRF acquisition. It has a customizable display for frequency response function, coherence, trigger blocks and many more. By using appropriate window setting such as uniform, force/ response, and hanning, a confident result can be acquired. There is accept or reject option in between impact hammer measurement to be chosen after validity check. Hammer impact range can also be set automatically.

FRF measurement can be exported in Universal File Format and MATLAB format to visualize the mode shapes and their modal frequency in third-party software such as ME'scope VES; the software used in this experiment for post-processing.

4.2.1 FRF analyzer setup for EMA.

Experiment setup for EMA is shown in Figure 4.6 below. The equipment consists of cantilever beam plate (structure to measure), clamp, insulation pad, uniaxial accelerometer sensor, impact hammer and FRF analyzer.

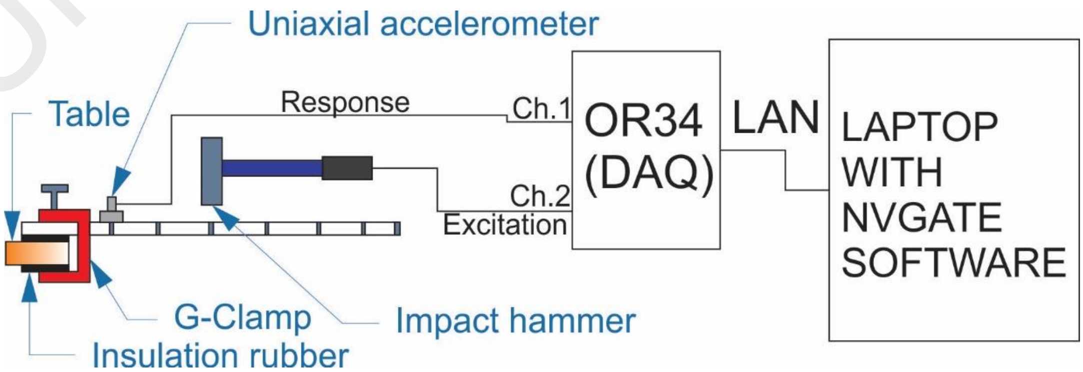

Figure 4.6: EMA hardware setup.

FRF analyzer is consists of data acquisition system (DAQ), LAN cable and laptop with NVGate software set up and running. Impact hammer is connected to input channel 1 and accelerometer is connected to input channel 2. Proper setup for both channels can be configured under Setup > Channels connection menu on top of the screen. Setting used in this experiment are in are in appendix C.

Table 4.1: Channel connection properties

	Label	**Component**	**Node**	**Direction**	**Type**
Input 1	Hammer	Stand Bt	2 (vary)	+Z	Translation
Input 2	Accel Z	Case	3 (fixed)	+Z	Translation
	Transducer	**Physical Qty.**	**Sensitivity**	**Range Pk**	**Ext. Gain**
Input 1	Default Force Sensor	Force	21.515 mV/N	27.9 N	1
Input 2	Default Accelerometer	Acceleration	1.0091 $mV/m/s^2$	99.1 m/s^2	1
	Polarity	**Offset Comp.**	**Coupling**	**Input Filter**	**Enable auto-range**
Input 1	Normal	0 V	ICP	None	On
Input 2	Normal	0 V	ICP	None	On

Data acquisition is normally triggered by the edge detection and the setup used in this experiment is shown in Table 4.2.

Table 4.2: Edge detection properties

	Label	**Source**	**Input Filter**	**Threshold**	**Slope**	**Hold off**	**Hysteresis**
Edge 1	Edge 1	Hammer	None	1N	Rise	0s	0 N

Windowing function will be used for both force and response from impact hammer and accelerometer. Input from impact hammer is using rectangular and output response is using exponential decay window. The graphical user interface (GUI) after setup finish is shown in Figure 4.7. NVGate software is ready for data acquisition process.

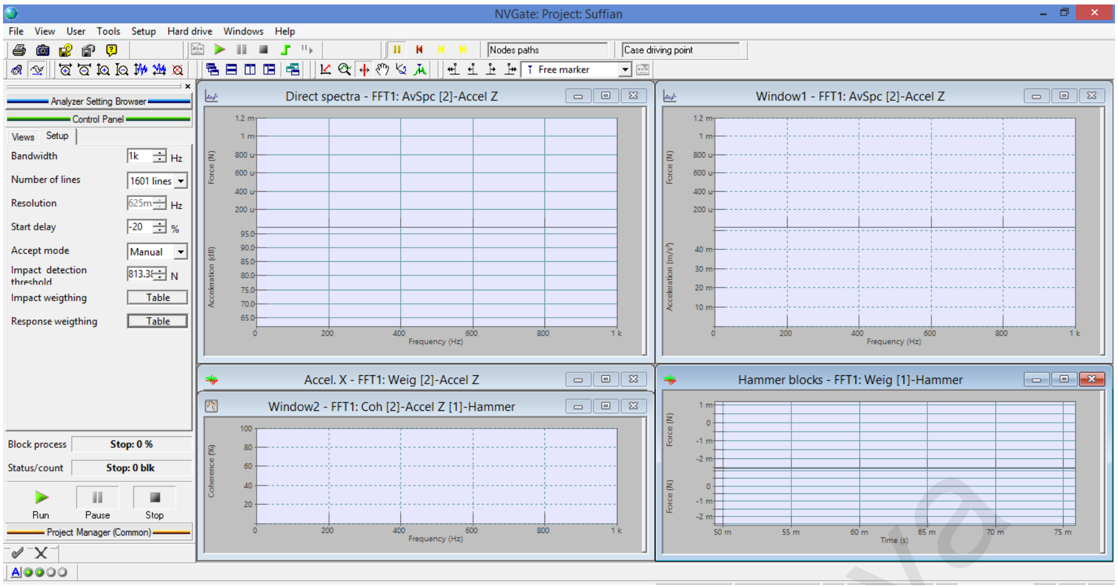

Figure 4.7: FRF analyzer configuration complete

4.2.2 Spectral Leakage and Windowing Function

Spectral leakage is the result of an assumption in the FFT algorithm that the time record is exactly repeated throughout all time and that signals contained in a time record are thus periodic at intervals that correspond to the length of the time record. If the time record has a nonintegral number of cycles, this assumption is violated, and spectral leakage occurs. Spectral leakage distorts the measurement in such a way that energy from a given frequency component is spread over adjacent frequency lines. Windowing function can be used to minimize the effects of performing an FFT over a nonintegral number of cycles (Cerna & Harvey, 2000).

Common windows are rectangular (also known as boxcar or uniform), hanning, flat top, and exponential decay. The rectangular window is same as applying no windows. This is suitable for the signal from impact hammer as the signal starts and end at zero value within the recorded time frame. Hanning and flat top are suitable for steady-state signal i.e. continuous vibration signal from rotating machinery. Exponential decay window can be used for acceleration signal in EMA which requires suppressing the tail end to zero.

4.3 3D Scanning for Reverse Engineering.

This project requires reverse engineering process for reconstructing CAD data of an aftermarket steel strut bar. Reverse engineering is a process of constructing an exact 3D CAD data from an actual object, which can be used for simulation, design improvement, manufacturing, etc.

The physical model is digitized into the point of clouds; set of data points using 3D scanners which later converted into the polygonal mesh to increase the model accuracy. These data can be used for inspection; comparing the physical object with its CAD model to measure the accuracy of the manufactured product. For reverse engineering where the CAD model is unavailable, the 3D model can be constructed from the polygonal mesh (typically saved in STL format) using CAD software which has reverse engineering modules such as CATIA, Solidworks, Polyworks, Geomagic and ANSYS SpaceClaim. Process flow chart of reverse engineering is shown in Figure 4.8.

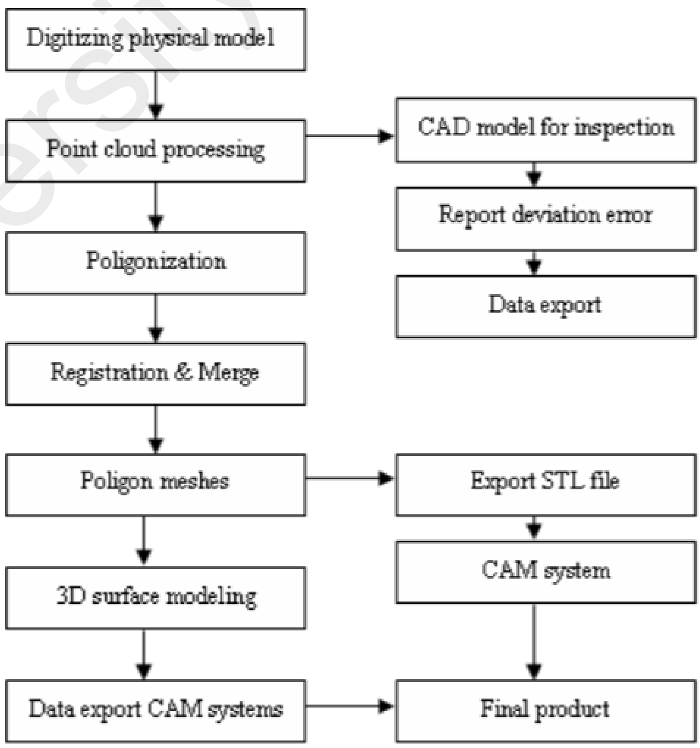

Figure 4.8: Reverse engineering processes

Typical procedures for reverse engineering is as follows (Kuş, 2009);

- Sensor calibration (if necessary)
- Preparation of part to be scanned (apply non-reflective spray for shiny surface, clamp on jig or fixture if necessary)
- Conducting 3D scanning process for physical model digitization.
- Point cloud processing and noises cleaning from scan data
- Merging point clouds (if there are multiple data due to part or tracker relocation)
- Translating point clouds into polygonal mesh and save into STL (stereolithography) format
- 3D CAD modeling for solid or surface reconstruction for CAE or computer-aided machining (CAM)

4.3.1 Handheld optical 3D laser scanner

Handheld optical 3D laser scanner Steinbichler Zeiss T-Scan CS and large volume optical tracker model Steinbichler Zeiss T-Track LV (see Appendix D) have been used for reverse engineering. Handheld 3D scanner T-Scan is a non-contact type which emits laser lines to scan the object surfaces and the CCD/CMOS camera lens on the scanner will measure the time the laser takes to hit the surfaces and reflect back to the sensor as the speed of light, c is precisely known. This system is capable to measure the laser travel distance from million pulses of the laser in picoseconds. Hence, this method is called time of flight (Figure 4.9).

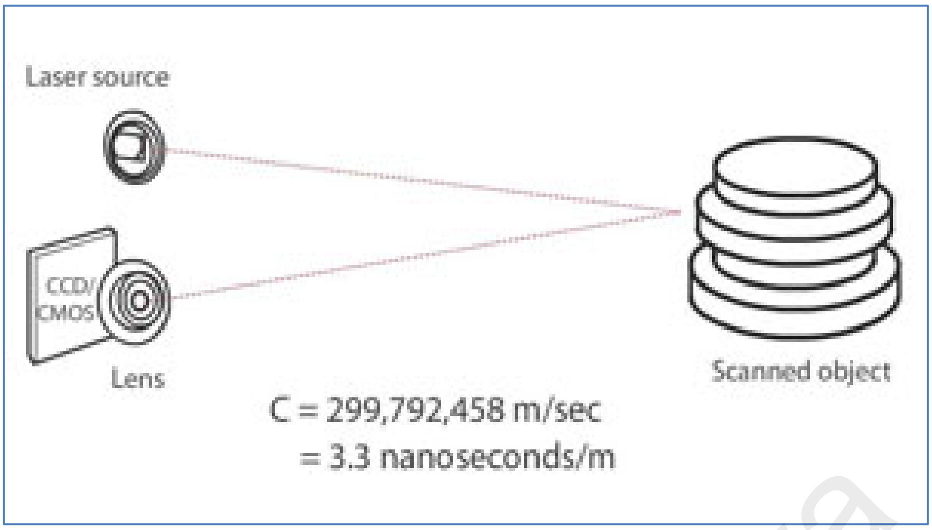

Figure 4.9: Time of flight technique (www.geomagic.com)

If travel time or round-trip time, t is measured, then the actual distance, d between the object and the scanner is

$$\boldsymbol{d} = c \cdot \frac{t}{2} \tag{4.2}$$

Time for light to travel, c for 1 millimeter is approximately 3.3 picoseconds. By moving the handheld scanner, view from different angle can be taken. In order to accurately measure the scanner location and orientation, few LED markers were positioned on each antenna-like feature surrounding the handheld scanner, acting as reference points (Figure 4.10).

Figure 4.10: Handheld optical 3D laser scanner model Steinbichler Zeiss T-Scan CS (http://optotechnik.zeiss.com/)

Optical tracker T-Track LV positioned about 1.5 to 7.5 meter from the scanner will track the position and orientation of these markers (at corner right of Figure 4.11 below). Since this is a large volume tracker, it can measure up to 35-meter square of measuring volume with up to 3.7 m x 2.6 m field of view. Therefore, scanning process will be much easier as less or even no repositioning of parts or tracker is required and more freedom of movement.

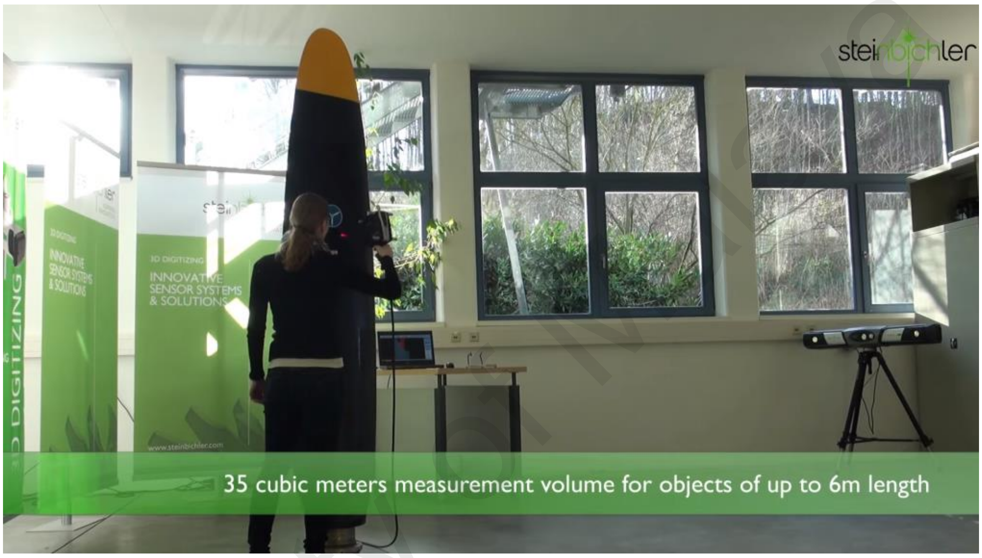

Figure 4.11: Optical tracker T-Track LV at right corner of the photo (http://optotechnik.zeiss.com/)

CHAPTER 5: RESEARCH METHODOLOGY

The overall process flow of this project is visualized in Figure 5.1. Beginning with conducting the literature review and reverse engineering of steel strut bar, an experimental modal analysis will be conducted to validate the FE model. Simulation on steel strut bar needs to be conducted to have benchmarking data for simulation and improvement activities on composite strut bar.

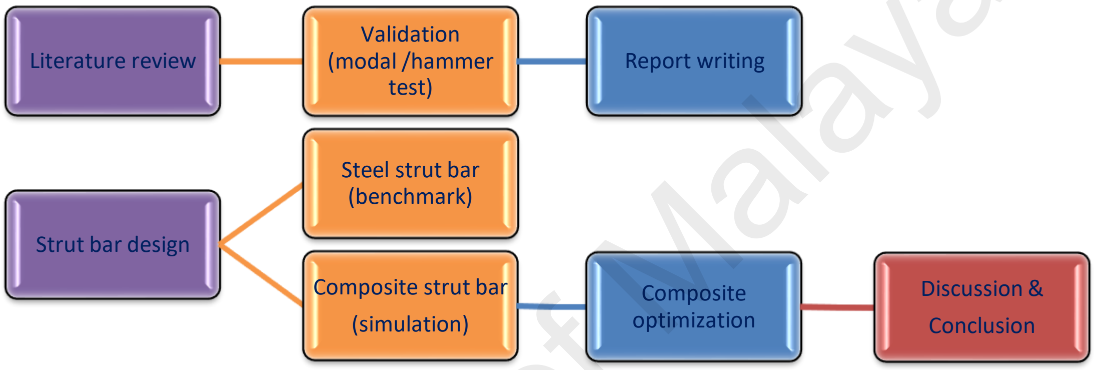

Figure 5.1: Research methodology flowchart.

The result from the steel bar dynamic analysis is validated through experimental modal analysis. FEA simulation of is fine-tuned until a good correlation with the experimental result is gained. Composite optimization needs to be conducted to identify the best configuration of the composite layer that enhances the performance of strut bar.

5.1 EMA methodology

EMA can be described in three main steps; experiment setup, data acquisition, and post-processing result.

Step 1: Experiment setup

Solid steel beam plate is clamped 160 mm from one end to a rigid structure (e.g. sturdy table using G-clamp with insulation rubber pads between the clamp and the plate to isolate external vibration. Total beam length is 660 mm with 160 mm fixed and 500 mm free on the other end. The plate is 2.6 mm thick and 30 mm width. There are 10 roving points distributed equally at the centerline of the beam with 50 mm distance in between. Sufficient amount of measurement point is important to ensure the normal mode can be modeled properly in post-processing. The hammer will be impacted at consistent speed and angle at the roving point and will be moved to other roving points after each measurement while the accelerometer will be fixed at 1 point (point 3 in this experiment). Impact hammer is set as input 1 and accelerometer as input 2.

DAQ is connected to the power supply and the laptop using LAN cable. Impact hammer cable is connected to the input channel 1 of DAQ while the uniaxial sensor is connected to the input channel 2.

Step 2: Data acquisition using OROS NVgate software

Proper configuration setting for impact hammer (Dytran 5800B2) and accelerometer (Dytran 3055BT) in FRF analyzer NVGate are presented in section 4.2. Experiment data can be recorded by clicking "Run". Hammer is impacted on vertical (Z-direction) on a roving point to generate an impulsive force. The vibration response was measured with an accelerometer fixed at point 3 in the Z (vertical) direction. Since each impact point was different, the DOFs corresponding to the force are called Roving DOFs. The accelerometer was fixed at DOF 3Z throughout the test; 3Z is called the Reference DOF. All cross-channel measurements should have a Roving and a (fixed) Reference DOF, denoted as; Measurement DOF = Roving DOF: Reference DOF. There should be 10 FRF measurements made in this experiment.

The average FRF spectral data such as result of magnitude, phase and coherence can be observed on the NVGate software. Green tick and red cross at the bottom will be prompted after each hammering, for accept or reject to repeat the measurement. The validity of each data measured need to be checked, by ensuring the average coherence is above 90% and repeated up to 5 times to minimize error. On top of that, the average FRF should have an adequate impact to excite all frequency range as presented in section 3.1.3. Figure 5.2 below shows an example of inadequate and adequate impact throughout the frequency range.

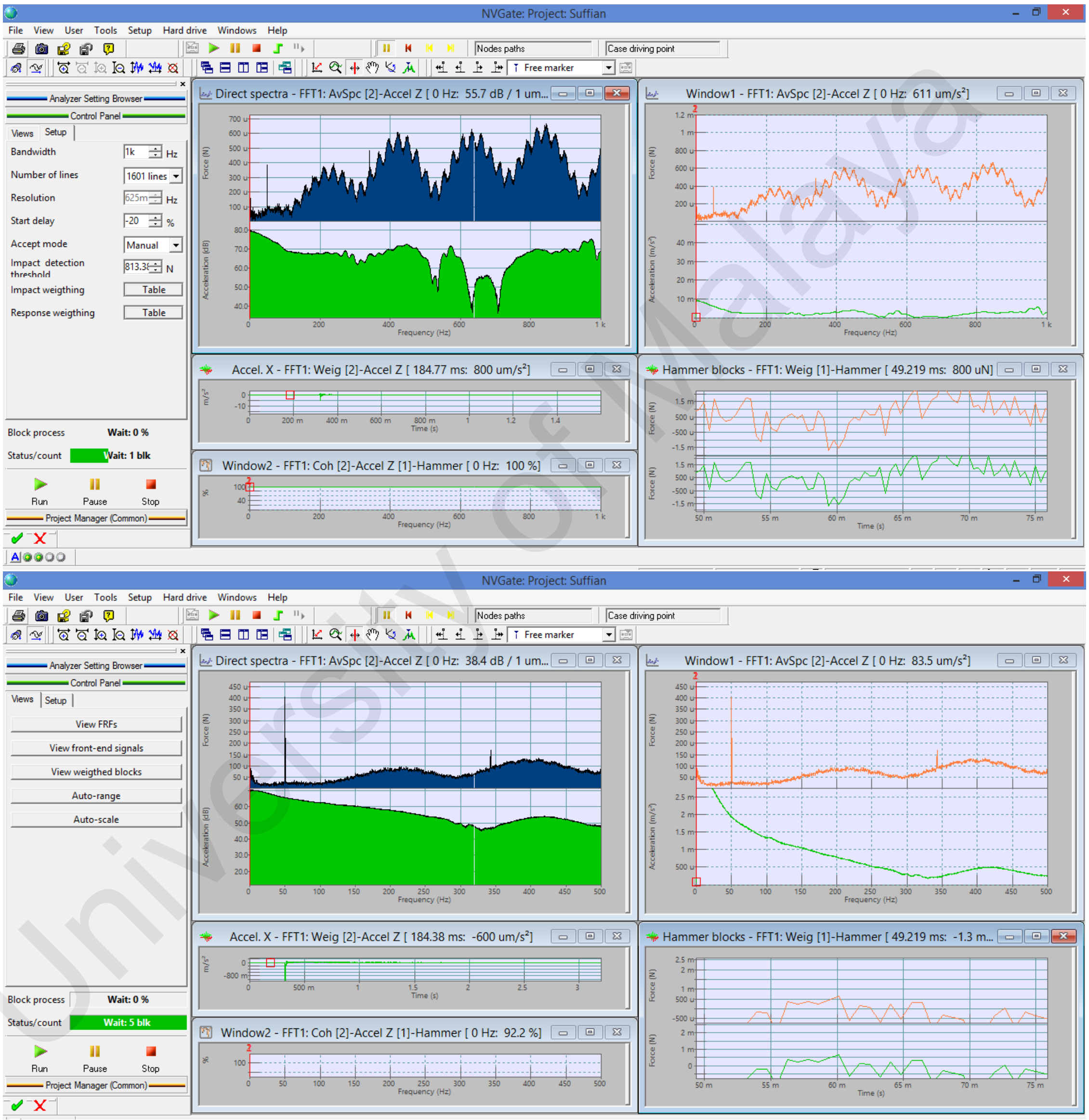

Figure 5.2: Inadequate (top) and adequate impulsive force

After 5 measurements completed, the data should be saved in correct naming format. For instance, when the impact hammer is knocked in at point 1 (roving point) and the accelerometer measured the response at point 3 (reference point), the data should be saved as ‘1Z_3Z.uff’. This is to ease the process in post-processing result in Me’Scope software.

Step 3: Post-processing result

After 5 measurements completed, the data should be saved in correct naming format. For instance, when the impact hammer is knocked in at point 1 (roving point) and the accelerometer measured the response at point 3 (reference point), the data should be saved as '1Z_3Z.uff'. This is to ease post-processing process in Me'Scope software.

Step 3: Post-processing result

The structure is modeled in Me'Scope according to the dimension. Measurement points were numbered according to the experiment setup where the accelerometer and impact force positioned. Result from NVGate software can be imported into Me'Scope through File > Import > Data Block. The list of result files (rovingDOF_referenceDOF.uff) from NVGate is selected and imported into Me'Scope with its naming format. All measurements were overlaid together in a single graph with obvious FRF peaks (if the measurement is correct) can be observed.

These FRF measurements later assigned to the modeled structure. Mode shape can be displayed through "animate" function. Each normal mode shape can be displayed by moving the peak cursor frequency band to another peak in the overlaid FRF curves. These peaks are the natural frequencies of the structure. The displacement of each mode shape can be scaled up or down to appropriate animation visualization. All imported data block, structure geometry, and animation were saved in *.VTprj format for future use.

5.2 Reverse engineering of steel strut bar

Strut bar should be clean and shiny surfaces should be coated with non-reflective spray. Strut bar will be placed firmly on a table facing the optical tracker. Proper positioning for maximizing scannable surface in one shot should be planned to minimize the number of surface data due to part repositioning. In this project, scanning process was completed with two sets of surface data; top faces and bottom faces of strut bar.

Hardware configuration of reverse engineering is shown in Figure 5.3. It consists of computer, optical tracker and handheld 3D optical scanner.

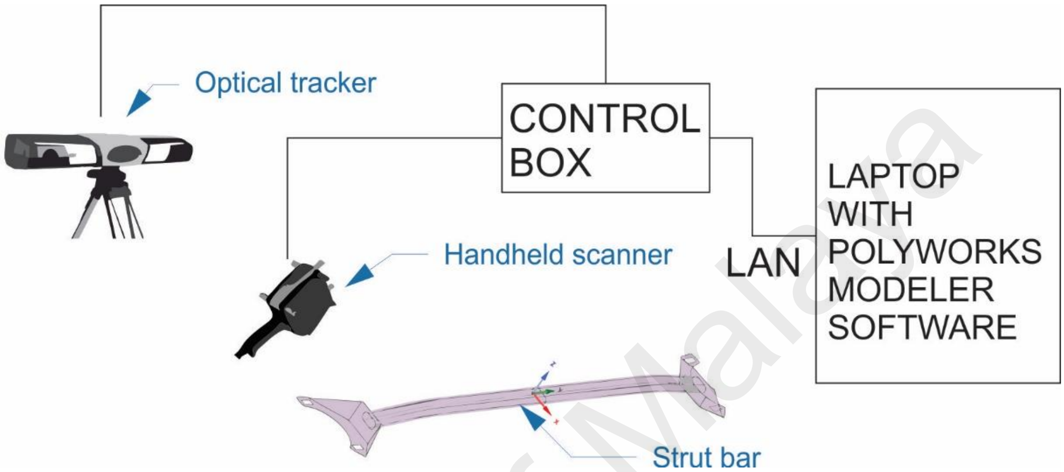

Figure 5.3: Reverse engineering hardware setup

Using Polyworks Modeler software, 3D scanning process to digitize the strut bar surface is conducted. Figure 5.4 shows the interface of Polyworks Modeler.

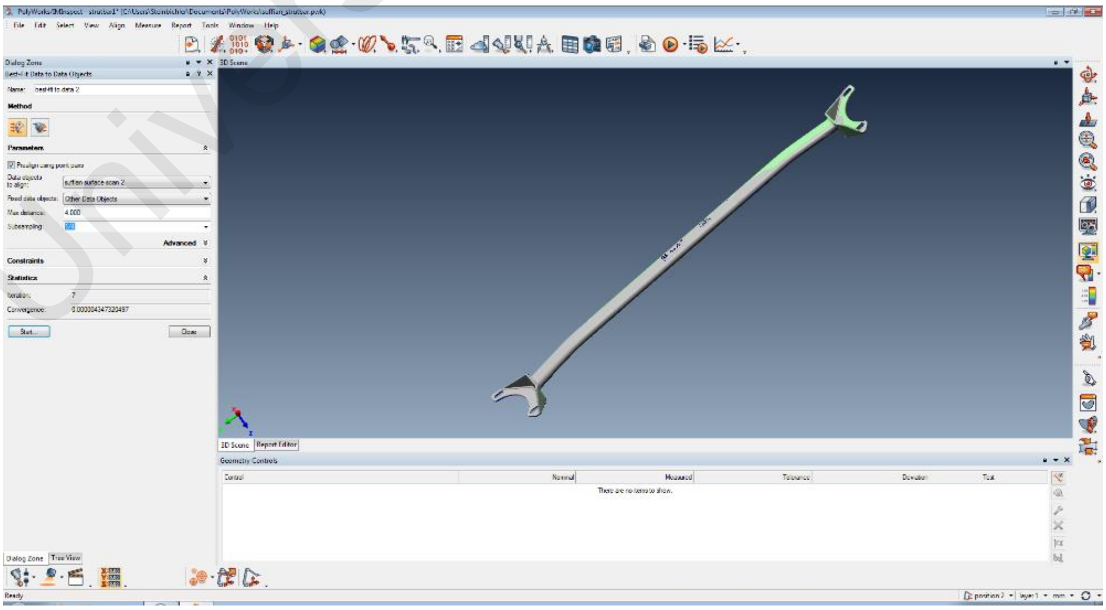

Figure 5.4: Polyworks Modeler GUI

The layout of the experiment is as shown in Figure 5.5. Surface data is imported into CAD modeling software to reconstruct the 3D model of the component. ANSYS SpaceClaim is the CAD software used in this project. Figure 5.6 shows the scanned data in cloud point that was cleaned up and converted in the triangular mesh (*.STL) format and Figure 5.7 is the final design of strut bar. CAD data is converted into mid surface for FE modeling. Mounting bracket thickness in 4.7 mm and bar thickness is 1.3 mm.

Figure 5.5: Layout of reverse engineering experiment

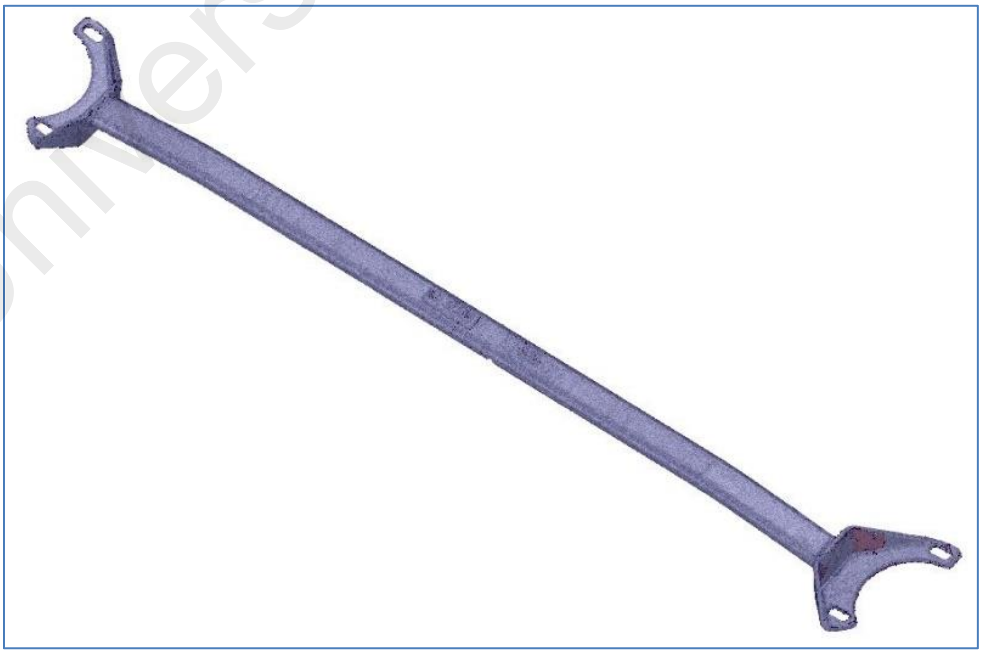

Figure 5.6: Cloud of points in STL format.

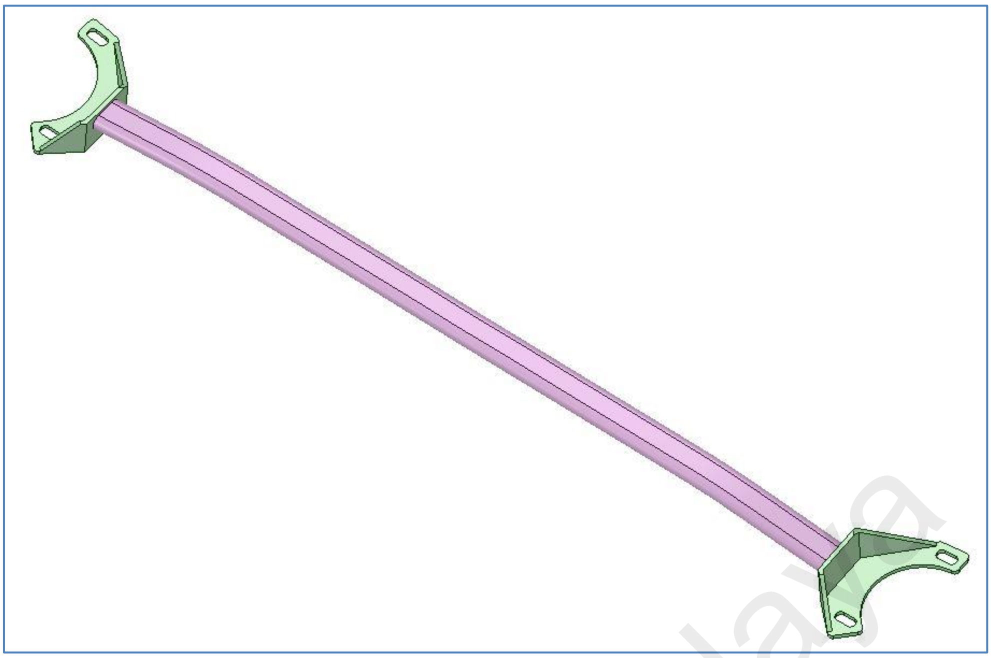

Figure 5.7: Final CAD design.

5.3 Modal analysis of carbon fiber and steel cantilever beam.

A carbon fiber beam with the same dimension of the steel plate (550 mm x 25 mm x 6 mm) was modeled to get a rough estimation of undamped natural frequencies and their mode shape of a cantilever beam as shown in the figure below. Standard material properties of Toray 300 UD with matrix Toray Semi-Toughen 350°F epoxy resin in Table 5.1 below is normalized to 60% fiber volume (Appendix E). Material properties are taken from manufacturer's data sheet and published data (Matthews, 2003).

Table 5.1: Material properties for Toray 300 UD CFRP.

Properties	**Value**	**Comments**
Ply thickness, t	0.1334 mm	ASTM D5947 - 11
Density, rho	1.76e-09 tonne/mm^3	ASTM D792 − 13
Modulus of elasticity in longitudinal direction, E_{11}	130e+03 MPa	ASTM D-3039
Modulus of elasticity in lateral direction, E_{22}	8.96e+03 MPa	ASTM D-3039
Poisson ratio for uniaxial loading, v_{12}	0.3	ASTM D-3039
In-plane shear modulus G_{12}	7.1+03 MPa	ASTM D-3518
Tensile in X-direction, X_t	1760 MPa	ASTM D-3039

Compressive in X-direction, X_c	1570 MPa	ASTM D-695
Tensile in Y-direction, Y_t	80 MPa	ASTM D-3039
Compressive in Y-direction, Y_c	80 MPa	ASTM D-695
In-plane shear strength, S	98 MPa	ASTM D-3518
Inter-Laminar Shear Strength (ILSS)	108 N/mm^2	ASTM D-2344
Tensile Strain	1.3 %	ASTM D-3039

For steel cantilever beam, a standard isotropic material property for steel (Table 5.2) is used for modal analysis simulation.

Table 5.2: Material properties of steel

Properties	**Value**	**Comments**
Thickness, t	2.6 mm	ASTM A1073
Density, rho	8e-09 tonne/mm^3	Typical for steel
Modulus of elasticity, E	195e+03 MPa	ASTM E111
Poisson ratio, ν	0.29	ASTM E132
Shear modulus of elasticity, G	86e+03 MPa	ASTM E143-13
Ultimate tensile strength	505 MPa	ASTM E111
Yield strength, Y_s	215 MPa	ASTM E111

20 layers of 0.1334 mm ply thickness with different fiber orientation and stacking sequence of unidirectional (UD) carbon fibers were configured in the simulation and compared to steel 2.6 mm thickness beam. Normal modes were observed up until 5th mode. Steel bar simulation result is compared to the theoretical frequency value and mode shape and validated through EMA. As for composite, the result is validated through correlation with the published result (Tita et al., 2003).

The cantilever beam (660 mm x 30 mm x 2.6 mm) was meshed using 5 mm QUAD element. 50 mm from one edge of the beam (consist of 10 x 5 QUAD elements) were fixed on all x, y, z translational and rotational degree-of-freedom (Figure 5.8). There are nine different stacking sequences, all in the same direction, or 0° pair with various ply angle, or positive-negative angle alternately arranged for ply orientation in order to balance the configuration as (Table 5.3).

Table 5.3: Ply orientation

Simulation No.	Stacking Sequence	Total no. of plies
1	0° / 0°	20
2	0° / 30°	10 / 10
3	0° / 45°	10 / 10
4	0° / 60°	10 / 10
5	0° / 90°	10 / 10
6	-30° / 30°	10 / 10
7	-45° / 45°	10 / 10
8	-60° / 60°	10 / 10
9	90° / 90°	20

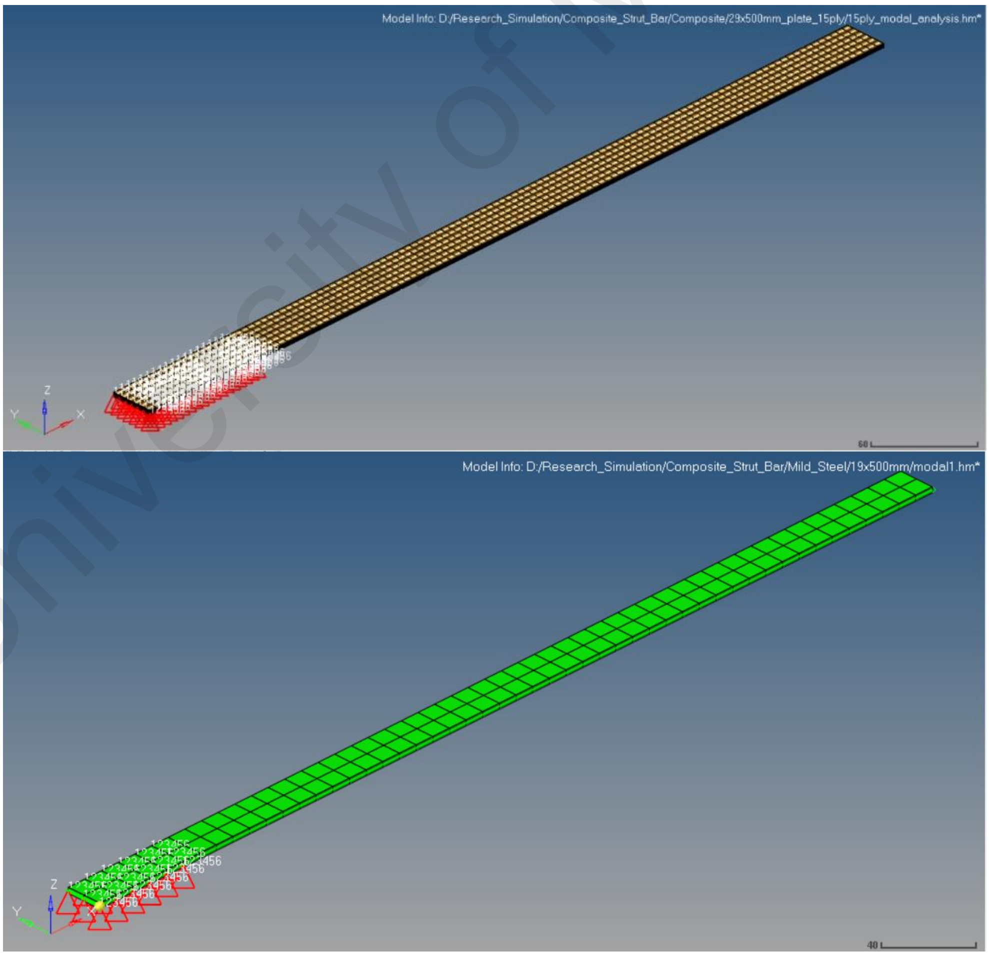

Figure 5.8: Cantilever beam FE model setup for a composite plate with 0-degree ply orientation (top) and similar setup for steel plate (bottom).

All beam will have same 20 plies or layers. Visualization of ply setup in this FE model is shown in Figure 5.9.

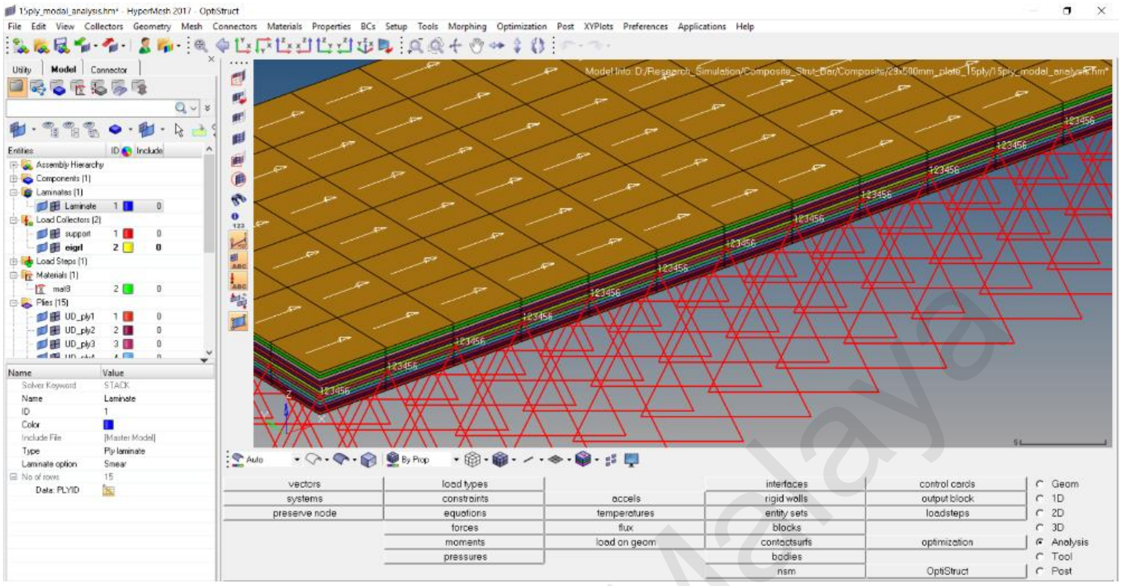

Figure 5.9: Ply stacking visualization and orientation

5.4 Abusive static loading test.

Moving forward, the CAD data of benchmarked steel strut bar obtained from reverse engineering process (presented in section 5.2) will undergo the same normal mode analysis. On top of that, static performance should also be observed to ensure the performance of carbon fiber strut bar has equivalent or better performance than steel strut bar while reducing weight. Since every car chassis has different structural stiffness, a standard static loading test needs to be performed.

Static loading tests in this simulation were considered abusive as the load applied is high enough to observe the part deflection under extreme load. Loading applied is the standard test from the part manufacturer to observe relative performance with other aftermarket strut bar hence cannot be considered as the actual operating load applied on the part. There were three tests conducted; compression test, torsion test, and flexural test. Based on FE model, the total weight of steel strut bar is 1.67 kg, which is very close to actual weight (Figure 5.10).

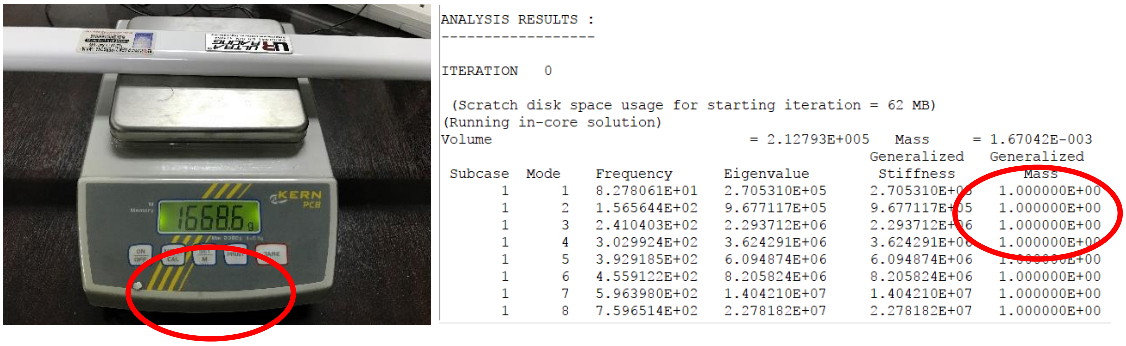

Figure 5.10: Actual part weight (1668 gram) and simulation mass (1.67e-03 tonne)

5.4.1 Performance evaluation method

Safety factor, *N* for each static loading test is determine from

$$N_{ductile} = \frac{YS}{\sigma_v} \tag{5.1}$$

where

$N_{ductile}$: Factor of safety for ductile material

YS : Yield strength [MPa]

σ_v : Von Mises stress [MPa]

Shown above is the safety factor calculation for steel and other ductile material. Typically, the design is considered safe if the safety factor value is above 1.5 under the normal loading condition. This test is considered as abusive as the strut bar might experience deformation after the test. On the other hand, CFRP is a brittle material. Therefore, a different method of safety factor calculation being used.

$$N_{brittle} = \frac{UTS}{\sigma_1} \tag{5.2}$$

Where

$N_{brittle}$: Factor of safety for brittle material

UTS : Ultimate tensile strength [MPa]

σ_1 : First principal stress [MPa]

On top of that, stiffness value, k for each load case was also evaluated. Stiffness can be determined by

$$k = \frac{F}{\delta} = \frac{1}{C} \tag{5.3}$$

Where

F : Force acting on the body [N]

δ : Displacement [mm]

C : Compliance [mm/N]

Compliance result of each load case is summarized in the *.out file in the simulation folder. This value represents the highest compliance at the highest displaced node. Stiffness is the inverse value of compliance.

5.4.2 Compression test

A simulation performed to evaluate the deflection and stress of strut bar when an impact is applied from the lateral direction. Rigid element (RBE2) was applied and fixed all six degrees of freedom (DOF) around each bolt on one side. On the other side, 100 psi or 0.6895 N/mm^2 of pressure was applied towards lateral direction (X-axis for this FE model). Graphical representation of simulation is shown in Figure 5.11.

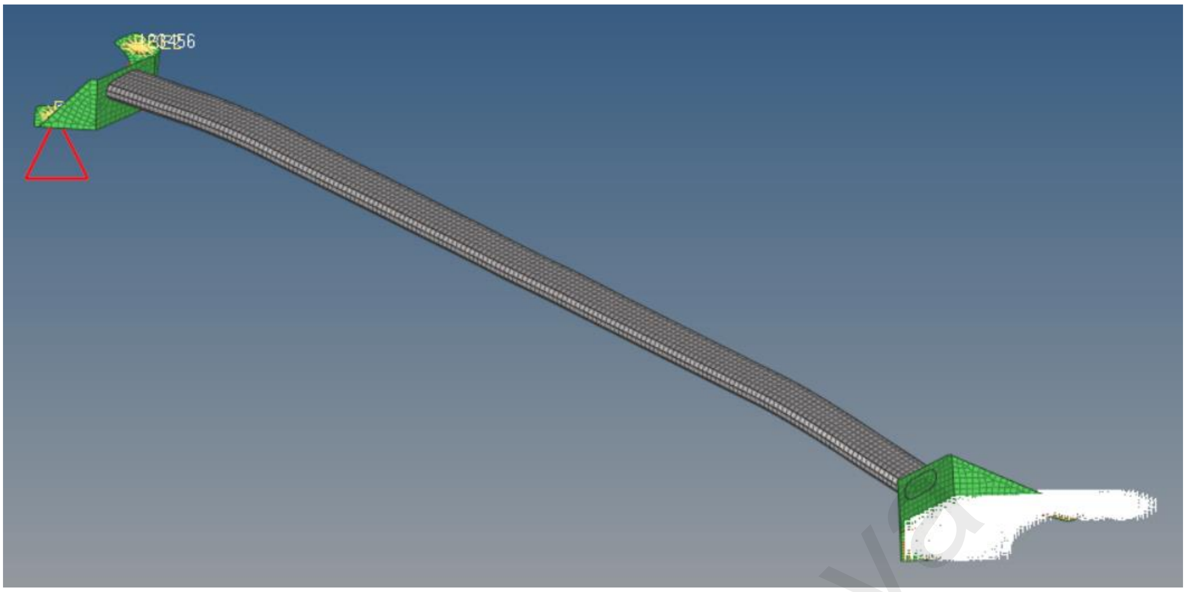

Figure 5.11: FE model setup for compression test

This test is similar to the test conducted using a compression test jig (Figure 5.12)

Figure 5.12: Compression test jig (ultraracing.my)

5.4.3 Torsion test

Torsion test was simulated to identify maximum deflection occurred when a torque is applied from the transverse axis. In this test, 78500 N.mm of torque was applied to simulate the condition 8 kg of mass was applied from a distance of 1 meter on the transverse axis using torsion test jig (Figure 5.13 and Figure 5.14).

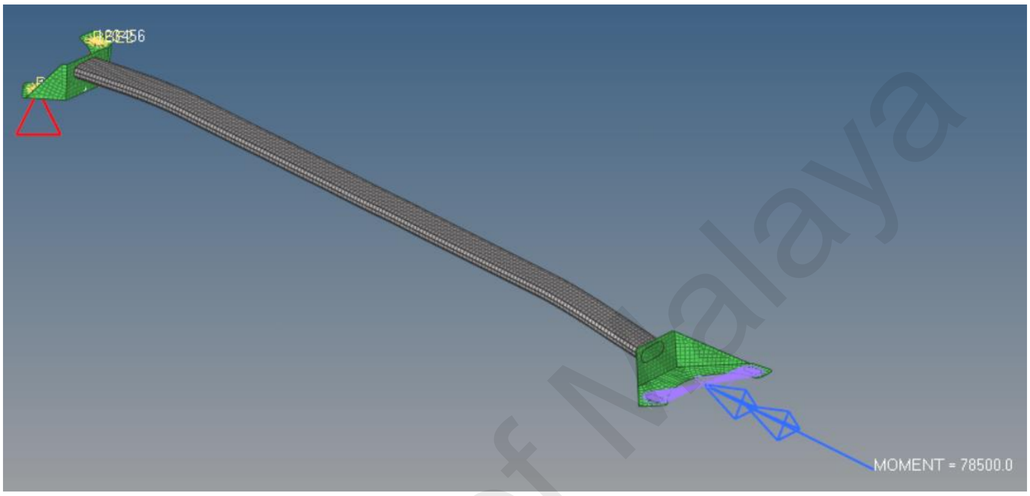

Figure 5.13: FE model setup for torsion test

Figure 5.14: Torsion test jig (ultraracing.my)

5.4.4 Flexural test

The flexural test was simulated to determine deflection when a torque is applied to the longitudinal axis. Similarly, 78500 N.mm of torque will be applied about Y-axis at bolt mounting on the strut in order to simulate the test on flexural test jig (Figure 5.15 and Figure 5.16).

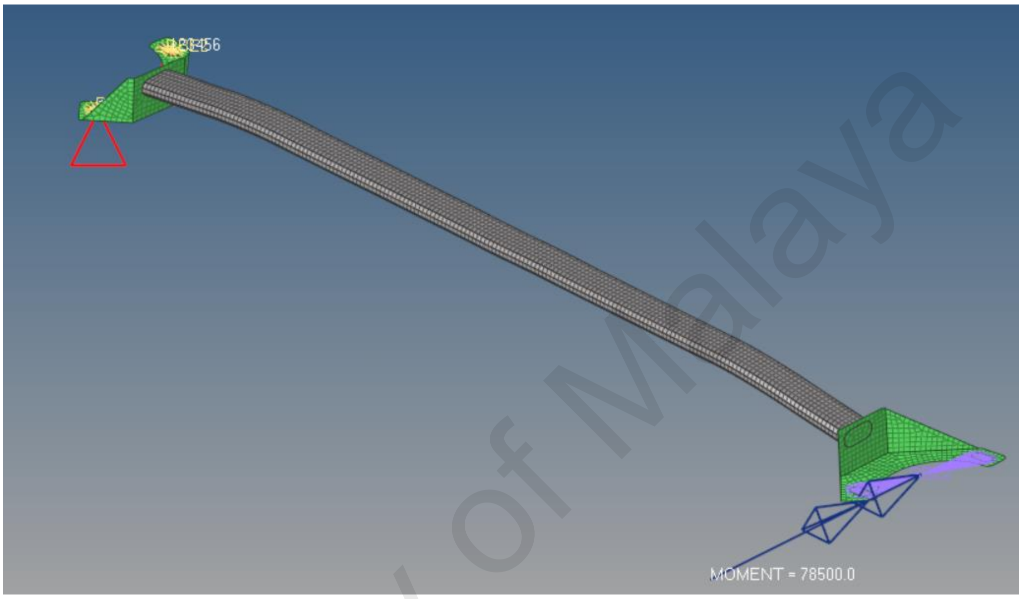

Figure 5.15: FE model setup for flexural test

Figure 5.16: Flexural test jig (ultraracing.my)

5.5 Carbon fiber optimization

Phase 1: Free Size (Topology) Optimization Setup

The first step in free size optimization is the ply configuration. This includes the thickness and orientation (0°, ±45°, ±90°, etc.) of each composite layer or ply. These plies are initially stacked on each other in a thick ply with different orientation, namely super ply. Then the plies are stacked or glued into a laminate. Here, 'smear' is the recommended laminate option as it neutralized the effect of stacking sequence (Figure 5.17). For element properties, it is recommended to use PCOMP card for an efficient process of switching plies or using a different type of design.

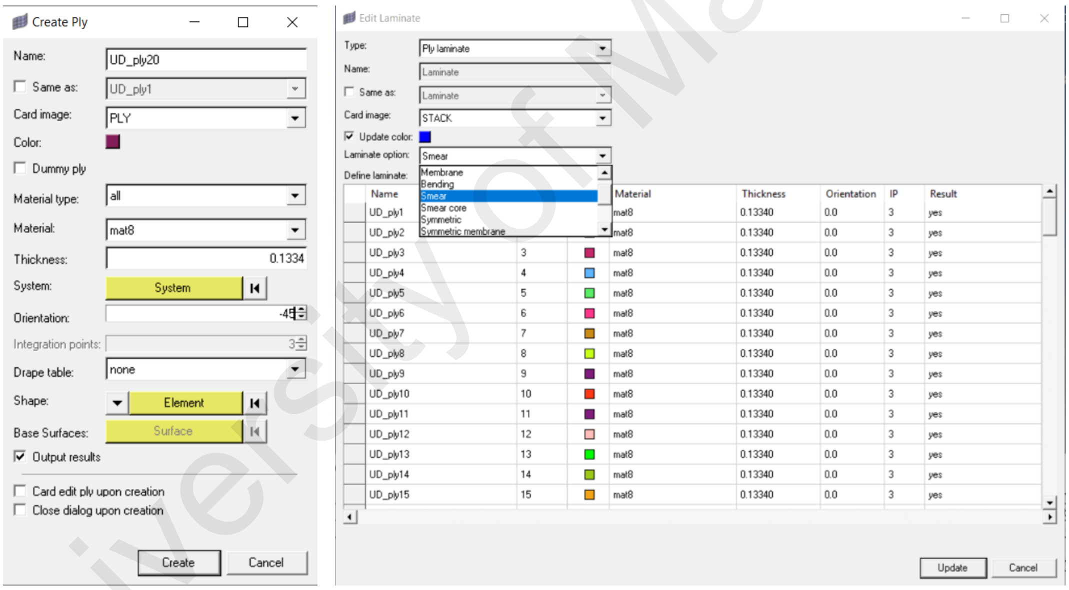

Figure 5.17: Ply (-45 unidirectional)   Laminate with Plies Stack definition

Later, boundary condition such as where the force is applied, and location of the supports are defined (Figure 5.18)

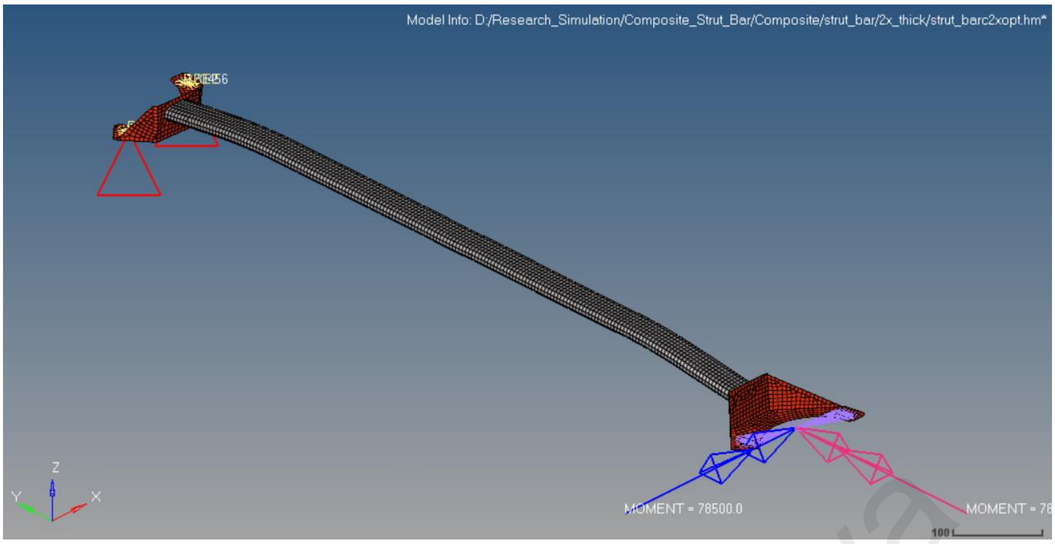

Figure 5.18: Boundary condition setup

An essential element in optimization is the design variable. Stacked plies are chosen as the design variables with manufacturing constraints, such as beam thickness (MEMBSIZ), pattern repetition type (PTRN) and min / max total composite laminate thickness (LAMTHK). Ply manufacturing constraint (PLYMAN) and balanced ply angles (BALANCE) also can be defined (Figure 5.19).

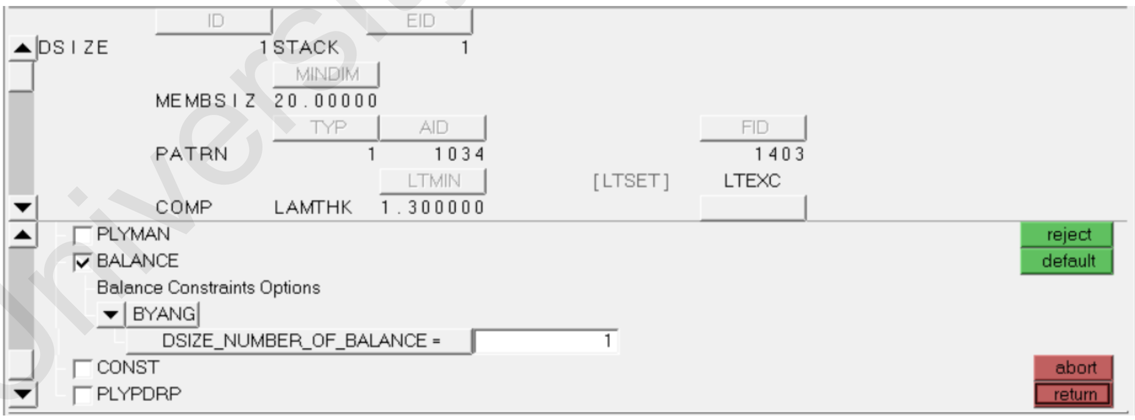

Figure 5.19: Design variable setup

Other than that, the typical setup for free size optimization has been used in this project which has design constraint, i.e. limit the volume fraction and also objective, i.e. minimize the weighted compliance with volume fraction is less than 80% (Figure 5.20 and 5.21). This is because when compliance is minimized, stiffness will be maximized.

Figure 5.20: Design constraint (maximum volume fraction is 0.8)

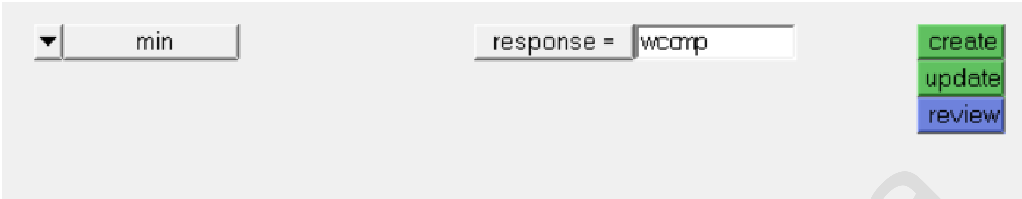

Figure 5.21: Objective (minimize compliance)

In order to move to the next process with free-size ply shape given in this phase, FSTOSZ (free-size to size optimization) control card should be selected under Analysis > control card > output and change the no. of output to 2 with menu selection below; for ply shape result display in post processor Hyperview (*.H3D file format) and for automatic generation of plies for sizing optimization (Figure 5.22). FSTOSZ will subdivide the design variables into separate plies for each ply shape and orientation (Figure 5.23).

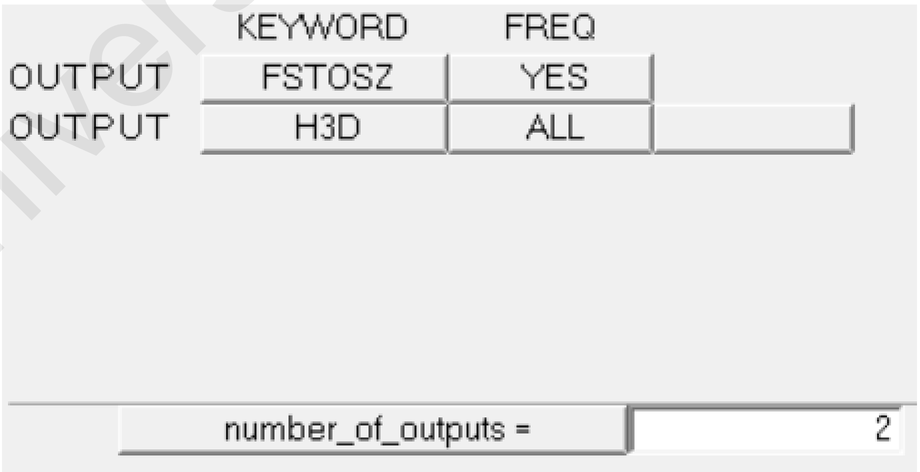

Figure 5.22: Output option for size optimization

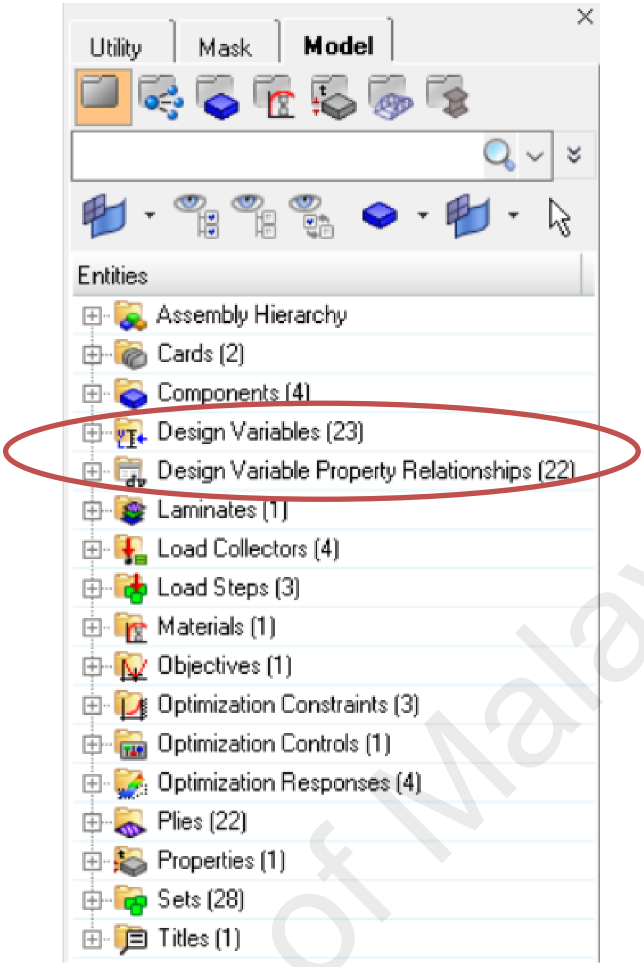

Figure 5.23: Single design variables is subdivided by FSTOSZ control card into each design variables and their property relationship

Phase 2: Ply Bundle Sizing Optimization Setup

The result of free size optimization will require designer's interpretation according to manufacturing feasibility. As an example from Figure 5.24, initial ply shapes from free size optimization can be interpreted into a combination of three individual ply. In this case, the super ply has now become three super plies. These changes will affect the strength or mass of a component, hence requires size optimization in the design fine-tuning phase. This process will identify the optimal thickness of each ply bundle.

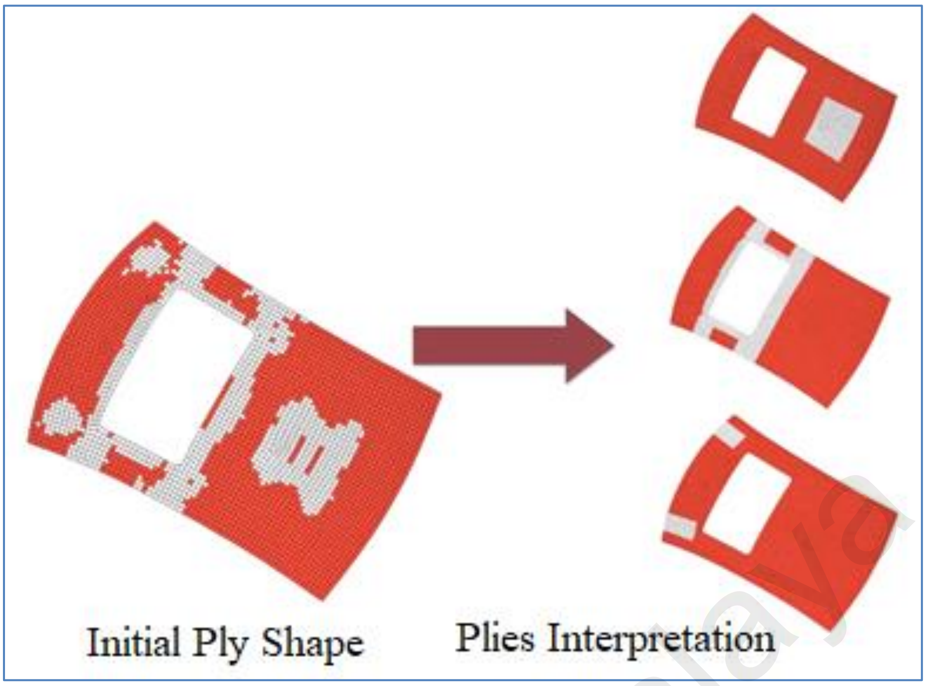

Figure 5.24: Design interpretation from optimal ply shape

Similar to free size, the condition of plies is still in a bundle during continuous size optimization stage but later "sliced" into few no. of plies according to the user with an optimal yet manufacturable shape in discrete size optimization stage. Design constraint such as maximum displacement or volume fraction and objective such as minimize mass or compliance still applied according to user preference. Composite behavior such as ply failure is also considered at this phase. Manufacturing constraints considered in phase 1 are carried over into this design phase through FSTOSZ control card.

Phase 3: Shuffling Optimization Setup.

Ply shape and stacking details for the design in phase 2 are not fully comply to manufacturing requirement or design regulation, such as maximum no. of successive plies with same ply angle, pairing the +/- degree ply angles and sequence of core and cover (outer layer/ ply), therefore require shuffling optimization on the ply stacking sequence. This phase will optimize the sequence to meet those manufacturing constraints while preserving the component behavior and performance. Figure 5.25 below show the difference between the final design of discrete ply bundle sizing optimization in phase 2 and the final stacking result from shuffling optimization.

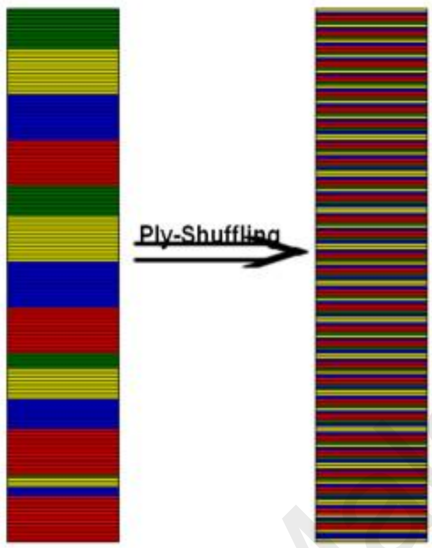

Figure 5.25: Shuffling Optimization.

Shuffling optimization requires the user to change the control card from FSTOSZ to SZTOSH to maintain formulation from bundle ply sizing optimization to this phase. Design variable for size optimization "desvar_size" is renamed to “desvar_shuffle” and can be edited through Analysis > optimization > composite shuffle > parameters (Figure 5.26 below) to apply manufacturing constraints such as pairing constraint and maximum successive plies.

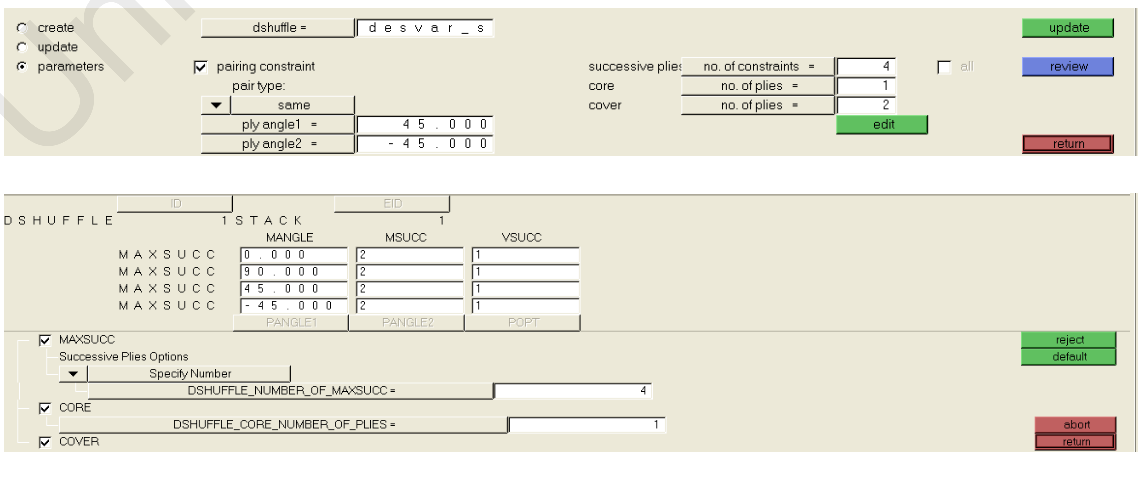

Figure 5.26: Design variables setup for shuffling optimization.

CHAPTER 6: RESULT INTERPRETATION AND DISCUSSION

Result and discussion of this research project are organized as follows:

i. Experimental modal analysis of steel cantilever beam

ii. Modal analysis of steel cantilever beam

iii. Modal analysis of different ply thickness of CFRP cantilever beam

iv. Modal analysis of different ply orientation of CFRP cantilever beam

v. Modal analysis of CFRP strut bar

vi. Static loading of strut bar

vii. Optimization of CFRP strut bar

6.1 EMA of cantilever beam

There are 10 points on cantilever beam are analyzed and modeled in Me'Scope. When all 10 FRF of Z-direction were overlapped together, five peaks were observed below the 500Hz range. Figure 6.1 and Figure 6.2 showed the result of natural frequency and their respective mode shapes. Fourth and fifth modes are less obvious due to soft plastic hammer tip used and hammering technique which requires more practices(Avitabile, 2001).

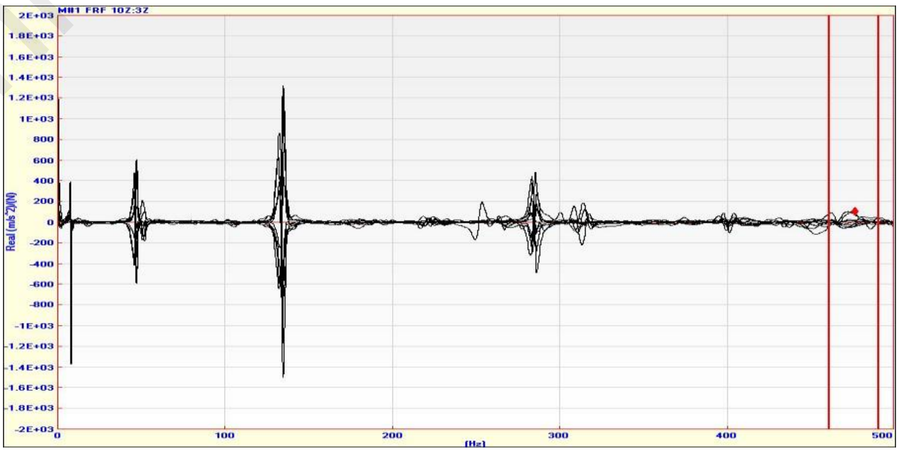

Figure 6.1: FRF from EMA of steel cantilever beam showing five peaks

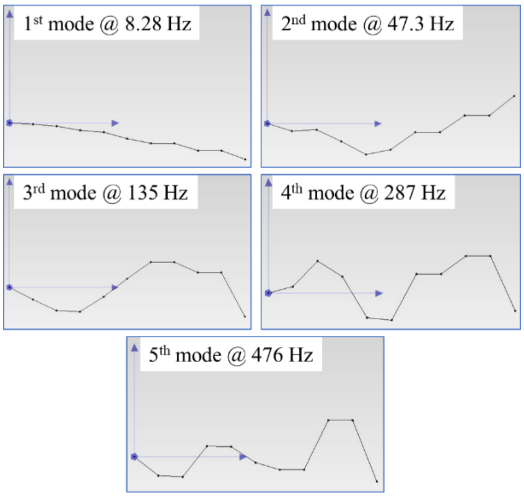

Figure 6.2: Experimental mode shape and natural frequencies of cantilever beam

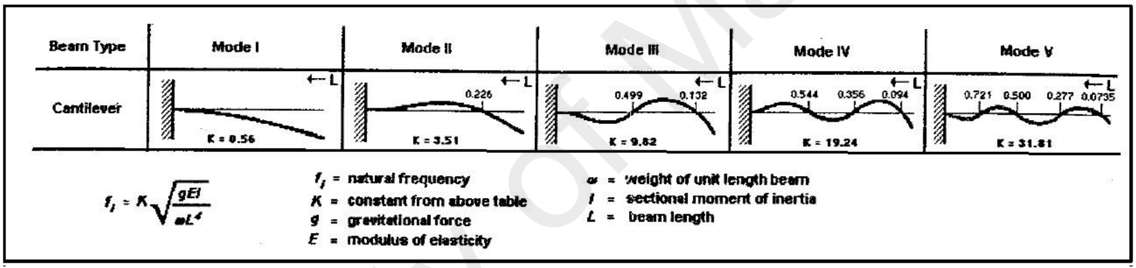

Figure 6.3: Theoretical result for transverse vibration of beam (Church, 1964)

Using Rayleigh method (Figure 6.3), mode shapes and natural frequencies, f [Hz] of cantilever beam can be calculated based on following equation (Church, 1964);

$$f = K\sqrt{\frac{gEI}{wL^4}} \tag{6.1}$$

Where

K: Constant for different modes. K=0.56 for mode 1, K=3.51 for mode 2, K=9.82 for mode 3, K=19.24 for mode 4 and K=31.81 for mode 5.

g: Gravity acceleration, 9.81 [m/s^2]

I: Moment of inertia of cantilever cross sectional area [m^4]

E: Modulus of elasticity of cantilever beam [Pa]

w: Weight per unit length of cantilever beam [N/m]

L: Length of cantilever beam [m]

Parameters for steel cantilever beam used in this experiement are as follows:

i. Dimension = 0.66 m x 0.03 m x 0.0026 m
ii. Weight = 0.41 kg
iii. Free length from clamp position = 0.5 m

Therefore,

$$I = \frac{0.03 \times 0.0026^3}{12} = 4.39 \times 10^{-11} [\, m^4] \qquad (6.2)$$

$$w = \frac{0.41 \times 9.81}{0.66} = 6.09 \left[\frac{N}{m}\right] \quad E_{steel} = 195 \times 10^9 \; [Pa] \qquad (6.3)$$

$$L = 0.5\, m \qquad f = \mathrm{K}\sqrt{\frac{(9.81)(195 \times 10^9)(4.39 \times 10^{-11})}{6.09 \;\times 0.5^4}} \qquad (6.4)$$

Comparison between theoretical and experimental result is shown in Table 6.1 below. Error percentage ranging from 0% to 9.3% with average error is 3.7%. Percentage error is high at mode 2 and 3 possibly due to distortion of data in the frequency domain that can be minimized through a proper setup of windowing function (Avitabile, 2001). Tati (2003) pointed out error can also from the positioning of the accelerometers and their mass, the position of roving points and non-uniformity in the specimen's properties (uneven thickness or width, etc.), other than measurement noises.

Table 6.1: Comparison of theoretical and experimental result for EMA

Mode	*f* (analytical) [Hz]	*f* (experiment) [Hz]	% error
1	8.30	8.28	0.5%
2	52.1	47.3	9.3%
3	145.9	135.0	7.5%
4	285.8	287.0	0.4%
5	472.6	476.0	0.7%
Average error %			3.7%

6.2 Modal analysis of steel cantilever beam

Modal analysis simulations were conducted with Altair Optistruct to observe natural frequency and mode shape of a steel cantilever beam; the result is then compared to theoretical value as discussed in section 6.2. As shown in Table 6.2, there are five transverse modes (vertical bending with respect to the Z-direction) below the 500 Hz range. Percentage of error of experimental result compared to theoretical value is shown in Table 6.2; good correlation is achieved with an error less than 0.2%. The average percentage of error, when compared to experiment result, is 3.9%. The weight of the steel cantilever beam is 410 and 412 grams for actual and simulated weight, respectively.

Table 6.2: Comparison of analytical and simulation result for modal analysis of steel cantilever beam

Mode	f (theory) [Hz]	f (simulation) [Hz]	% error (simulation – analytical)	% error (simulation – experiment)
1	8.30	8.30	0.0%	0.2%

2	52.1	52.2	0.1%	10.4%
3	145.9	146.0	0.1%	8.1%
4	285.8	286.2	0.1%	0.3%
5	472.6	473.5	0.2%	0.5%
Average error %			0.1%	3.9%

For benchmarking purpose, modal analysis for steel cantilever beam was conducted up until 1000 Hz. There are total of seven transverse modes, two lateral modes (horizontal bending with respect to the Y-direction) and two torsion modes (twisting about the X-axis). The details of natural frequency and mode shape for each mode are discussed in the next section. These data will be compared against the CFRP cantilever beam result.

6.3 Modal analysis of different thickness of CFRP cantilever beam

Normal modes are observed at 10, 15, 20, 25 and 30 plies of carbon fibers, each weighing at 47, 70, 93, 116 and 139 g, respectively. Normal modes are observed under 1 kHz frequency range for a different number of ply thickness with 0°/0° ply orientation. The objective of this simulation is to identify the relationship between ply thicknesses and natural frequency. Details of the modal analysis result of different ply thickness are shown in Appendix F. Mode shapes in Figure 6.4 to 6.6 are arranged in sequence; the left figure is the first mode shape and right figure is the last mode shape within the 1000 Hz frequency range.

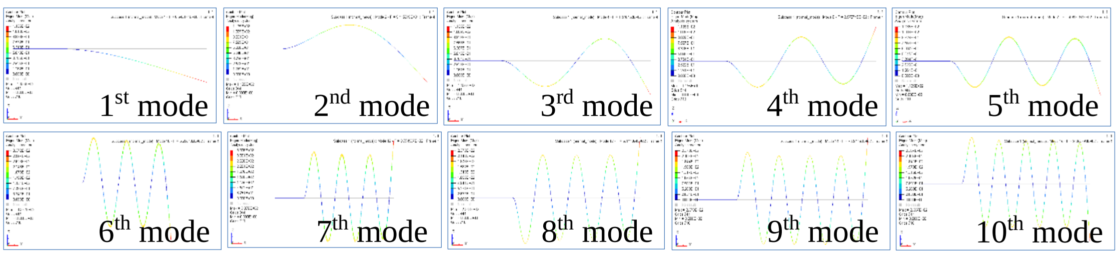

Figure 6.4: Transverse vibration modes

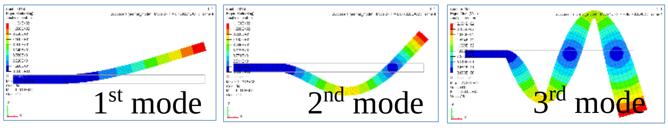

Figure 6.5: Lateral vibration modes

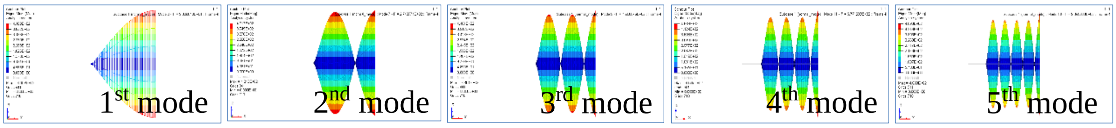

Figure 6.6: Torsional vibration modes

Summary of modal analysis of different thickness of CFRP cantilever beam for transverse modes (Z-axis) is shown in Figure 6.7.

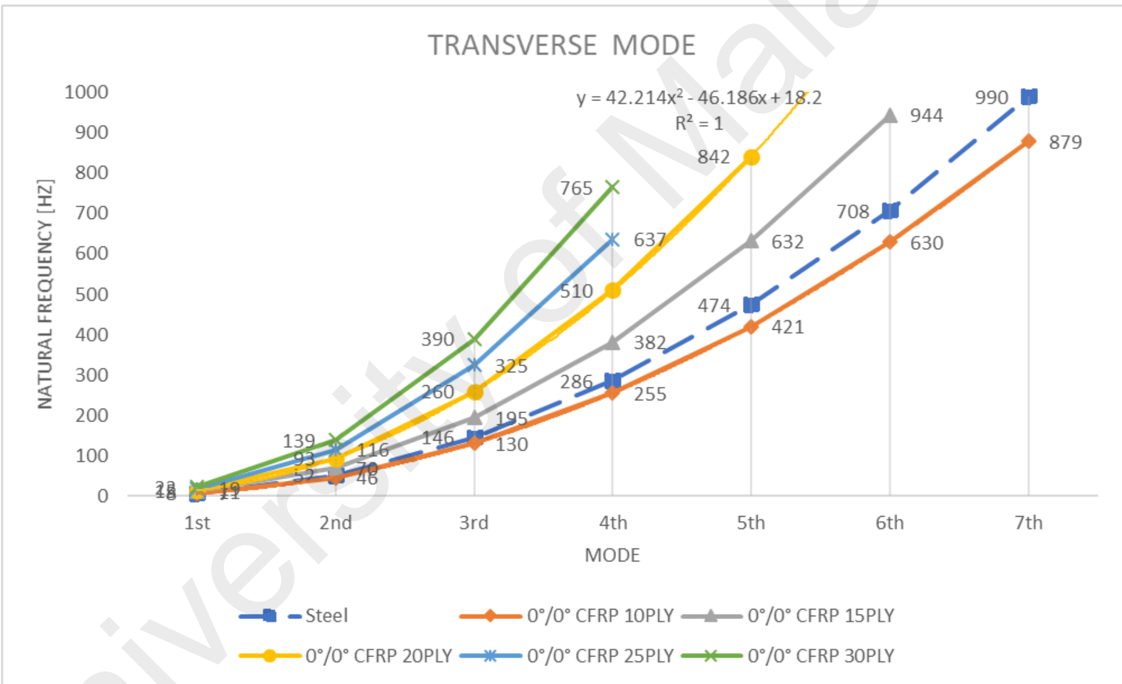

Figure 6.7: Transverse vibration modes for different ply thickness

Natural frequency for each mode increases as the number of ply increases because of the increase of the effective elasticity modulus for the beam (Mohammed, 2013). The result of each ply can be perfectly represented by a quadratic equation where R^2=1. As the number of plies increase, the stiffness of CFRP beam increases, hence the number of normal mode below 1kHz decreases.

The result of lateral modes (Y-axis) and torsional modes (about the X-axis) are shown in Figure 6.8~6.9. While torsion modes show a similar trend with transverse modes across ply thicknesses, the lateral modes show no change in natural frequency regardless of the ply thicknesses.

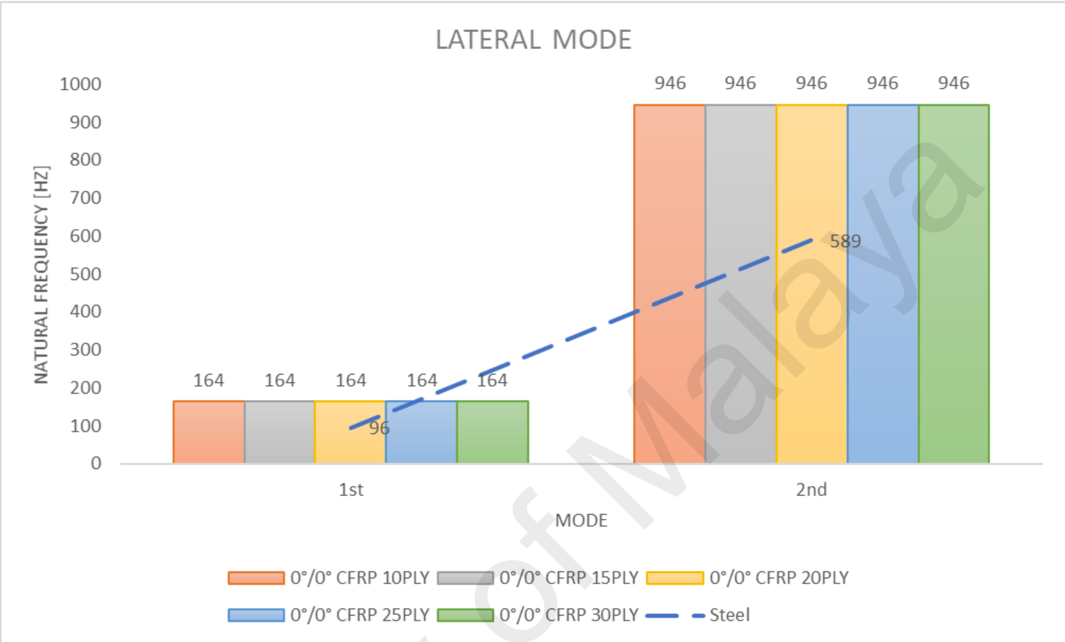

Figure 6.8: Lateral vibration modes for different ply thickness

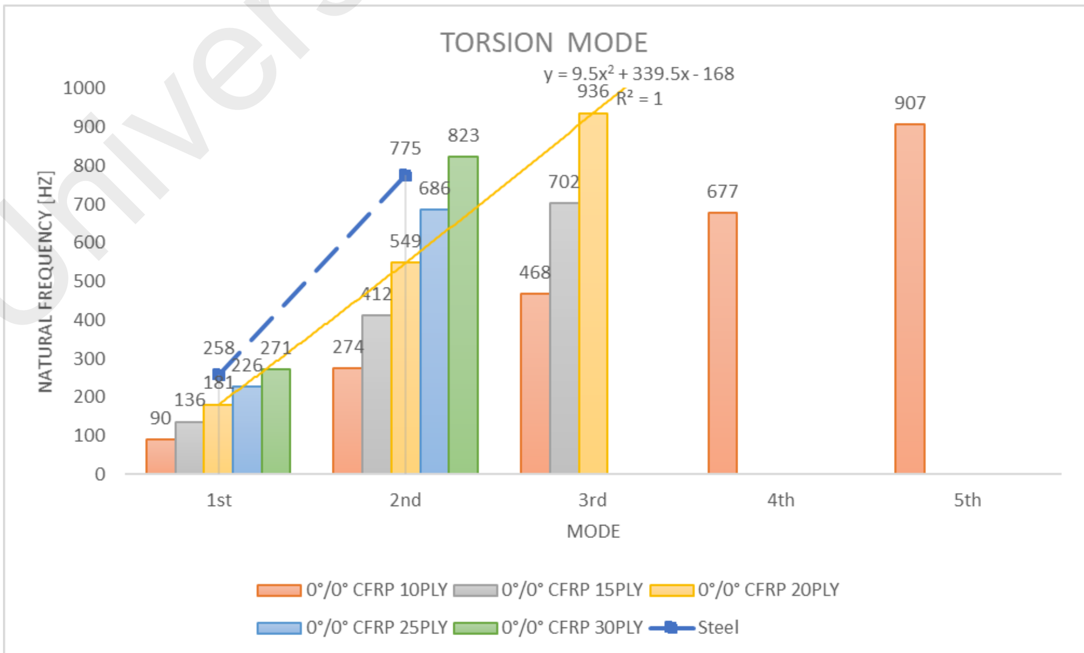

Figure 6.9: Torsion vibration modes for different ply thickness

In comparison to steel cantilever beam, 0°/0° CFRP cantilever beams performed better in terms of resisting bending modes but weaker against torsion modes. In order to achieve equivalent stiffness, the thickness of the CFRP beam has to be 150% thicker than the steel beam (30 plies of CFRP beam (total of 2.6 mm stack) compared to 2.6 mm steel beam thickness in this experiment). Another approach to achieve equivalent stiffness is by varying the ply orientation to improve resistance against torsion. This will be further discussed in the next topic.

Interesting findings in this simulation is that the ply thickness for the same ply orientation of CFRP beams does not affect lateral modes frequency and mode shape. This had been verified with the 0°/90° and 45°/-45° CFRP cantilever beam at 10, 20, and 30 ply thickness (Figure 6.10). The first and second lateral mode for the 0°/90° CFRP at various thicknesses are 121 Hz and 722 Hz, while for the 45°/-45° CFRP cantilever beam are 72 Hz and 445 Hz, respectively. Details are in Appendix F

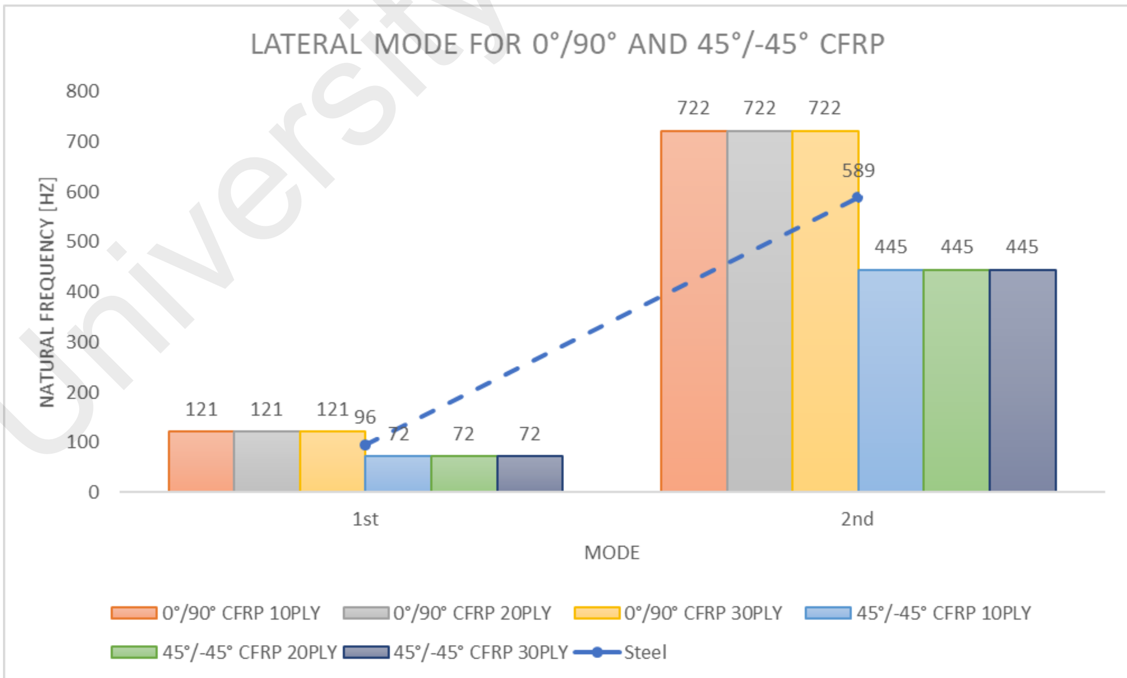

Figure 6.10: Lateral modes for 0°/90° and 45°/-45° at different ply thickness

6.4 Modal analysis of different ply orientation of CFRP cantilever beam

As mentioned in the previous section, ply orientation can be varied to improve the stiffness against torsion and bending. The results of different ply orientation of 20 ply CFRP cantilever beam are shown in Figure 6.11 ~ 6.13. Details of normal mode shape for each frequency is shown in Appendix G.

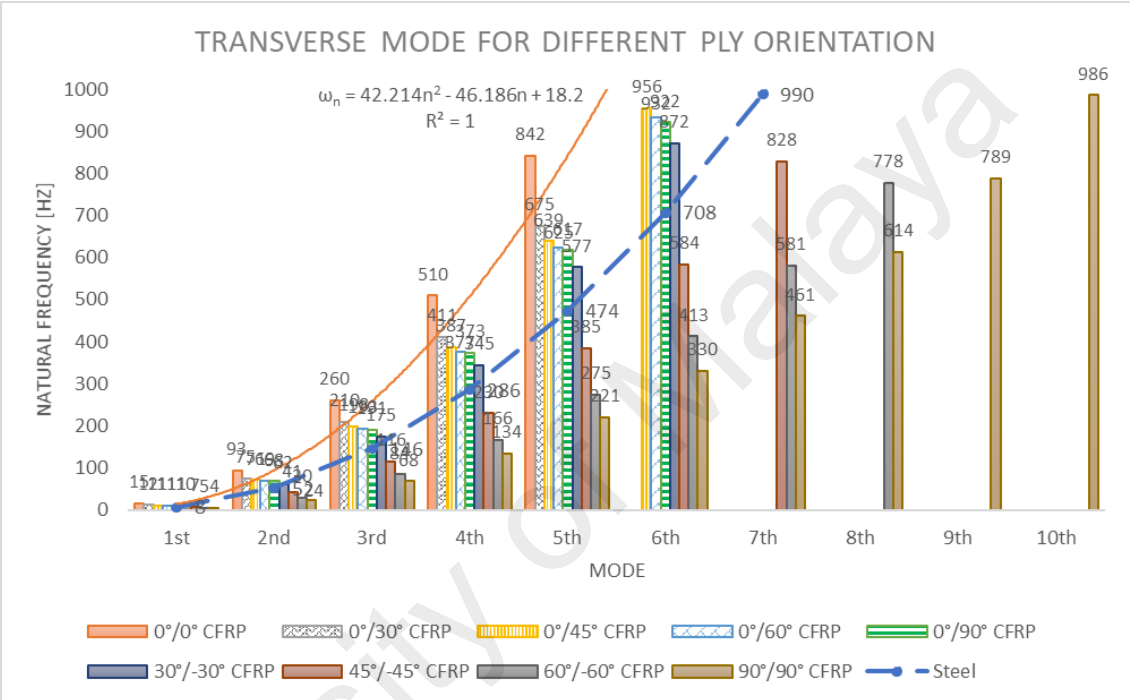

Figure 6.11: Transverse vibration modes for different ply orientation

First, natural frequency and mode shape for 0°/0°, 0°/30°, 0°/45°, 0°/60° and 0°/90° are being observed when the 0° ply is paired with different ply orientation in a stacked laminate. The natural frequency of transverse mode of CFRP beam is becoming lower as the UD fiber angle is away from the longitudinal direction towards the lateral direction (90° ply orientation). Torsional modes also influence the mode shape of each transverse modes as shown in the result in Appendix G. However, the influence of torsion reduces as the ply orientation increases towards lateral direction (90° orientation).

The second part of this simulation is to compare with the result of positive-negative angle alternately arranged for ply orientation. Figure 6.11 shows that all CFRP beam with

0° ply laminate (0°/0°, 0°/30°, 0°/45°, 0°/60°, 0°/90°) and 30°/-30° CFRP beam have better resistance towards bending than steel. Although positive – negative ply orientation does not perform better than steel, this configuration eliminates the influence of torsion in all transverse modes. The result for each ply orientation can also be represented by the quadratic equation where R^2=1.

45°/-45° ply orientation are among the lowest natural frequency against bending as reported in the previous study (Tita et al., 2003). 90°/90° has the worst performance as it has the lowest natural frequency followed by 60°/-60° and 45°/-45° ply orientation. The absence of 0° plies in positive – negative ply orientation pairs reduced their stiffness.

A similar trend of transverse modes can be observed in lateral modes. (Figure 6.12). As the ply angle increases from 0° to 90°, natural frequency for lateral modes decreased. No influence of torsion to the mode shape of lateral modes were found (Appendix G).

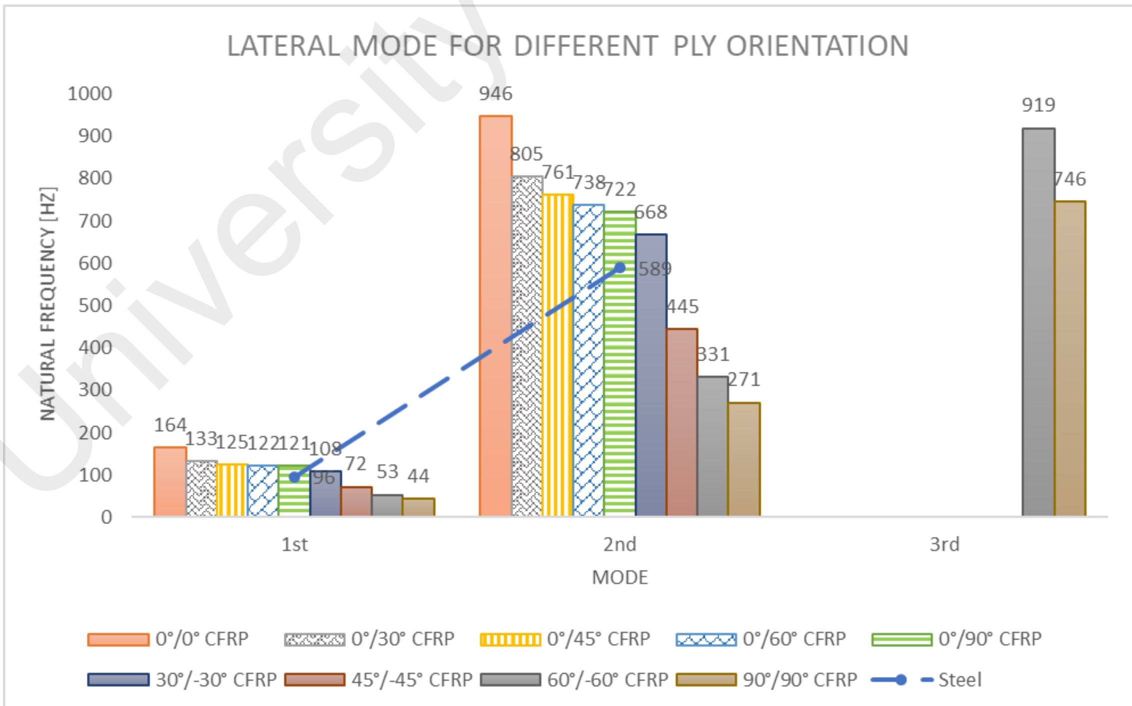

Figure 6.12: Lateral vibration modes for different ply orientation

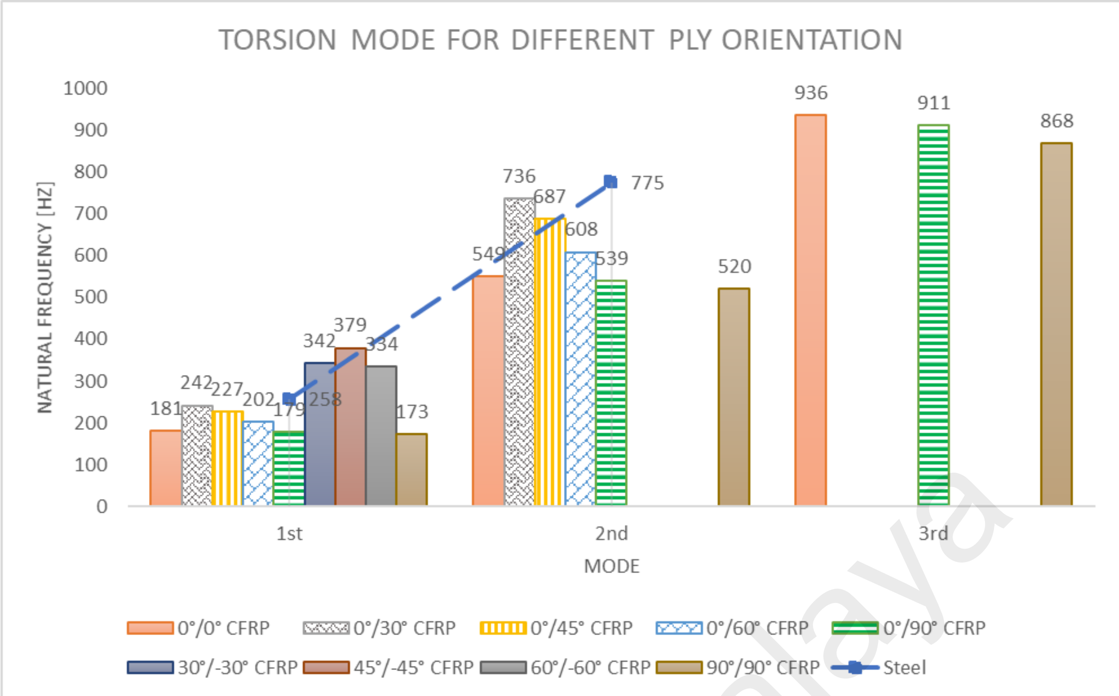

Figure 6.13: Torsion modes for different ply orientation

In term of torsion, 0°/0°, 90°/90° and 0°/90° ply orientation performing worse than steel (Figure 6.13). 30°/-30° CFRP ply configuration can improve the resistance towards torsion as good as 45°/-45° and 60°/-60° plies. They have only one torsion mode below 1 kHz. Here, we know that the alternate positive – negative degree ply angle arrangement could resist the resonance due to torsion. Their mode shapes are also pure torsion mode; they do not have distortion as can be observed in 0°/30°, 0°/45°, and 0°/60° CFRP ply orientations. Negative degree ply angle can cancel out torsions that distorts the mode shape, hence increase the stiffness. As an example, Figure 6.14 shows different of 2nd torsion mode shape between 0° /30° and [0°, (0°/30°)$_6$,0°]$_s$ of 20 plies CFRP.

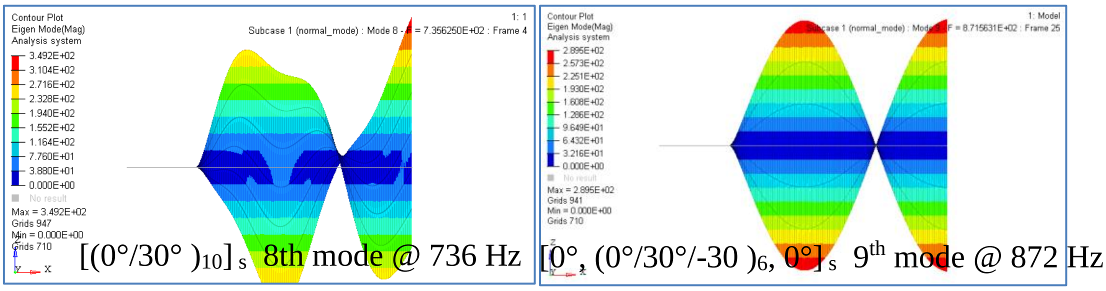

Figure 6.14: 0°/30° and [0°, (0°/30°/-30°)$_6$, 0°]$_s$ of 2nd torsion mode shape

Although the combination of 0° ply with different ply orientation (0°/0°, 0°/30°, 0°/45° and 0°/60°) reduced the stiffness against bending, they do improve the resistance against torsion. In contrast, the natural frequency of 0°/90° plies is always lower than 0°/0° plies, as 90° plies make the performance worse for a cantilever beam. 90°/90° CFRP ply orientation is not performing well in both bending and torsion mode for the cantilever beam. These findings will be confirmed again in the next section for a more complex geometry of strut bar.

There is an enormous difference in weight. Steel cantilever beam weigh 0.41 kg while the 20 ply CFRP beam weighs only 0.093 kg. The simulation results also show that different ply orientations should be stacked together in order to complement each other's advantages and disadvantages.

6.5 Modal analysis of strut bar

There are 36 plies at the mounting on both sides and 10 plies of CFRP at oval-shaped bar connecting both strut to achieve thickness similar to the steel strut (4.7mm at mounting, 1.3mm at the bar). Strut bar is fixed at both ends of strut towers. Mass of the CFRP and steel strut bar is 0.382 and 1.66 kg, respectively. Modal analysis of strut bar result is shown in Figure 6.15 ~ 6.17. In this section, as the geometry becomes more complex, only ply orientations that produced a pure normal mode shape in the previous section are being evaluated; 0°/0°, 30°/-30°, 45°/-45°, 60°/-60°, 90°/90° and 0°/90°.

The natural frequency of all modes is higher than cantilever beam results due to thicker plies at both strut bar mounting that increased the stiffness. On top of that, the natural frequency also increased due to the condition that strut bar is fixed at both ends. Normal mode shape at each frequency is mostly a combination of two bending or torsion modes that are shown in Appendix H. Resonances mostly occurred at the oval-shaped bar given the long length of the beam that was welded only at both ends and relatively thin compared to the mounting side.

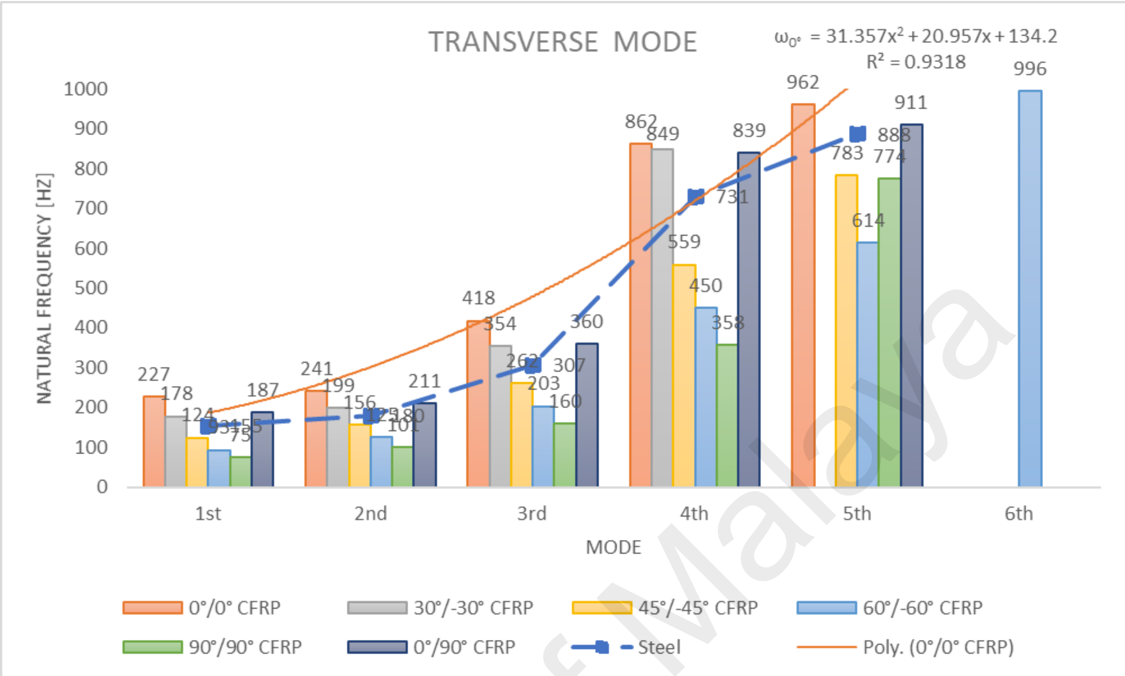

Figure 6.15: Transverse vibration mode of strut bar

Compared to the result in the previous section, 0°/0°, 30°/-30°and 0°/90° CFRP also performed better against bending than steel in strut bar (Figure 6.15). However, due to the more complex geometry, the result of each ply orientation for each mode cannot be perfectly fitted the regression model ($R^2 \neq 1$).

The lateral mode also showed the similar result as in transverse mode (Figure 6.16). Natural frequency for lateral modes decreases and number of modes under 1 kHz increases when the ply angle increases from 0° to 90°.

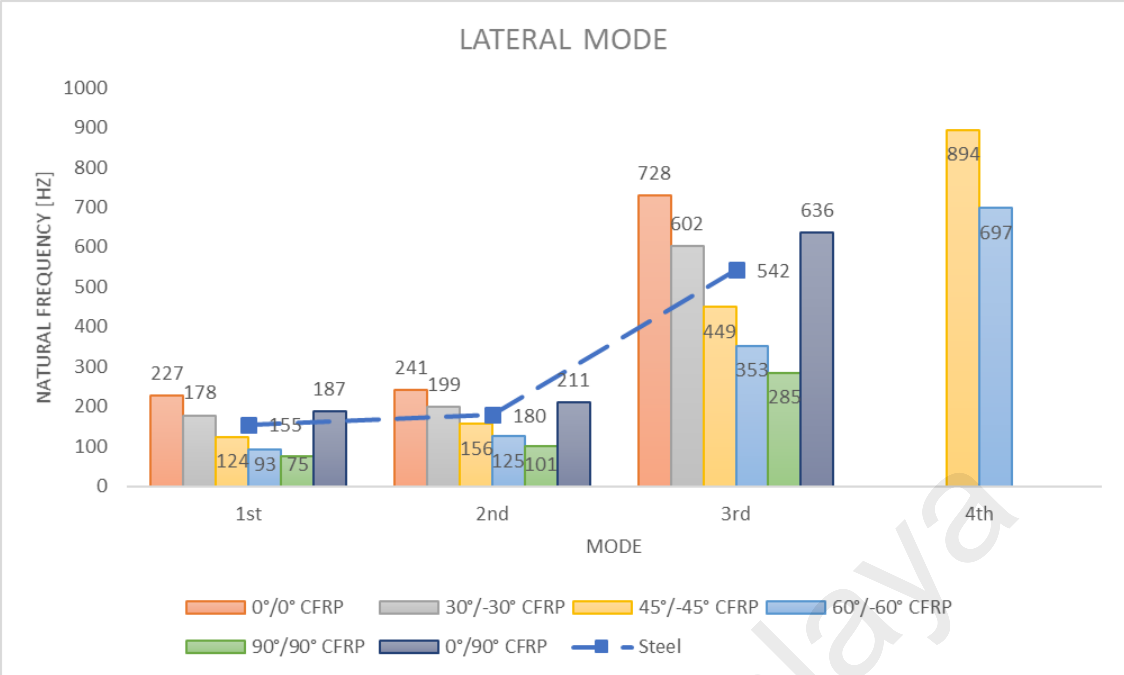

Figure 6.16: Lateral vibration mode of strut bar

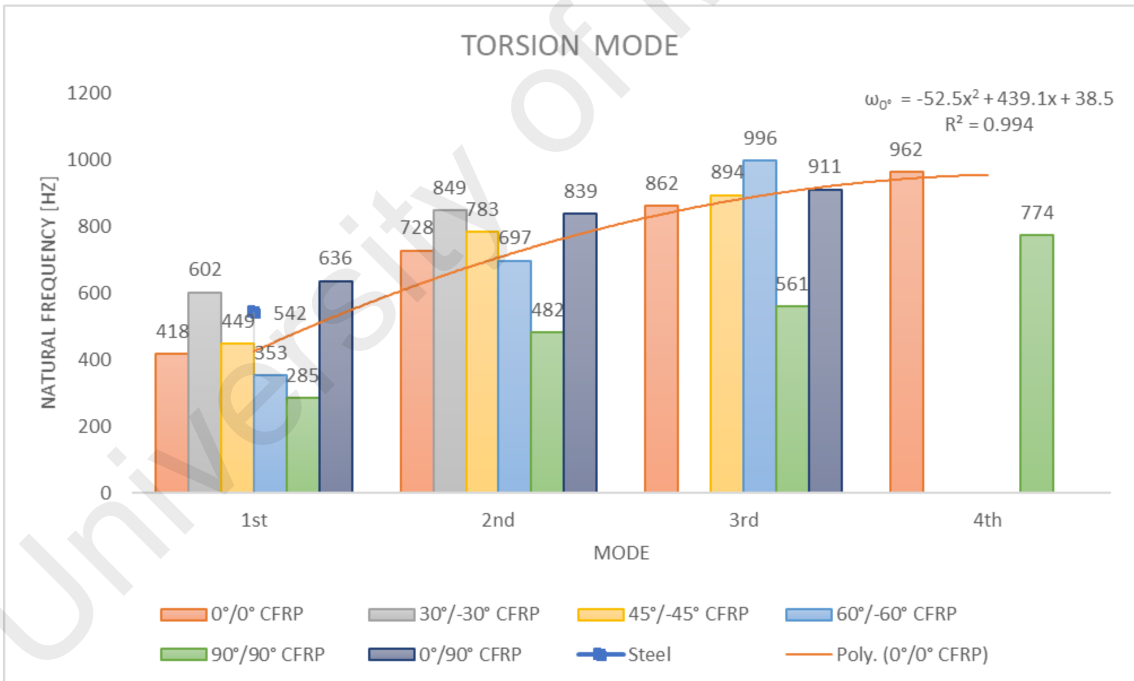

Figure 6.17: Torsion vibration mode of strut bar

0°/0°, 90°/90°, and 0°/90° CFRP strut bar did not perform well against torsion. Similarly, 45°/-45° and 60°/-60° CFRP strut bar against torsion also did not give a good result as when compared to steel strut bar. Torsion vibration modes of 45°/-45° and 60°/-60° ply orientation CFRP strut bar contradicted the findings of CFRP cantilever beam as discussed in the previous section. In a complex strut bar geometry, 30°/-30° ply orientation is preferred in the sense of reducing torsion. 30°/-30° CFRP ply configuration can overcome the weaknesses of 0°/0° ply configuration when these configurations are combined together. The natural frequency of 0°/90° ply orientation is lower than 0°/0° in bending modes due to 90° plies introduced in the stack. Although 90° plies increase the resistance against torsion, but not as good as 30°/-30° ply orientation.

90°/90°, 60°/-60°, and 45°/-45° ply orientation have lower natural frequency and have a higher number of modes under 1 kHz than steel strut bar. Therefore, these ply orientations are not suitable for the strut bar design.

From this simulation, there are many coherences found between simple cantilever beam and strut bar modal analysis. Cantilever beam modal analysis can provide a general overview of the modal analysis of more complex geometry, with a simpler model and less computational effort and did not require reverse engineering for CAD modeling. However, running simulation of an actual geometry can provide more insightful findings such as the 30°/-30° ply is the best ply orientation that reduces torsion for this particular strut bar design, etc.

6.6 Abusive static loading test of strut bar

Static loading test was conducted to find a correlation with the dynamic behavior of strut bar. The results are shown in Figure 6.18. The thickness of CFRP strut bar is exactly same as steel strut bar.

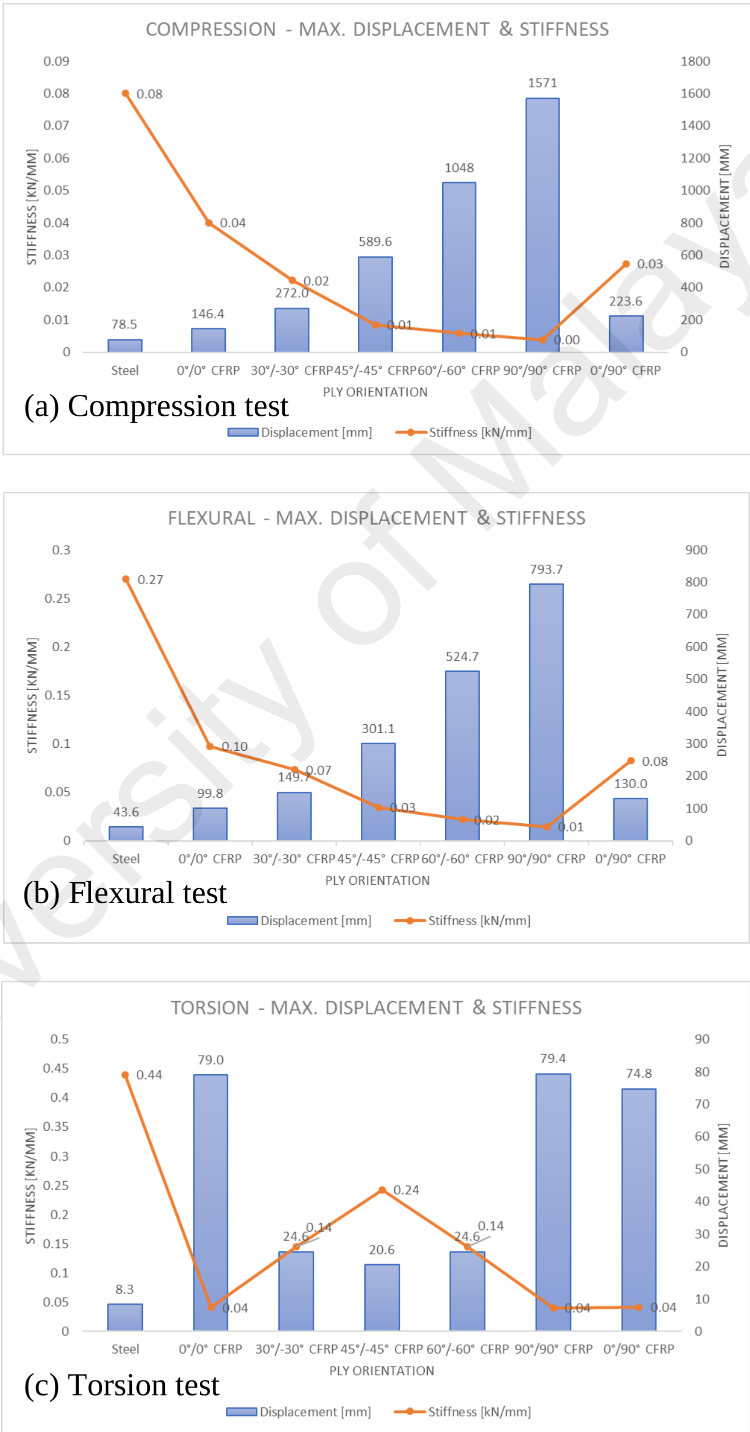

Figure 6.18: Maximum displacement and stiffness of all load cases

As was shown in the modal analysis, 0°/0°, 30°/-30° and 0°/90° gave better resistance towards bending in flexural and compression test. These ply orientations produce a lower displacement and higher stiffness compared to others. However, the stiffness of CFRP is relatively lower than steel for the same geometry. This is most probably due to the lower modulus of elasticity, E as derived in equation 3.36 in section 3.2.2. The elastic modulus of steel is 195 GPa whereas the modulus for CFRP is only up to 130 GPa (longitudinal) and 8.96 GPa (lateral direction), respectively. Same condition for torsion test, as based on equation 3.37, shows that steel strut bar performs better than CFRP strut bar due to its lower shear modulus, G. The shear modulus for steel is 86 GPa while for CFRP is only 7.1 GPa.

The maximum first principal stress of 30°/-30° and 45°/-45° ply orientation CFRP strut bars was close to the steel value. This is the effect of alternate positive – negative ply orientation that allows for more effective distribution of the stress (Figure 6.19). 0°/90° ply orientation becomes second best after 0°/0° in compression and flexural tests, showing that 90° ply would weaken the structure. Least performance of 90°/90° in all tests is an evidence to support this finding.

45°/-45°, 60°/-60°, and 90°/90° ply orientation will be ruled out for composite strut bar optimization process due to inferior performance as compared to steel in both modal analysis and static loading. Although 45°/-45° and 60°/-60° ply orientation show higher stiffness value in torsion, it is not significant when other ply configuration also achieves stiffness value of 0.04 and above.

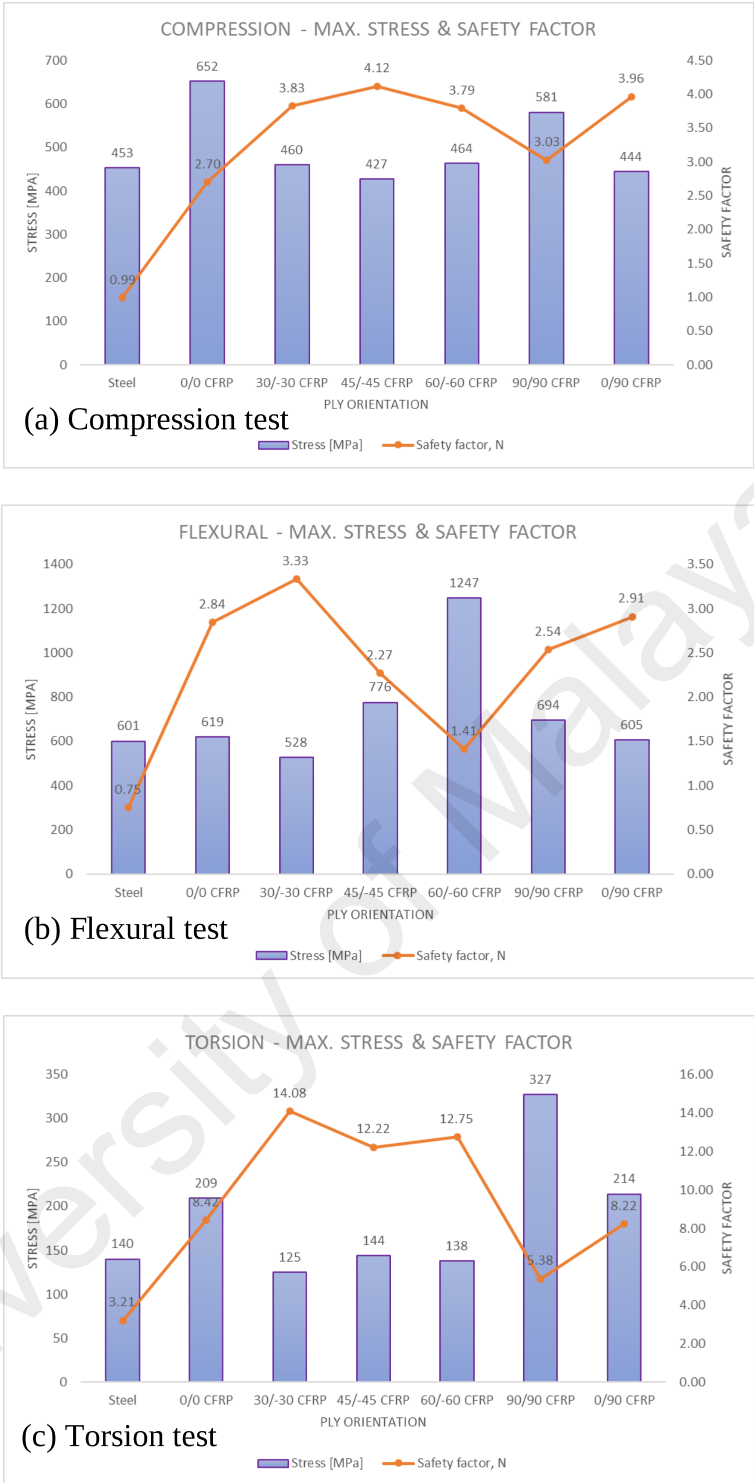

Figure 6.19: Maximum stress and safety factor of all load cases

Based on dynamic behavior and static loading test result from section 6.4 up to this section, a combination of 0°, 30° and -30° ply orientations are deemed to be the best performing candidates for composite strut bar optimization in improving stiffness and minimize the effect of bending and torsion in all directions.

6.7 Design optimization of CFRP strut bar

Below is the pre-optimization result to measure compliance value for each static load case where the thickness of all ply orientation was set to 1 ply (0.1334 mm). The strut bar is consists of three different ply orientations; 0°, 30°, -30°. This process was performed to determine the compliance for each load case. Compliance is the inverse of stiffness and measured in millimeter per Newton [mm/kN].

Table 6.3: Pre-optimization analysis result

Load case	**Compliance, C_i [mm/kN]**	**Weighted compliance, C_w**
Compression	6.022749	1.0
Torsion	2.308172	2.6
Flexural	1.322781	4.5

If weighted compliance for all load cases were set to 1.0, the final design will be heavily influenced by flexural load case due to its compliance is the highest. Torsion load case mostly will not be affecting the final design because it is comparatively low than other load cases. In order to ensure each load case to equally influence the final product design, weighting factor had been applied. Result in weighted compliance column in Table 6.3 was determine by the following equation

$$C_w = \frac{C_{max}}{C_{i,n}} \tag{6.5}$$

C_{max} in this design problem is the compliance value of flexural test and $C_{i,n}$ is the compliance for each load case.

6.7.1 Phase 1: Free size optimization result

Free size optimization produces an optimum shape by removing unnecessary material outside the load path. The thickness of each ply is in super-ply; very thick ply. However, the mass of this initial concept is 1.0 kg, which is lower than steel strut bar mass, 1.66 kg.

The objective of this optimization is to minimize weighted compliance subjected to maximum 1kg weight and static loadings constraints. The improvement of composite strut bar compared to steel is in Table 6.4 below. Figure 6.20 is the visualization of free-size optimized design.

Table 6.4: Free size optimization result

Maximum Displacement	**Steel strut bar [benchmark]**	**Mass constraint [kg]**	**Free-size opt. result**
Compression [mm]	73	1.00	38
Torsion [mm]	8.3	1.00	8.2
Flexural [mm]	40	1.00	21
Mass [kg]	1.66		1.00

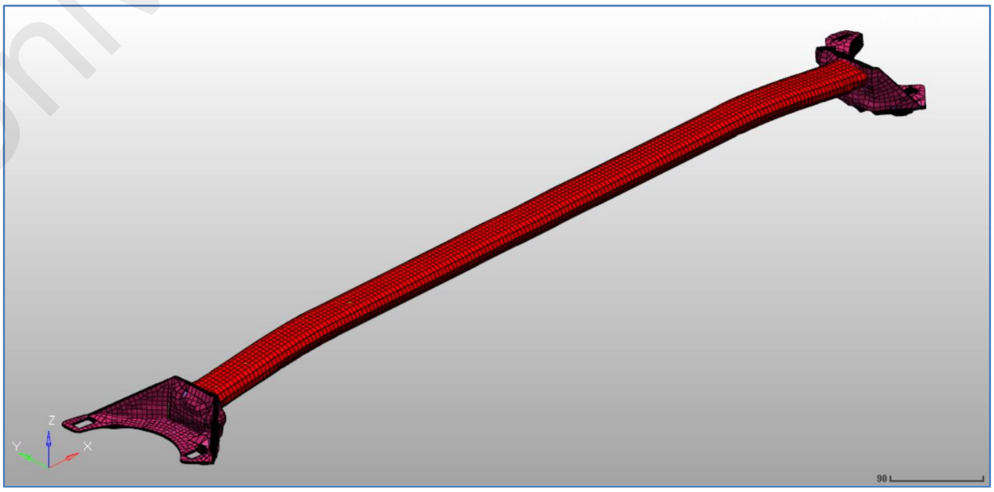

Figure 6.20: Free-size optimization result

6.7.2 Phase 2: Size optimization result

There are two steps involved in this phase; continuous size optimization and discrete size optimization. During this phase, optimum shape and thickness for each ply orientation from free-size are separated (interpreted) into several shapes according to user setup (example in Figure 5.24). In this project, default no. of shape (four shapes) was used. One of the results of free size to continuous size for -30° ply orientation at the mounting is shown in Figure 6.21.

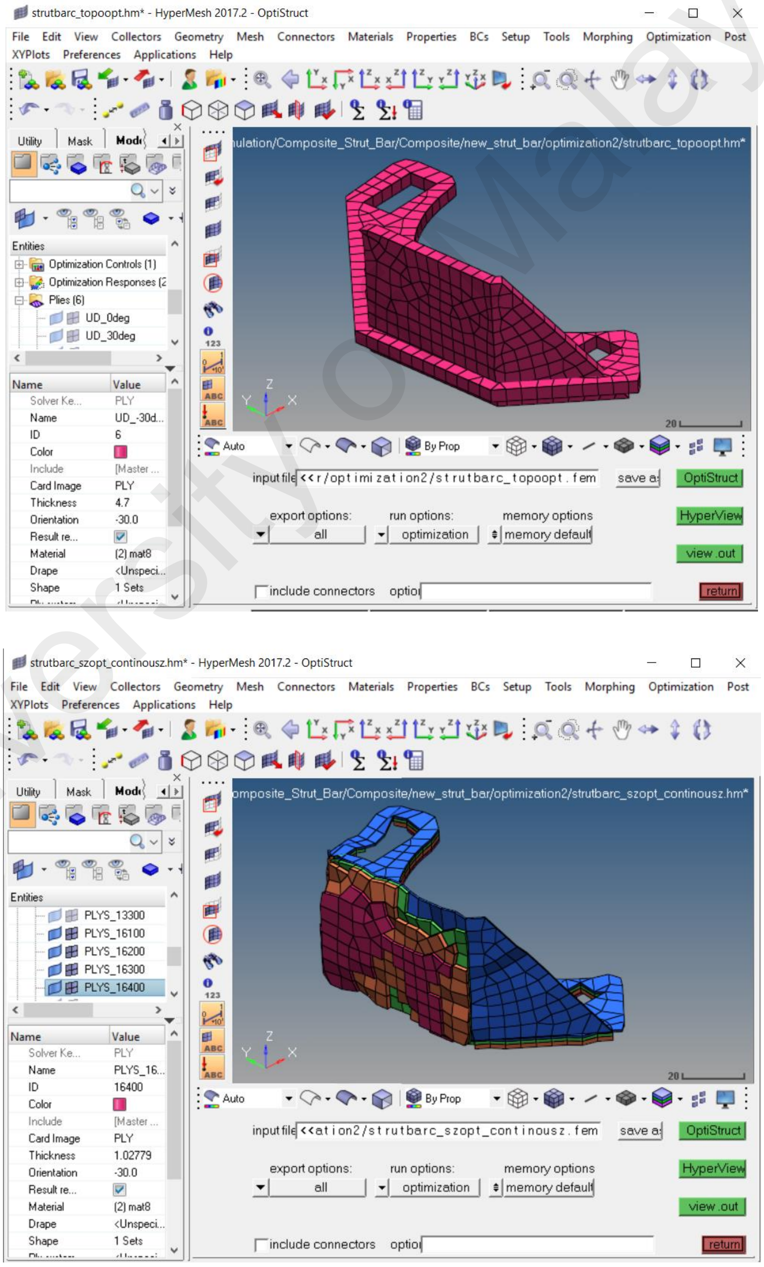

Figure 6.21: Free size (top) to continuous size optimization (bottom)

The thickness of each ply will be reduced to optimum thickness according to design objective. At this size optimization phase, design objective was changed from minimizing weighted compliance in free-size phase to minimizing mass. The constraint was changed from mass (1.0 kg) to static displacement. Here, maximum displacement was allowed up to steel strut bar static displacement value for each load case as shown in Table 6.5.

Table 6.5: Continuous size optimization result

Maximum Displacement	**CFRP strut bar (free-size)**	**Displacement constraint**	**Continuous size opt. result**
Compression [mm]	38	68	58
Torsion [mm]	8.2	9.0	9.0
Flexural [mm]	21	35	32
Mass [kg]	1.00		**0.831**

This results in a lighter weight with better performance than steel strut bar. Mass of CFRP strut bar reduces from 1.0 kg to 0.83 kg.

Next, discrete size optimization can be carried out editing the TMANUF entry in each ply control card. When TMANUF is set, the thick ply bundle can be "sliced" into manufacturable ply thickness, which is 0.1334 mm for each ply. Figure 6.22 shows the result of discrete size optimization process to the ply laminate where all ply bundle has now become individual ply.

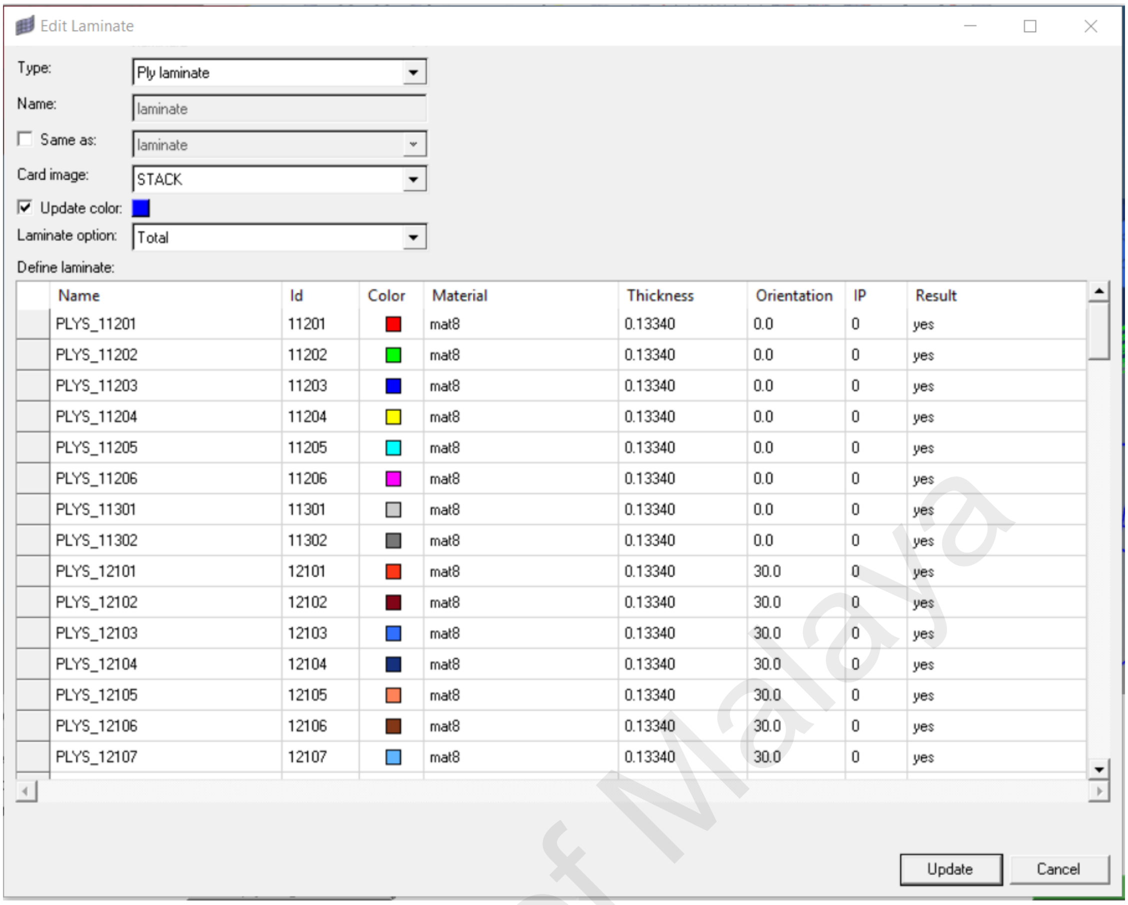

Figure 6.22: Discrete size optimization output

At this point, FSTOSZ control card in was changed to SZTOSH for size to shuffle optimization process. CFRP strut bar mass increases from 0.831 kg to 0.834 kg (Table 6.6).

Table 6.6: Discrete size optimization result

Maximum Displacement	**CFRP strut bar (continuous size)**	**Displacement constraint**	**Discrete size opt. result**
Compression [mm]	58	68	61
Torsion [mm]	9.0	9.0	8.6
Flexural [mm]	32	35	33
Mass [kg]	0.831		**0.834**

6.7.3 Phase 3: Shuffle optimization setup

Shuffle optimization algorithm proposes the optimal stacking sequence could be while preserving the design performance. As current algorithm only supports 45°/-45° ply orientation as a pair and not for 30°/-30° ply, a stacking sequence with a single ply of 30° and -30° to each other is not possible at this moment.

The only manufacturing constraint can be applied to the stack is the maximum successive number of plies of the same orientation does not more than 4 plies in sequence. As shown in DSHUFFLE control card (Figure 6.23), with MSUCC= 4 for the orientations 0°, 30° and -30°. It is defined that maximum four of these plies are allowed to follow each other.

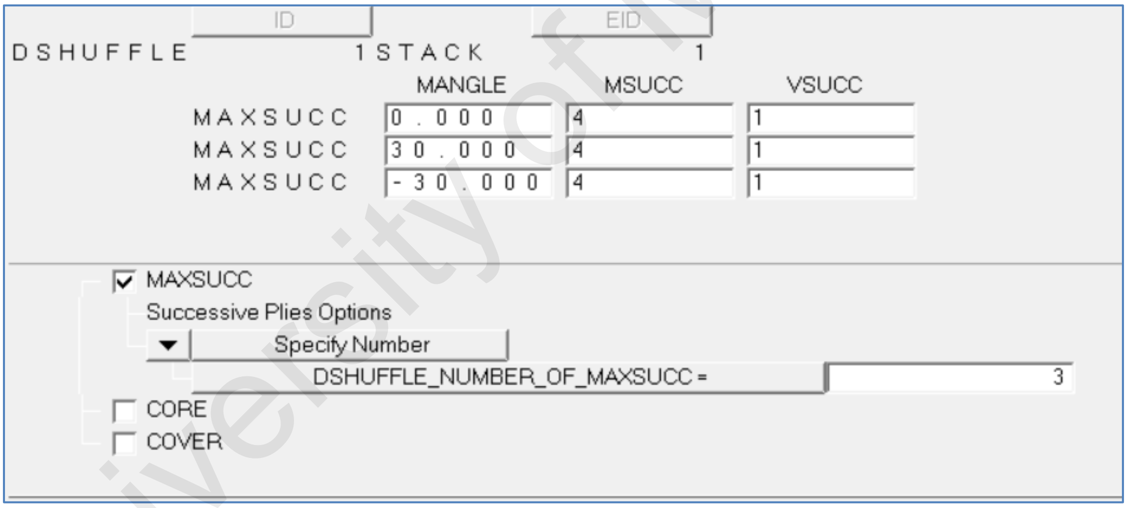

Figure 6.23: Manufacturing constraint setup in DSHUFFLE control card

Table 6.7 shows the optimization results of the final phase in the composite optimization process. There are some changes in displacement and weight increases from 0.834 kg to 0.861 kg. There are plies added in between four successive plies that contributing to the increment in weight.

Table 6.7: Shuffle optimization result

Max. Displacement [mm]	Steel strut bar	CFRP strut bar (discrete size)	Displacement constraint	Shuffling opt. result
Compression	73	61	56	60
Torsion	8.3	8.6	8.0	8.9
Flexural	40	33	32	35
Mass [kg]	1.66	0.834		**0.861**

The outcome of composite optimization of automotive strut bar is shown in Figure 6.24. Surface connecting the mounting and strut bar became slightly thicker to reduce stress concentration in the area. Maximum stress found at bolt area, with significantly lower stress than steel (Appendix J).

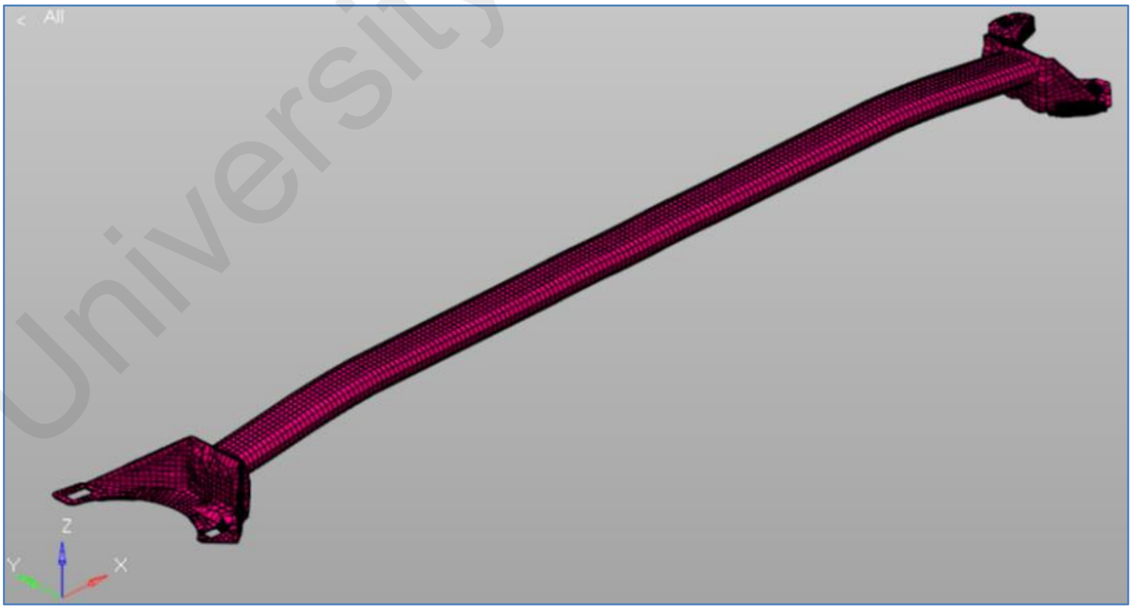

Figure 6.24: Shuffle optimization design.

The result of composite optimization through all phases are shown in Figure 6.25. There are 48% reduction in mass, 18% improvement on compression, 13% improvement on flexural with 7% increase in torsion. However, a slight increase in torsion is acceptable since the maximum displacement due to torsion only increases by 0.6mm.

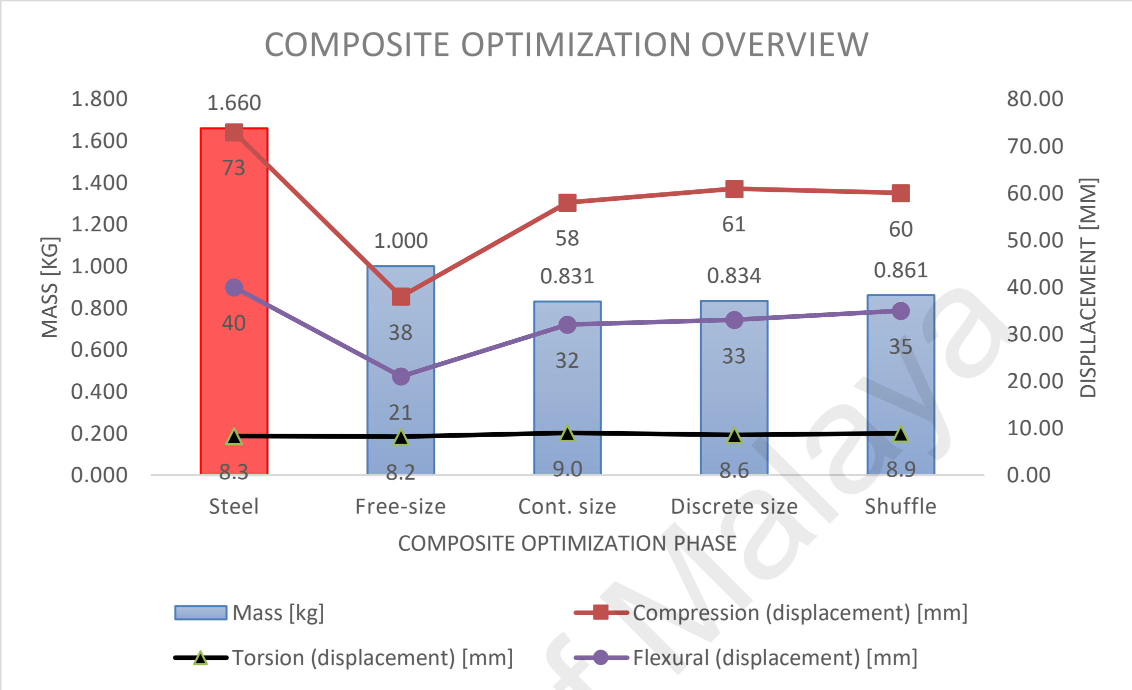

Figure 6.25: Composite optimization result summary

Modal analysis of the final product as compared to steel strut bar is shown in Figure 6.26. The optimized CFRP strut bar only has 4 modes under 1kHz. First and second modes are bending towards Z and Y-direction at 217Hz and 239Hz respectively. Pure bending Z-direction mode occurred in the third mode at 412Hz. The fourth mode is a combination of torsion and bending at 698 Hz. The result shows that natural frequency increased 29% to 40% for each mode (Figure 6.24). Details are in appendix J.

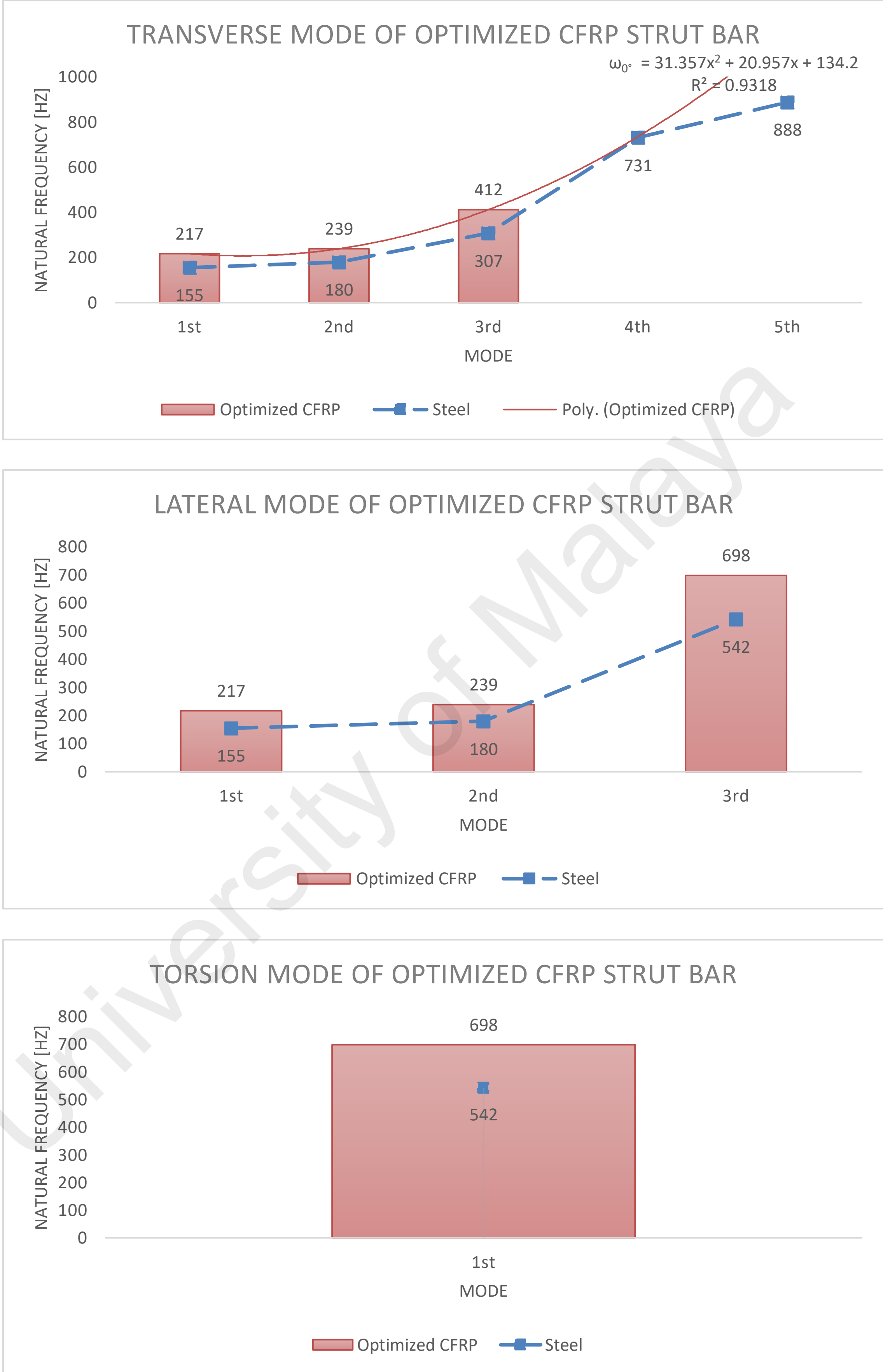

Figure 6.26: Modal analysis of optimized CFRP strut bar

CHAPTER 7: CONCLUSIONS AND RECOMMENDATION

7.1 Conclusions

Dynamic analysis of carbon fiber shown to be a good approach to develop a lightweight yet strong automotive strut bar. The result from simulations can be summarized as follows:

i. Natural frequency for each mode of CFRP cantilever beam increases as the number of ply increases. The result of each ply can be perfectly represented by a quadratic equation where $R^2=1$. However, CFRP beam with the same ply orientation has no change of natural frequency on lateral modes regardless of the ply thickness.

ii. The natural frequency of transverse and lateral mode of 0° ply with different ply orientation (0°/0°, 0°/30°, 0°/45° and 0°/60°) CFRP beam becomes lower as the angle increase, however, the resistance against torsion is improved.

iii. Alternate positive – negative degree ply angle arrangement such as 30°/-30° and 45°/-45° could resist resonance due to torsion. Combination of different ply orientation should be stacked together in order to complement each other's advantages and disadvantages.

iv. 60°/-60° and 90°/-90° CFRP ply orientation is not performing well in both bending and torsion mode for cantilever beam and strut bar.

v. The natural frequency of 0°/90° ply orientation is always lower than 0°/0° in all modes due to 90° plies introduced in the stack of the cantilever beam. But due to complex geometry in strut bar, 90° plies increase the resistance against torsion, but not as good as 30°/-30° ply orientation.

vi. Cantilever beam modal analysis can provide a general overview of the modal analysis of more complex geometry, with a simpler model and less computational effort and did not require reverse engineering for CAD modeling. However, running simulation of an actual geometry can provide more insightful findings.

vii. Based on dynamic behavior and static loading test result, a combination of 0°, 30° and -30° ply orientations are deemed to be the best performing candidates for composite strut bar optimization in improving stiffness while minimizing the effect of bending and torsion in all direction.

viii. Free-size, continuous size, discrete size, and shuffle optimization are the phases involved in composite design optimization. Automotive strut bar mass can be reduced up to 48% while improving or preserving the static and dynamic performance. Natural frequency also increased 29% to 40%. Composite components can also be manufactured according to the manufacturing requirement.

7.2 Recommendation for future works

Dynamic analysis of CFRP cantilever beams and strut bar showed results that were comparable in stiffness with lighter weight. However, several aspects should be investigated further to obtain further lightweight that comply the engineering and manufacturing constraint.

i. Maximum no. of successive plies at same ply orientation should be investigated further to ensure no issue of delamination, fracture, etc.

ii. Manufacturing constraint for balanced no. of ply angle for composite optimization currently limited to 45° /-45° pairs only while this project is using 30° / -30° ply orientation. Modification of balanced no. of ply angle (BALANCE – BYANG) in FE model subroutine can be performed to allow this optimization.

iii. The final design of CFRP strut bar was based on original steel strut bar, caused the thicker ply around the mounting. Fresh design concept to that particular area can distribute the load more efficiently hence possible for further weight reduction.

REFERENCES

Avitabile, P. (2001). Experimental Modal Analysis. *Sound and Vibration*, *35*(1), 1–15.

Berggren, C., & Magnusson, T. (2012). Reducing automotive emissions-The potentials of combustion engine technologies and the power of policy. *Energy Policy*, *41*, 636–643. https://doi.org/10.1016/j.enpol.2011.11.025

Bhudolia, S. K., Perrotey, P., & Joshi, S. C. (2017). Enhanced vibration damping and dynamic mechanical characteristics of composites with novel pseudo-thermoset matrix system. *Composite Structures*, *179*, 502–513. https://doi.org/10.1016/J.COMPSTRUCT.2017.07.093

Cerna, M., & Harvey, A. F. (2000). Application Note 041 The Fundamentals of FFT-Based Signal Analysis and Measurement. Retrieved from http://www.gunthard-kraus.de/DSP/Dsp_CD/DSP_Application_Notes_and_Books_and_Tutorials/The_fundamentals_of_FFT_based_Signal_Analysis_and_measurements/AN041.PDF

Chaphalkar, S. P., Khetre, S. N., & Meshram, A. M. (2015). Modal analysis of cantilever beam Structure Using Finite Element analysis and Experimental Analysis. *American Journal of Engineering Research*, *4*(10), 178–185.

Cheah, L. W., & Heywood, J. B. (2010). Cars on a Diet : The Material and Energy Impacts of Passenger Vehicle Weight Reduction in the U . S . *Engineering*, 121. https://doi.org/http://web.mit.edu/sloan-auto-lab/research/beforeh2/files/LCheah_PhD_thesis_2010.pdf

Church, A. H. (1964). *Mechanical Vibrations*. New York: John Wiley & Sons, Inc.

Deepak, S. V. (2012). Modelling and Analysis of Alloy Wheel, *1*(3).

Deka, B. K., Hazarika, A., Kim, J., Park, Y.-B., & Park, H. W. (2017). Recent development and challenges of multifunctional structural supercapacitors for automotive industries. *International Journal of Energy Research*, *41*(10), 1397–1411. https://doi.org/10.1002/er.3707

Fallah, M. S., Bhat, R., & Xie, W. F. (2008). New nonlinear model of macpherson suspension system for ride control applications. *Proceedings of the American Control Conference*, *3114*(April), 3921–3926. https://doi.org/10.1109/ACC.2008.4587105

Galvez, P., Quesada, A., Martinez, M. A., Abenojar, J., Boada, M. J. L., & Diaz, V. (2017). Study of the behaviour of adhesive joints of steel with CFRP for its application in bus structures. *Composites Part B: Engineering*, *129*, 41–46. https://doi.org/10.1016/J.COMPOSITESB.2017.07.018

Goh, G. D., Dikshit, V., Nagalingam, A. P., Goh, G. L., Agarwala, S., Sing, S. L., … Yeong, W. Y. (2018). Characterization of mechanical properties and fracture mode of additively manufactured carbon fiber and glass fiber reinforced thermoplastics. *Materials & Design*, *137*, 79–89.

https://doi.org/10.1016/J.MATDES.2017.10.021

Gur, Y., & Wagner, D. (2017). Damping properties and NVH Modal Analysis Results of Carbon Fiber Composite Vehicle Components. *SAE Int. J. Mater. Manf.*, *10*(2), 198–205. https://doi.org/10.4271/2017-01-0500

Irina, M. M. W., Azmi, A. I., Tan, C. L., Lee, C. C., & Khalil, A. N. M. (2015). Evaluation of Mechanical Properties of Hybrid Fiber Reinforced Polymer Composites and their Architecture. *Procedia Manufacturing*, *2*, 236–240. https://doi.org/10.1016/j.promfg.2015.07.041

Irvine, T. (2000). An Introduction To Frequency Response Functions, 1–14. Retrieved from http://www.staff.vu.edu.au/msek/FRF.pdf

Jagannatha, T. D., & Harish, G. (2015). MECHANICAL PROPERTIES OF CARBON/GLASS FIBER REINFORCED EPOXY HYBRID POLYMER COMPOSITES. *Int. J. Mech. Eng. & Rob. Res*. Retrieved from http://www.ijmerr.com/uploadfile/2015/0421/20150421101601643.pdf

Kalantari, M., Dong, C., & Davies, I. J. (2017). Effect of matrix voids, fibre misalignment and thickness variation on multi-objective robust optimization of carbon/glass fibre-reinforced hybrid composites under flexural loading. *Composites Part B: Engineering*, *123*, 136–147. https://doi.org/10.1016/J.COMPOSITESB.2017.05.022

Kangde, S., Shitole, V., & Sahu, A. K. (2014). Suspension Strain Correlation Using Flex Bodies in MBD. SAE International . https://doi.org/10.4271/2014-01-0763

Kuş, A. (2009). Implementation of 3D Optical Scanning Technology for Automotive Applications. *Sensors*, *9*, 1967–1979. https://doi.org/10.3390/s90301967

Lee, H. C., Oh, H. J., & Kim, S. S. (2013). The Design of a Hybrid Composite Strut Tower for Improving Impact Resistance and Light-weight, *26*(4), 223–229.

Lutsey, N. (2010). Review of technical literature and trends related to automobile mass-reduction technology. *California Air Resources Board*, (May).

Maia, N. M. M., & Silva, J. M. M. (2001). Modal Analysis Identification Techniques. *Philosophical Transactions: Mathematical, Physical and Engineering Sciences*, *359*(1778), 29–40. Retrieved from http://www.jstor.org/stable/3066392

Matthews, F. L. (2003). *Finite element modelling of composite materials and*.

Miller, W. ., Zhuang, L., Bottema, J., Wittebrood, a. ., De Smet, P., Haszler, a, & Vieregge, a. (2000). Recent development in aluminium alloys for the automotive industry. *Materials Science and Engineering: A*, *280*(1), 37–49. https://doi.org/10.1016/S0921-5093(99)00653-X

Moaveni, S., & Saeed. (2008). *Finite element analysis : theory and application with ANSYS*. Pearson Prentice Hall. Retrieved from https://dl.acm.org/citation.cfm?id=1203619

Mohamed, N. M., EL-Wazery, M. S., EL-Elamy, M. I., & Zoalfakar A, S. H. (2017). Mechanical and Dynamic Properties of Hybrid Composite laminates. *International Journal of Advanced Engineering and Global Technology*, *5*(3). Retrieved from http://ijaegt.com/wp-content/uploads/2017/04/609971-pp-1703-1725-MD-Updated.pdf

Mohammed, O. A. (2013). Mohammed: Vibration analysis of hybrid laminated composite beam Vibration analysis of hybrid laminated composite beam. *Al-Rafid. Engin.*, *21*(4), 210–216. Retrieved from https://www.iasj.net/iasj?func=fulltext&aId=77211

Ni, R. G., Lin, D. X., & Adams, R. D. (1984). The dynamic properties of carbon-glass fibre sandwich-laminated composites: theoretical, experimental and economic considerations. *Composites*, *15*(4), 297–304. https://doi.org/10.1016/0010-4361(84)90710-9

Qviller, A. (2012). *Development of car for Eco-marathon*. Norwegian University of Science and Technology. Retrieved from https://brage.bibsys.no/xmlui/handle/11250/241597

Saravanan. S, K. (2007). Experimental Analysis of Carbon/Glass Fiber Reinforced Epoxy Hybrid Composites with Different Carbon/Glass Fiber Ratios. *International Journal of Innovative Research in Science, Engineering and Technology (An ISO Certified Organization)*, *3297*(5). https://doi.org/10.15680/IJIRSET.2016.0505023

Schwarz, B. J., & Richardson, M. H. (1999). Experimental Modal Analysis. *CSI Reliability Week*, *35*(1), 1–12. https://doi.org/10.1016/j.jbiomech.2011.03.005

Takamatsu, M., Fujita, H., Inoue, H., & Kijima, M. (1992). Development of Lighter-Weight, Higher-Stiffness Body for New RX-7. SAE International . https://doi.org/10.4271/920244

Tita, V., Carvalho, J. de, & Lirani, J. (2003). Theoretical and experimental dynamic analysis of fiber reinforced composite beams. *Journal of the Brazilian Society of Mechanical Sciences and Engineering*, *25*(3), 306–310. https://doi.org/10.1590/S1678-58782003000300014

Wang, J., Shi, C., Yang, N., Sun, H., Liu, Y., & Song, B. (2018). Strength, stiffness, and panel peeling strength of carbon fiber-reinforced composite sandwich structures with aluminum honeycomb cores for vehicle body. *Composite Structures*, *184*, 1189–1196. https://doi.org/10.1016/j.compstruct.2017.10.038

Warren Dias. (2011). Optimization of Laminate Composite Structures – Recent Advances and Applications - Altair HyperWorks Insider. Retrieved October 6, 2017, from http://insider.altairhyperworks.com/opt-laminate-composite/

William F. Milliken, & Douglas L. Milliken. (1994). *Race Car Vehicle Dynamics*. SAE International. Retrieved from http://books.sae.org/r-146/